UNIVERSITY
OF TRENTO - Italy

Faculty of Science - Department of Physics
Doctoral School in Physics

XXIV cycle

Optimization of nanostructured materials towards gas sensing

Matteo Tonezzer

Tutors:

Prof. Antonio Miotello

Dr. Salvatore Iannotta

Scientific Committee:

Prof. Roberto S. Brusa

Prof. George. G. Malliaras

Prof. Giovanni Mattei

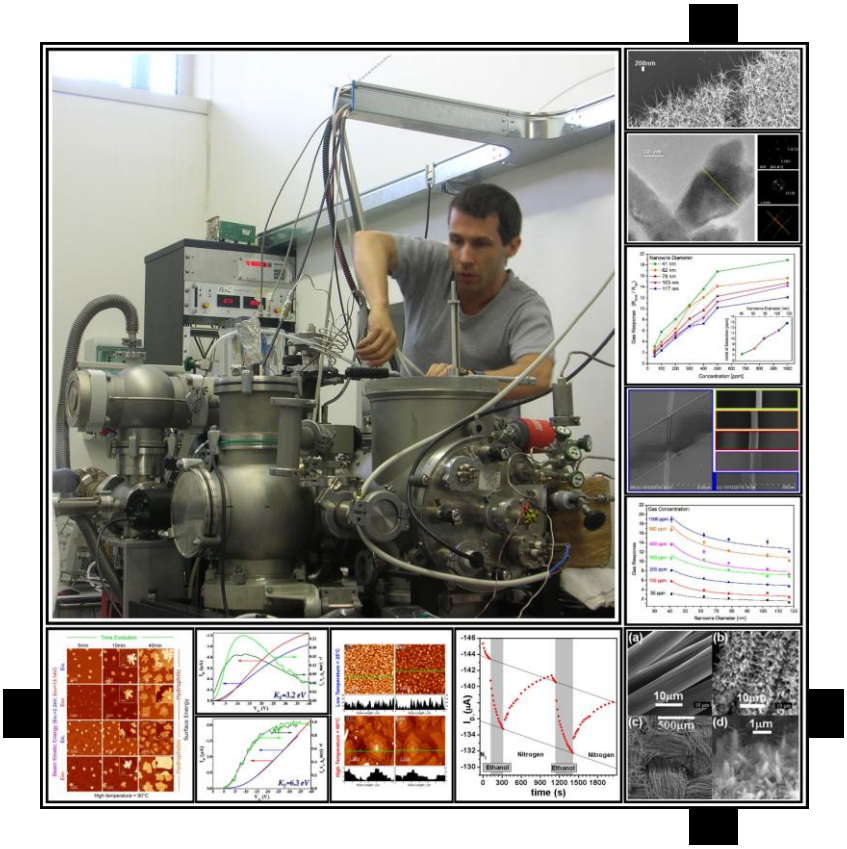

Summary

Acknowledgments

First of all I would like to sincerely thank the people who maybe didn't even notice how much they supported my decision to face this adventure: Prof. Massimo Sancrotti *in primis*, then Prof. Enzo di Fabrizio, Dr. Salvatore Iannotta and Prof. Alberto Morgante. Their spur has been crucial.

Together with them I would like to thank Prof. Antonio Miotello for accompanying and supporting me along this profitable journey during which I learnt so much. I'm also grateful to Dr. Tullio Toccoli, who introduced me to the wonderful world of organic materials, and to Prof. Rodrigo G. Lacerda, who made me discover the fascinating universe of metal oxide nanowires.

A personal thank goes also to Prof. Masakazu Nakamura and Dr. Ryosuke Matsubara, who warmly welcomed me in Chiba, for their collaboration and even more for their friendship.

I'm grateful to all the people who helped with this work and whom I try to remember all here: Cristina Armellini, Paolo Bettotti, Claudio Corradi, Stefano Gottardi, Tran Quang Huy, Marco Pola, Eveline Rigo, Nguyen Van Toan and Laura Toniutti.

I want then to thank my family, for the support they gave me before and along this journey; my parents have been one of the few "companies" in Italy which invested generously in scientific research. A general thank flies also to all of my friends, starting from Lino and Laura, who always nodded smiling when I, carried away by enthusiasm, was talking too scientifically.

Matteo

Congress and conference attendances

2011

1. M. Tonezzer and N.V. Hieu

   "Size-dependent response of single-nanowire gas sensors confirms depletion layer model",
   accepted at "EMCMRE 2011, Euro-Mediterranean Conference on Materials and Renewable Energies",

   21 -25 November 2011, Marrakech, Morocco.

2. M. Tonezzer, T. Toccoli, S. Gottardi, P. Bettotti, E. Rigo and S. Iannotta

   "Growth and performance of quasi-monocrystalline α-Sexithiophene deposited by Supersonic Molecular Beam Deposition: because energy matters",
   accepted at "EMCMRE 2011, Euro-Mediterranean Conference on Materials and Renewable Energies",

   21 -25 November 2011, Marrakech, Morocco.

3. S. Gottardi, T. Toccoli, M. Tonezzer, P. Bettotti, S. Iannotta and P. Rudolf

   "Controlling molecules' momentum with SuMBD: the early stages of Pentacene growth on SiOx/Si",
   oral at "ICOE 2011, International Conference on Organic Electronics",

   22 -24 June 2011, Rome, Italy.

4. T. Toccoli, E. Borga, D. Maniglio, C. Fasoli, S. Gottardi, M. Tonezzer and S. Iannotta

   "Organic Electrochemical Transistors based on PEDOT:PSS: biocompatible devices to sense the cells metabolism and drug activity",
   poster at "ICOE 2011, International Conference on Organic Electronics",

   22 -24 June 2011, Rome, Italy.

5. S. Gottardi, T. Toccoli, M. Tonezzer, P. Bettotti, P. Rudolf and S. Iannotta

   "Controlling molecules' momentum with SuMBD: the early stages of Pentacene growth on SiOx/Si",
   oral at "XX AIV Conference 2011 – Italian Association of Science and Technology",

   17 -19 May 2011, Padua, Italy.

6. T. Toccoli, D. Maniglio, C. Fasoli, M. Zanetti, M. DallaSerra, S. Gottardi, M. Tonezzer and S. Iannotta

   "Organic Electrochemical Transistors based on PEDOT:PSS: biocompatible devices to sense the pore formation in bilayer lipid membranes attacked by bacterial pore forming toxins",
   oral at "XX AIV Conference 2011 – Italian Association of Science and Technology",

   17 -19 May 2011, Padua, Italy.

7. M. Tonezzer, T. Toccoli, S. Gottardi, E. Rigo, P. Bettotti and S. Iannotta
"Growth and performance of polycrystalline α-Sexi-thiophene thin films deposited by Supersonic Molecular Beam Deposition",
poster at "EMRS Spring Meeting 2011 – European Materials Research Society",
9 -13 May 2011, Nice, France.

8. S. Gottardi, Y. Wu, T. Toccoli, M. Tonezzer, S. Iannotta and P. Rudolf
"The role of perpendicular and parallel momentum in early stages of pentacene growth with SuMBD",
oral at "EMRS Spring Meeting 2011 – European Materials Research Society",
9 -13 May 2011, Nice, France.

9. M. Tonezzer, R. G. Lacerda
"Characterization of sensing properties of C/ZnO hybrid nanostructures",
poster at "EMRS Spring Meeting 2011 – European Materials Research Society",
9 -13 May 2011, Nice, France.

10. M. Tonezzer, N. V. Hieu
"Gas sensing properties of SnO_2 single nanowire transistors",
poster at "EMRS Spring Meeting 2011 – European Materials Research Society",
9 -13 May 2011, Nice, France.

2010

11. C. Fasoli, M. Tonezzer, T. Toccoli, S. Gottardi, C. Corradi, M. Pola, P. Bettotti, E. Rigo, L. Pavesi and S. Iannotta
"High performance oligothiophenes devices grown by SuMBD",
oral at "ICG 2010 – Italian Crystal Growth 2010,
18 -19 November 2010, Parma, Italy.

12. S. Gottardi, Y. Wu, T. Toccoli, M. Tonezzer, S. Iannotta, P. Rudolf
"The effects of perpendicular and parallel momentum in pentacene growth with SuMBD",
oral at "ICG 2010 – Italian Crystal Growth 2010,
18 -19 November 2010, Parma, Italy.

13. M. Tonezzer, T. Toccoli, E. Rigo, P. Bettotti, L. Pavesi and S. Iannotta
"Growth and performance of polycrystalline organic thin films deposited by Supersonic Molecular Beam Deposition",
oral at "IWAMSN 2010 – International Workshop on Advanced Material Science and Nanotechnology",
9 -12 November 2010, Hanoi, Vietnam.

14. M. Tonezzer, R.G. Lacerda

"Characterization of sensing properties of a C/ZnO hierarchical nanostructure",

poster at "IWAMSN 2010 – International Workshop on Advanced Material Science and Nanotechnology",

9 -12 November 2010, Hanoi, Vietnam.

15. S. Gottardi, W. Yu, T. Toccoli, M. Tonezzer, S. Iannotta and P. Rudolf

"The role of perpendicular and parallel momentum in early stages of pentacene growth with SuMBD",

oral at "ECOSS 27 – European Conference on Surface Science",

29 August - 3 September 2010, Groningen, The Netherlands.

16. M. Tonezzer, T. Toccoli, T. Nomura, R. Matsubara, S. Gottardi, M. Nakamura and S. Iannotta

"Grains and domain boundaries control of organic semiconductors grown by supersonic molecular beams",

oral at "ECOSS 27 – European Conference on Surface Science",

29 August - 3 September 2010, Groningen, The Netherlands.

17. T. Toccoli, M. Tonezzer, S. Gottardi, C. Fasoli, W. Yu, P. Rudolf and S. Iannotta

"Supersonic Molecular Beams of Pentacene: The influence of kinetic energy on the growth processes",

oral at "27th International Symposium on Rarefied Gas Dynamic",

10 - 15 July 2010, Pacific Grove, California, USA.

18. M. Tonezzer, T. Toccoli, S. Gottardi, E. Rigo, P. Bettotti, L. Pavesi and S. Iannotta

"SuMBD growth of α-sexithiophene thin films: influence of kinetic energy on sub-monolayer formation and device performance",

oral at "27th International Symposium on Rarefied Gas Dynamic",

10 - 15 July 2010, Pacific Grove, California, USA.

19. R.V. Maltsev, A.K. Rebrov, T. Toccoli, M. Tonezzer, N. Coppedè and S. Iannotta

"The Influence of Nozzle Geometry on the Properties of Molecular Beam with Heavy Organic Molecules",

oral at "27th International Symposium on Rarefied Gas Dynamic",

10 - 15 July 2010, Pacific Grove, California, USA.

20. L. Quazuguel, C. Fasoli, S. Iannotta, M. Tonezzer and T. Toccoli

"Morphology and devices properties of picene films grown by Supersonic Molecular Beams",

poster at "NN10 - 7th International Conference on Nanoscience & Nanotechnologies",

11-14 July 2010, Halkidiki, Greece.

21. M. Tonezzer, R.G. Lacerda

"ZnO nanowires on C microfiber architecture as flexible gas sensor",

poster at "NN10 - 7th International Conference on Nanoscience & Nanotechnologies",

11-14 July 2010, Halkidiki, Greece.

22. M. Tonezzer, T. Toccoli, S. Gottardi, P. Bettotti, E. Rigo, L. Pavesi and S. Iannotta

"Growth and performance of polycrystalline α-Sexi-thiophene thin films deposited by Supersonic Molecular Beam Deposition",
oral at "IS-FOE10 - 3rd International Symposium on Flexible Organic Electronics",

6-9 July 2010, Eagles Palace Hotel, Ouranoupolis, Greece.

23. M. Tonezzer, T. Toccoli, S. Gottardi, W. Yu, P. Rudolf and S. Iannotta

"The role of perpendicular and parallel momentum in early stages of pentacene growth with SuMBD",
oral at "IS-FOE10 - 3rd International Symposium on Flexible Organic Electronics",

6-9 July 2010, Eagles Palace Hotel, Ouranoupolis, Greece.

24. M. Tonezzer, T. Toccoli, C. Fasoli, S. Gottardi, P. Bettotti, E. Rigo, L. Pavesi and S. Iannotta

"High performance Oligothiophenes devices grown by SuMBD",
poster at "ICOE 2010, International Conference on Organic Electronics",

22 - 25 June 2010, Paris, France.

25. C. Fasoli, D. Maniglio, T. Toccoli, M. Tonezzer, A. Motta and S. Iannotta

"PEDOT::PSS EOCT realized by ink jet technique for the ionic control in dynamic flux of water solution",
poster at "ICOE 2010, International Conference on Organic Electronics",

22 - 25 June 2010, Paris, France.

26. T. Toccoli, M. Tonezzer, S. Gottardi, C. Fasoli, P. Bettotti, E. Rigo, L. Pavesi and S. Iannotta

"High Ordered Thin Film of Oligothiophenes Grown by SuMBD: Optical, Electrical and Morphological Characterization",
oral at "CIMTEC 2010, 5th Forum on New Materials",

13 - 18 June 2010, Montecatini Terme, Italy.

27. M. Tonezzer, E. Rigo, T. Toccoli, S. Gottardi, P. Bettotti, L. Pavesi and S. Iannotta

"SuMBD growth of α-sexithiophene thin films: influence of kinetic energy on sub-monolayer formation and device performance",
oral at "EMRS 2010",

8 - 10 June 2010, Strasbourg, France.

28. M. Tonezzer and R. G. Lacerda

"Integrated zin oxide nanowires/carbon microfiber gas sensor with improved performance",
poster at "EMRS 2010", 8 - 10 June 2010, Strasbourg, France.

2009

29. M. Tonezzer, E. Rigo, T. Toccoli, S. Gottardi, P. Bettotti, L. Pavesi and S. Iannotta

    "SuMBD growth of oligothiophenes thin films: influence of kinetic energy on sub-monolayer formation and device performance",
    oral at "SLONANO 2009",

    19 - 21 October 2009, Ljubljana, Slovenia.

30. M. Tonezzer and R.G. Lacerda

    "Easy and cheap ZnO/C nano-on-micro architecture for gas sensing applications",
    poster at "SLONANO 2009",

    19 - 21 October 2009, Ljubljana, Slovenia.

31. T. Toccoli, S. Gottardi, M. Tonezzer, P. Bettotti, L. Pavesi, S. Destri, M.C. Pasini and S. Iannotta

    "Oligothiophenes thin films grown by SuMBD: morphological, structural and electrical characterization",
    oral at "FUTURMAT1 – First International Meetingon Organic Materials for a Better Future",

    Ostuni, 12 – 16 September 2009.

32. M. Tonezzer, T. Toccoli, S. Gottardi, P. Bettotti, L. Pavesi and S. Iannotta

    "Oligothiophenes thin films grown by SuMBD: the influence of kinetic energy on sub-monolayer formation",
    oral at "ECOSS 2009 – European Conference On Surface Science",

    Parma, 30 August – 4 September 2009.

33. T. Toccoli, Y. Wu, J. Zhang, N. Koch, M. Tonezzer, S. Iannotta and P. Rudolf

    "High quality pentacene sub-monolayer by supersonic molecular beam epitaxy",
    oral at "ECOSS 2009 – European Conference On Surface Science", Parma, 30 August – 4 September 2009.

List of publications

1. M. Tonezzer*, T. Toccoli, E. Rigo, P. Bettotti and S. Iannotta
   "α-Sexithiophene growth by SuMBD: Enhanced Growth Control and Devices Performances"
   submitted to ***Advanced Functional Materials.***

2. M. Tonezzer*, N.V.Hieu*
   "Size-dependent response of single-nanowire gas sensors"
   accepted to ***Sensors and Actuators B: Chemical.***

3. A.K. Rebrov, P.A. Skovorodko*, T. Toccoli, M. Tonezzer, N. Coppedè, S. Iannotta
   "Experimental and Numerical Study of Pentacene Molecular Beam Seeded in the Free Jet of Helium",
   AIP Conf. Proc., 1333 (2011) 607.

4. R.V. Maltsev, A.K. Rebrov, T. Toccoli, M. Tonezzer, N. Coppedè, S. Iannotta
   "Optimizing Nozzle Geometry for Controlling Properties of Molecular Beam with Heavy Organic Molecules",
   AIP Conf. Proc., 1333 (2011) 413.

5. M. Tonezzer*, E. Rigo, S. Gottardi, P. Bettotti, L. Pavesi, S. Iannotta and T. Toccoli*
   "The role of kinetic energy of impinging molecules in □-sexithiophene growth",
   Thin Solid Films, 519 (2011) 4110.

6. M. Tonezzer* and R.G. Lacerda
   "Zinc oxide nanowires on carbon microfiber as flexible gas sensor",
   in press, published online on ***Physica E: Low-dimensional Systems and Nanostructures***.
   doi:10.1016/j.physe.2010.11.029

7. N. Coppedè, M. Nardi, T. Toccoli, M. Tonezzer, F. Siviero, V. Micheli, A.C. Meyer and S. Iannotta*
   "Solid state dye sensitized solar cells based on supersonic beam deposition of organic, inorganic cluster assembled and nano-hybrid materials",
   Journal of Renewable and Sustainable Energy, 2 (2010) 053106.

8. M. Tonezzer* and R.G. Lacerda
   "Integrated zinc oxide nanowires/carbon microfiber gas sensors",
   Sensors and Actuators B: Chemical, 150 (2010) 517-522.
   doi:10.1016/j.snb.2010.09.003

9. T. Toccoli*, M. Tonezzer*, P. Bettotti, N. Coppedè, Silvia Larcheri, A. Pallaoro, L. Pavesi and S. Iannotta
   "Supersonic Molecular Beams Deposition of α-Quaterthiophene: Enhanced Growth Control and Devices Performances"
   Organic Electronics, 10, 3 (2009) 521-526.

10. L.C. Campos and M. Tonezzer, A.S. Ferlauto, L.O. Ladeira and R.G. Lacerda*
    "Epitaxially induced, low temperature growth of ZnO nanowires from solid Au-Zn catalyst",
    Advanced Materials, 20, (2008),1499.

Introduction

As its title announces, the general aim of this doctoral thesis is to investigate the growth and use of nanostructured materials in order to make them suitable for sensoristics.

Sensors applications have become very important in the last years because of a new sensibility towards pollution of the urban world and its effects on human health. Only very recently people and countries discovered the importance of environment preservation and monitoring. After a period of fast and uncontrolled industrial progress, we are now aware of this danger. Thus we need to monitor the environment and the changes which are happening directly or indirectly because of human presence.

During the last decades, solid-state gas sensors have played an important role in environmental monitoring and chemical process control [1]. The strong investigation which followed, made clear that the field of science and sensor technology cannot search for new sensor materials which are *ideal*, because different applications (e.g. different transformations of energy and different goals for sensors) require different materials. However materials are important drivers in sensor technology. The combination of the right materials (new or existing) to the right application can result in smarter, cheaper, or more reliable sensors.

In order to give a contribution to this important evolving situation, during these three years the PhD candidate investigated two of the most important areas related to nanostructured materials used in sensing applications.

On one side, the recent interesting field of **metal oxide nanowires** has been studied, both in terms of fundamentals (growth mechanism and structural properties) and sensor properties towards different gases. On the other side, the less exploited (in terms of sensor devices) field of **organic thin films** has been investigated, in terms of growth and fundamental properties (charge carriers mobility) which are required to use them as sensors.

While nanostructured metal oxides are already in use in commercial sensors (usually in the form of porous thick or thin films), organic materials are

[1] P.T. Mosley and B.C. Tofield, Solid State Gas Sensor, Hilger, Bristol, 1987.

still in a prototypal phase, and need further investigation in order to be effectively used. This different evolution step is reflected also in the present thesis: in which zinc and tin oxide nanowires are characterized as gas sensing devices, while molecular materials are only optimized towards a better order and a higher carrier mobility, which is one of the bottlenecks towards a higher response.

For this reason, the chapters concerning metal oxide nanowires will give a wide picture, from their growth mechanism to their structure until their use (in different architectures) in sensing applications. Oxide nanowires have been used as passive (resistive) sensors (they have been used also as active sensors, but such data are still under analysis) both in order to develop new real sensors, and to better understand the sensing mechanism behind the high response of such nanostructured materials.

Their nanoscale dimensions, comparable to the depletion layer, makes them almost ideal intrinsic *on-off* devices, and this can be exploited to fabricate a new generation of sensors characterized by a huge response. The problems of metal oxide sensors are however their poor selectivity and high working temperature. In this direction goes the investigation of the molecular materials.

Concerning the organic complement in this thesis, the aim of the experimental work was the optimization of the overall field effect mobility of carriers (holes) along the whole device, which means several microns (tens of microns, due to the impossibility to use standard lithography techniques on organic delicate materials).

This meant the minimization of grain boundaries, that are one of the steps hindering the charge carrier mobility, and even the recently found domain boundaries. Exploiting the high kinetic energy achievable by SuMBD, we found that it is partially transformed in surface mobility, increasing the order of the fundamental building blocks inside each monolayer, and decreasing the grain and domain boundary density (because of wider and less fractal grains).

At the end of the thesis we will show a first combination of the two families of materials, just as a sample of what the exploitation of the best

features of each family (high response for metal oxides and good selectivity for organic materials) can provide.

Chapter 1 will describe the main properties and characteristics of sensing materials, and sketch the structure of a sensor device. It will also define the main parameters commonly used to evaluate and compare the performance of sensing devices.

In Chapter 2 we will introduce the metal oxide semiconductors, and the way they interact with an analyte gas. We will then focus on zinc oxide nanostructures, discovering a novel growth mechanism.

In *Chapter 3* single tin oxide nanowires will be used to fabricate gas sensors whose response will be investigated as a function of the nanowire diameter. The so called depletion layer modulation model will be confirmed experimentally.

Chapter 4 will explain the basics of organic semiconductors, together with the peculiarities of the novel technique used: SuMBD (Supersonic Molecular Beam Deposition). The mechanism behind the growth of the first molecular monolayer will be studied, because this is the most important region in organic active devices like OFETs (Organic Field Effect Transistors).

In *Chapter 5* the growth of different molecular materials (three different small conjugated molecules: quaterthiophene, sexithiophene and pentacene) is analyzed as a function of the main deposition parameters. Both the sub-monolayer and the thin film growth are investigated. The performance of organic transistors is related to the growth and “crystallinity” of the material. Several cases of study will be presented.

In *Chapter 6* a first architecture involving both inorganic and organic materials (carbon microfibers and zinc oxide nanowires) is fabricated and presented as an example of future synergies for a next generation of nanostructured sensors.

Chapter 1

Gas sensing overview

1.1 Sensors and transducers

There is a lot of confusion in literature about gas sensing properties, because diverse authors use different definitions for the same quantity, or the same term is used with different meanings. Since the aim of this thesis is to investigate novel nanostructured materials in order to specifically use them as sensors, in this chapter I will describe precisely what a sensor is, and how its performance can be measured.

This task is, however, not as simple as it could seem. Although *sensor* is a common technical term that has been in frequent use only in the last decades, instruments working just like sensors have been in use ever since man first attempted to gather reliable information concerning his physical, chemical and biological environment.

During the last few years, by virtue of the rapidly increasing capabilities of microprocessors, the idea of constructing a technical analogue of human intelligence with the human senses has arisen. Since then, a tendency has risen to designate as *sensors* all instruments suitable for technical measurements of physical, chemical or biological quantities.

Hence one must be conscious of the fact that a number of different fields, each with its own historical background, are lumped together. It is therefore not surprising that no one unanimous concept of a sensor has yet been agreed upon in this heterogeneous community. However, at least some meaningful definition is essential for this work and it is possible to recommend one that follows the ANSI MC6.1 1975, “Electrical Transducers Nomenclature and Terminology” [1].

This standard, which has been prepared by the Instrument Society of America, defines a transducer as “a device which provides a usable *output* in

response to a specified *measurand*". Further, an *output* is defined as an "electrical quantity", and a *measurand* is "a physical quantity, property, or condition which is measured".

The main usable output, today, consists in some sort of electrical signal which lends itself to signal processing, the establishment of control loops, etc.. On the other hand, appears clear that there are a lot of possible measurands (temperature, pressure, speed etc..) which one can be interested to measure.

In any case, it is evident that in general the specified measurand is intrinsically different from the desired output signal. Thus, in order to convert the former quantity into the latter, at least one transduction principle has to be invoked to allow a sensor working.

Usually, these transduction principles are better known as physical or chemical effects. A dictionary of such effects has been compiled in 1980 by Ballentyne and Lovett [2], and more than 250 physical effects are to be found in 1984 in a dictionary by Schubert [3]. Although not all of them will be suitable for use in sensing applications, it is clear that some ordered scheme is necessary to classify this large number of effects. Lion [4] proposed the grouping of various principles according to the form of energy in which the signals are received and generated, thus ending up with a matrix-like arrangement.

He distinguished six classes of signals, that are: mechanical, thermal, electrical, magnetic, radiant and chemical. Considering each transduction principle as distinguishable by well-defined input and output signals which can be attached to the classes defined above, a 6x6 matrix will be required to list the various principles: Table 1.1 is a compiled number of principles which either have important applications in instrumentations, or are just instructive to visualize the basic systematic of this grouping.

Primary Signal \ Secondary Signal	Mechanical	Thermal	Electrical	Magnetic	Radiant	Chemical
Mechanical	(Fluid) Mechanical and Acoustic Effects: eg, Diaphragm, Gravity Balance, Echo Sounder	Friction Effects (eg, Friction Calorimeter) Coolings Effects (eg, Thermal Flow Meters)	Piezoelectricity Piezoresistivity Resistive, Capacitive, and Inductive Effects	Magnetomechanical Effects: eg, Piezomagnetic Effect	Photoelastic Systems (Stress-induced Birefringence) Interferometers Sagnac Effect Doppler Effect	
Thermal	Thermal Expansion (Bimetalic Strip, Liquid-in-Glass and Gas Thermometers, Resonant Frequency) Radiometer Effect (Light Mill)		Seebeck Effect Thermoresistance Pyroelectricity Thermal (Johnsen) Noise		Thermooptical Effects (eg, in Liquid Crystals) Radiant Emission	Reaction Activation eg, Thermal Dissociation
Electrical	Electrokinetic and Electromechanical Effects: eg, Piezoelectricity Electrometer Ampere's Law	Joule (Resistive) Heating Peltier Effect	Charge Collectors Langmuir Probe	Biot-Savart's Law	Electrooptical Effects: eg, Kerr Effect Pockels Effect Electroluminescence	Electrolysis Electromigration
Magnetic	Magnetomechanical Effects: eg, Magnetostriction Magnetometer	Thermomagnetic Effects: eg, Righi-Leduc Effect Galvanomagnetic Effects eg, Ettingshausen Effect	Thermomagnetic Effects: eg, Ettingshausen-Nernst Effect Galvanomagnetic Effects: eg, Hall Effect, Magnetoresistance		Magnetooptical Effects: eg, Faraday Effect Cotton-Mouton Effect	
Radiant	Radiation Pressure	Bolometer Thermopile	Photoelectric Effects: eg, Photovoltaic Effect Photoconductive Effect		Photorefractive Effects Optical Bistability	Photosynthesis, -dissociation
Chemical	Hygrometer Electrodeposition Cell Photoacoustic Effect	Calorimeter Thermal Conductivity Cell	Potentiometry, Conductimetry, Amperometry Flame Ionization Volta Effect Gas Sensitive Field Effect	Nuclear Magnetic Resonance	(Emission and Absorption) Spectroscopy Chemiluminescence	

Table 1.1: Physical and chemical transduction principles (from reference [5]).

1.2 Chemical sensors

Remembering the definition given in previous section, a chemical sensor can be viewed as a device which transforms chemical information (ranging from the concentration of a specific sample component to total composition analysis) into an analytically useful signal [6]. A chemical state is determined by the different concentrations, partial pressures or activities of particles such atoms, molecules, etc. to be detected in the gas, liquid or solid phase.

As depicted in Figure 1.1, chemical sensors can be conceptually subdivided into two basic functional units: a *recognition site* and a *transducer*. Some sensors may include an optional filter which prevent the interaction of the recognition site with the interfering particles.

The *recognition site* of a sensor transforms the chemical information into a form of energy which may be measured by the transducer.

The *transducer* is a device capable of transforming the energy carrying the chemical information about the sample into a useful analytical signal.

The *recognition sites* of a chemical sensors may be based upon various principles:

- *physical*, where no chemical reaction takes place;
- *chemical*, in which a chemical reaction with participation of the analyte gives rise to the analytical signal;
- *biochemical*, in which a biochemical process is the source of the analytical signal. They may be regarded as a subgroup of the chemical ones. Such sensors are called *biosensors*.

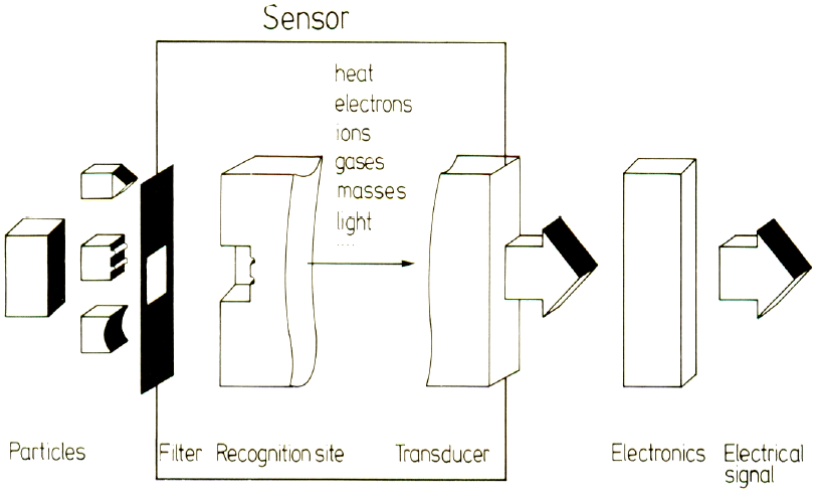

Figure 1.1: Simplified picture of a chemical sensors (from reference [6]).

Chemical sensors may be classified according to the operating principle of the transducer [7,8,9,10]:

1 Optical devices transform changes of optical phenomena, which are the result of an interaction of the analyte with the receptor part. This group may be further subdivided according to the optical which undergoes modifications in chemical sensors: *absorbance*, caused by the absorptivity of the analyte itself or by the reaction with some suitable indicator; *reflectance*, usually using an immobilized indicator;

luminescence, based on the measurement of the intensity of light emitted by a chemical reaction in the receptor system; *fluorescence*, which can change due to interactions with the analyte; *refractive index*, changing due to the change in the sensing material composition following the incorporation of the analyte.

2 Electrochemical devices transform the effect of the electrochemical interaction analyte-electrode into a useful signal. Such effects may be stimulated electrically or may result in a spontaneous interaction at the zero-current condition. The following subgroups may be distinguished: *voltammetric sensors*, including amperometric devices, in which current is measured in the direct current or alternate current mode; *potentiometric sensors*, including amperometric devices, in which the potential of the indicator electrode (ion-selective electrode, redox electrode, metal/metal-oxide electrode) is measured against a reference electrode; *chemically sensitized field effect transistor* (ChemFET) in which the effect of the interaction between the analyte and the active coating is transformed into a change of the source-drain current; *potentiometric solid electrolyte gas sensors*, differing from potentiometric sensors because they work in high temperature solid electrolytes and are usually applied for gas sensing measurements.

3 Electrical devices based on measurements where no electrochemical processes take place, but the signal arises from the change of electrical properties caused by the interaction with the analyte. This group includes: *metal oxide semiconductor sensors*, based on reversible redox processes of analyte gas components; *organic semiconductor sensors*, based on the formation of charge transfer complexes, which modify the charge carrier density; *electrolytic conductivity sensors*, *electric permissivity sensors*.

4 Mass sensitive devices transform the mass change at a specially modified surface into a change of a property of the support material. The mass change is caused by accumulation of the analyte. Two classes can be distinguished: *piezoelectric devices* are based on the measurement of the frequency change of the quartz oscillator plate caused by absorption of a mass of the analyte at the oscillator; *surface*

acoustic wave (SAW) devices depend on the modification of the propagation velocity of a generated acoustical wave affected by the deposition of a definite mass of the analyte.

5 Magnetic devices based on the change of paramagnetic properties of a gas being analyzed.

6 Thermometric devices based on the measurement of the heat effects of a specified chemical reaction or adsorption which involve the analyte.

This classification, even being the most used one, represents only one among the possible different options. For instances, in the past sensors have been classified not according to the primary effect but to the method used for measuring the effect [11, 12]; chemical sensors have also been classified according to the application to detect or determine a given analyte [13] or by the application way [14,15].

It is, of course, possible to use various classifications as long as they are based on clearly defined and logically arranged principles.

Gases are the key measurands in many industrial and domestic activities; therefore the application fields of chemical sensors are very broad [16,17,18]. Among these Göpel and Schierbaum have identified [6]:

1 Environmental control (air, water, soil);
2 Working area measurements (workplace, household, car, atc..)
3 Emission measurements (car, waste water, etc..)
4 Process control and regulation (biotechnological and chemical plants, fermentation processes, etc..)
5 Medical applications (clinical diagnostics, anaesthetics, veterinary)
6 Agricultural (analysis in agriculture and gardening, detection of pesticides, etc..)

Two important groups of applications which are generally distinguished in literature are:

- The detection of single gases (such as NO_x, NH_3, O_3, CO_x, CH_4, H_2, SO_2);
- The discrimination of gases/vapours mixtures (such as odours).

Single gas sensors can be used, for example, as fire detectors, leakage detectors, controllers of ventilation in cars or planes, devices for environmental pollution monitoring and alarm devices warning the overcoming of threshold concentration levels of hazardous gases in indoor applications.

Figure 1.2 shows, for instance, the concentration levels and thresholds of typical environmental polluting gases as legislated in Japan [19] while, as regard the context detection of odour and volatile organic compound (VOC) emissions, a brief list of widespread applications of chemical sensors developed during the past years is summarized in Table 1.2.

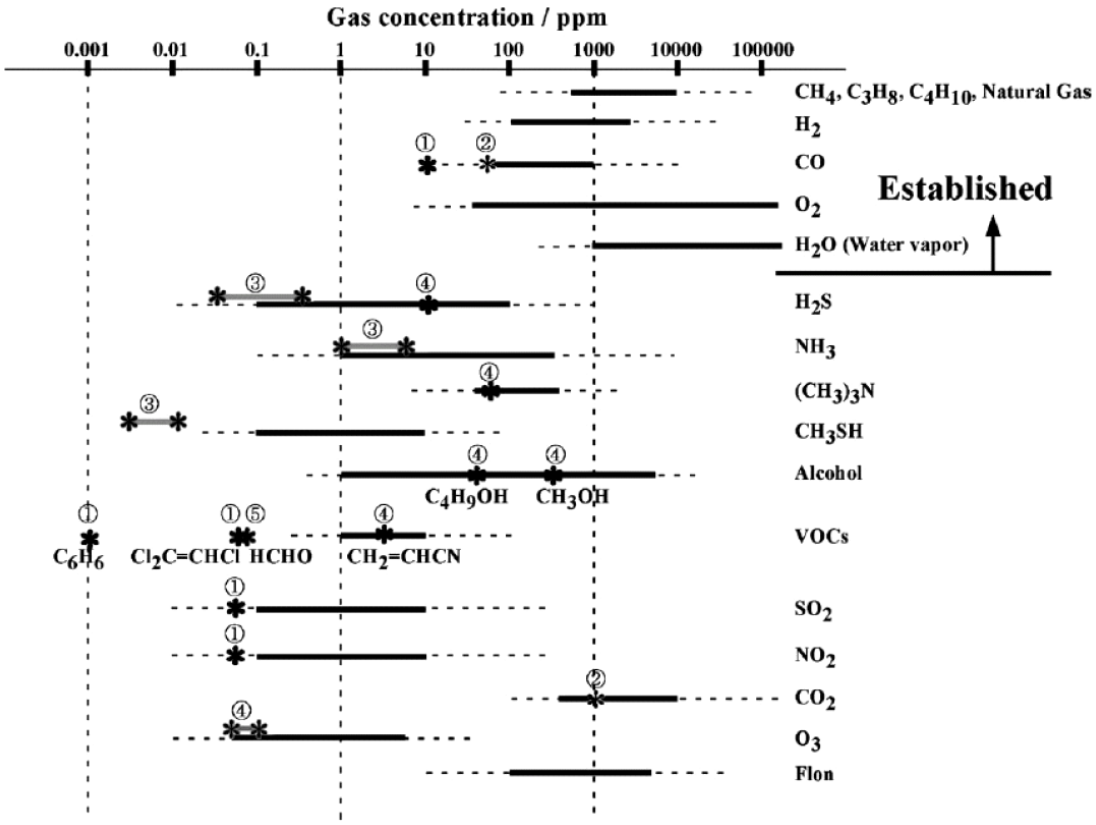

Figure 1.2: Concentration levels of typical gas components concerned. Star marks indicate the standards of the gases legislated in Japan by (1) Environmental Standard, (2) Ordinance on Health Standards in the Office, (3) Offensive Odour Control Law, (4) Working Environment Measurement Law, and (5) Ordinance by Ministry of Health, Labour and Welfare (from reference [19]).

	Application fields	Detection objects	Sensors
1	Environmental control	Propane, Propanol	Metal oxide sensor with multivariate analysis
		Solvent vapours (Pentane, Hexane, Heptane, etc..)	QCM with PCA and neural network
2	Measurements in working areas	Gas mixture analysis	MOSFET sensor with PCA and artificial neural network
		Harmful organic vapours detection	QCM sensors
3	Emission measurements	Waste water separation	Polypirrole sensors with multivariate analysis
		Ammonia emission	QCM sensor array
4	Process control and regulation	Bioreactor off-gas composition monitoring	MOSFET sensor with PCA
		Block milk products classification	Neotronics eNOSE electronic nose
5	Medical applications	Urine analysis	QCM sensor with PCA
		Human skin odour analysis	QCM sensors with self-organizing map (SOM) analysis
		Human breath analysis	Metal oxide sensors with signal pattern evaluation
6	Agricultural	Vinegar discrimination	AromaScan electronic nose
		Boar taint intensity discrimination	Conductiong polymer sensor array with pattern recognition routines

Table 1.2: Chemical sensor applications relevant to the odour and volatile organic compound (VOC) emissions detection (from reference [20]).

The detection of volatile organic compounds (VOCs) or smells generated from food or household products has also increasing importance in food industry and in indoor air quality; multi-sensor systems (often referred as electronic noses) are the modern sensing devices designed to analyze such complex environmental mixtures [21,22,23].

The electronic nose aims to emulate the mammalian nose by using an array of sensors that can simulate mammalian olfactory responses to aromas (Figure 1.3). Each sensor in the array behaves like a receptor by responding to different odours to varying degrees. The changes are transduced into electrical signals, which are pre-processed and conditioned before identification by a pattern recognition system. Some of the sensors used in

commercial electronic noses are reviewed in Table 1.3 together with their properties and limitations.

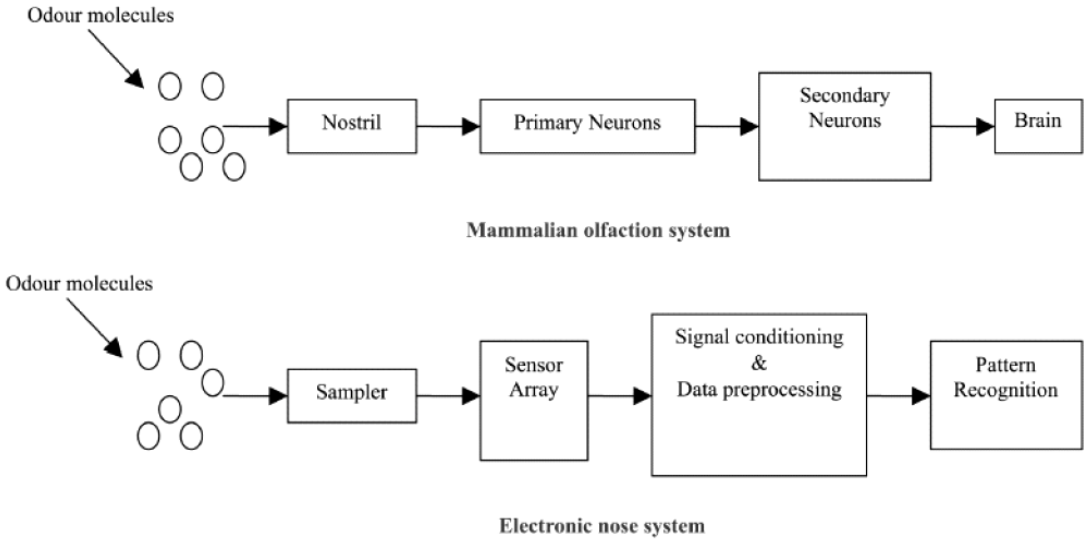

Figure 1.3: Comparison of the mammalian olfactory system and the electronic nose system (from reference [24]).

Sensor type	Measurand	Fabrication	Examples of sensitivity/detection range/detection limits (DL)	Advantages	Disadvantages
Polymer composites	Conductivity	Screenprinting, spincoating, dipcoating, spray coating, microfabrication	ppb for HVPG ppm for LVPG; 1 per cent $\Delta R/R_b$/ppm; DL ≤ 0.1-5 ppm	Operate at room temperature, cheap, diverse range of coatings	Sensitive to temperature and humidity
Intrinsically conducting polymers	Conductivity	Electrochemical, chemical polymerisation	0.1-100 ppm	Sensitive to polar analytes, cheap, good response times, operate at room temperature	Sensitive to temperature and humidity, suffer from baseline drift
Metal oxides	Conductivity	Screenprinting, RF sputtering, thermal evaporation, microfabrication	5-500 ppm	Fast response and recovery times, cheap	High operating temperatures, suffer from sulphur poisoning, limited range of coatings
SAW	Piezoelectricity	Photolithography, airbrushing, screenprinting, dipcoating, spincoating	1 pg to 1 mg of vapour 1 pg mass change; DL = 2 ppm for octane and 1 ppm NO_2 and 1 ppm H_2S with polymer membranes	Diverse range of coatings, high sensitivity, good response times, IC integratable	Complex interface circuitry, difficult to reproduce
QCM	Piezoelectricity	Micromachining, spincoating, airbrushing, inkjet printing, dipcoating	1.5 Hz/ppm; 1 ng mass change	Diverse range of coatings, good batch to batch reproducibility	Poor signal-to-noise ratio, complex circuitry
Optical devices	Intensity/ spectrum	Dipcoating	Low ppb; DL (NH_3)=1 ppm with polyaniline coating	Immune to electromagnetic interference, fast response times, cheap, light weight	Suffer from photobleaching, complex interface circuitry, restricted light sources
MOSFET	Threshold voltage change	Microfabrication, thermal evaporation	2.8 μV/ppm for toluene; DL = (amines, Sulphides) = 0.1ppm; Maximum response = 200 mV especially for amines	Small, low cost sensors, CMOS integratible and reproducible	Baseline drift, need controlled environment

Notes: HVPG – high vapor pressure gas; LVPG – low vapor pressure gas; $\Delta R/R_b$ – relative differential resistance change

Table 1.3: Summary of the sensors used in commercial electronic noses (from reference [24]).

1.3 Gas-sensor interaction

As previously stated, the first requirement for any kind of gas sensor lies in the interaction between the sensing material and the molecules of the detecting analyte (Figure 1.4).

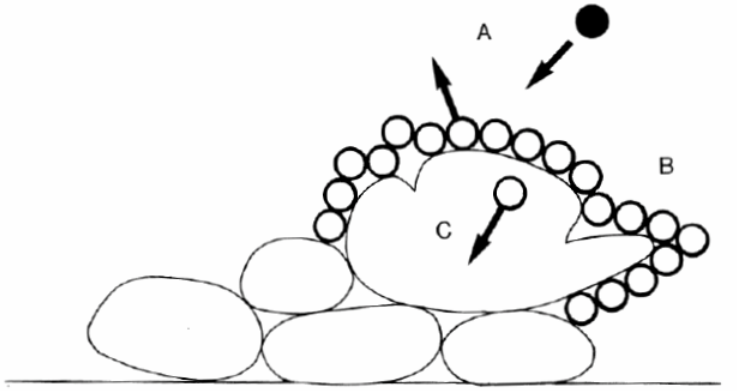

Figure 1.4: Simplified picture of some of the physical-chemical processes involved in the interaction of gases with a polycrystalline material. A) displacement; B) defects (structural and chemical); C) intra-crystallite diffusion; (from reference [25]).

The gas-sensor interaction consists in the gas adsorption at the sensing material surface generally followed by diffusion into the sensor bulk. In this paragraph the adsorption will be briefly described due to its strong relevance to the gas sensing process. Usually adsorption is distinguished as physical and chemical, the difference lying in the type of adsorbate-adsorbent interaction [26].

Physical adsorption is assumed to be a surface binding caused by polarization dipole-dipole Van der Waals interaction, whereas chemical adsorption arises from covalent forces with plausible involvement of electrostatic interaction. Most clearly the difference between physical and chemical adsorption can be traced in the curves of Lennard-Jones [27,28], describing the energy in the adsorbate-adsorbent system as a function of the distance between the particle and the surface (Figure 1.5).

There are two adsorption curves corresponding to physical (curve 1) and chemical (curve 2) adsorption. Here Q_i is the adsorption heat and r_i is the equilibrium distance determining the maximum of potential energy. In the case of chemisorption r is much smaller and Q is much larger than the corresponding values for physisorption. The potential barrier δE formed as a result of intersection of these two adsorption curves is often considered as an activation energy of transition from physically adsorbed state into the chemically adsorbed one.

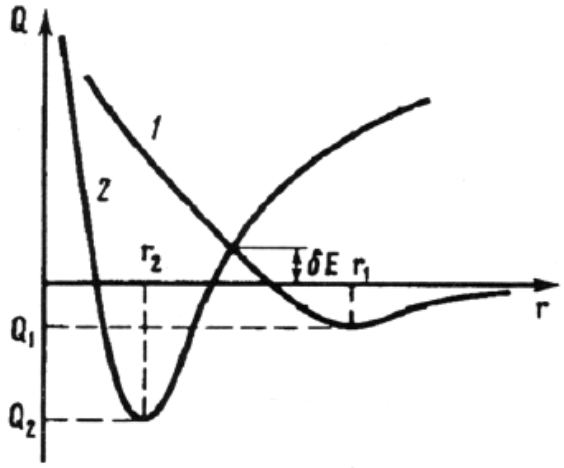

Figure 1.5: The diagram of potential energy according to Lennard-Jones (from reference [26]).

The classical method to investigate adsorption deals with establishing a correspondence between the amount of adsorbed gas at the equilibrium, the temperature and the partial pressure of the gas in the space surrounding the adsorbent. Usually, a constant temperature is maintained throughout an adsorption experiment. The shape of the obtained isotherms gives information on the character of adsorption.

In the most simple case of ideal, energy-homogeneous surface, the adsorption equilibrium of non-interacting particles is described by the Langmuir isotherm [29]:

$$\Theta = a'P/(1+a'P) \qquad (1.1)$$

where Θ is the surface coverage, i.e. the number of adsorbend molecules divided by the total number of adsorption sites, P is the gas pressure, $1/a' = v_0/\text{Prob.} \cdot (mkT)^{1/2} \cdot \exp(-Q/kT)$; v_0 is a rate constant, "Prob." is the probability that a molecule is adsorbed whenever it has both the energy E and a vacant site available, m is the molecular weight of an adsorbed particle, k the Boltzmann constant, T the absolute temperature and Q the adsorption heat. This isotherm describes a non-dissociation adsorption process with saturation corresponding to creation of a monomolecular layer.

At low pressures $a'p \ll 1$ and the Langmuir isotherm becomes the Hanry isotherm ($\Theta = a'p$) describing the domain of linear adsorption (see Figure 1.6).

The adsorption rate of a certain substance on a surface of a solid state is described by an equation of the type

$$d\Theta/dt = Ap(1-\Theta)e^{-E_A/kT} - B\,\Theta^{e-E_D/kT} \qquad (1.2)$$

where E_A and E_D are the activation energies of adsorption and desorption, A and B are constants containing leading factors, given by the theory of reaction rates and by the kinetic theory of gases. The leading term in the right-hand side of the previous equation describes the number of particles incident from the gaseous phase on a unit surface of adsorbent per unit time; the second term accounts for the amount of particles emitter into the gaseous phase.

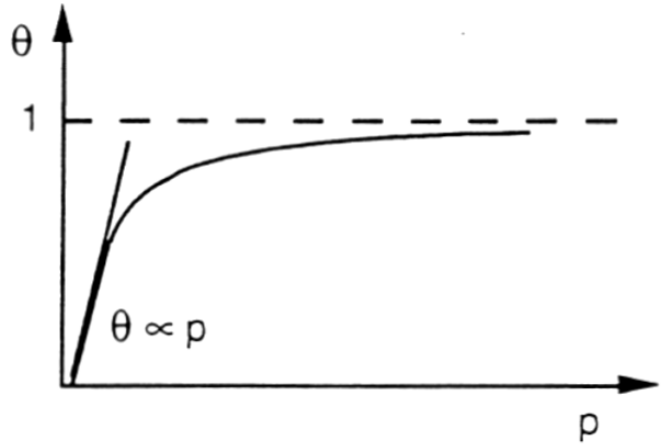

Figure 1.6: Percentage of occupied sites as a function of the pressure (from reference [25]).

According to the Langmuir theory, the previous equation can be written as

$$d\,\Theta/dt=K_o\cdot Sp/(2\pi mkT)^{1/2}\cdot(1-\Theta)\,e^{-E_A/kT}-v\,\Theta e^{-E_D/kT} \qquad (1.3)$$

where S is the surface occupied by a single adsorbed particle, v is the frequency of oscillation of an adsorbed particle and $K = K\exp(-E_A/kT)$ is the adhesion coefficient. An integration of the previous equation gives

$$\Theta(t)=P/(p+b)\cdot(1-e^{-K_1 t}) \qquad (1.4)$$

where $K_1=K_0\cdot Sp/(2\pi mkT)^{1/2}\cdot e^{-E_A/kT}+e^{-E_D/kT}$ and

$$b= v/K_0 S\cdot(2\pi mkT)^{1/2}\cdot e^{(E_A-E_D)/kT} \quad .$$

It must be observed that the Langmuir kinetics given by the previous equation are often violated. In many cases the data on the adsorption kinetics follow the Roginsky-Zeldovich-Elovich kinetics isotherm [30]:

$$\Theta(t)=A+B\cdot ln(1+ t/t_*) \qquad (1.5)$$

where A, B and t_* are constants dependending on the type of adsorbate-adsorbent pair.

The differential form of Elovich equation is given by:

$$d\,\Theta/dt = a\cdot\exp(-b\,\Theta) \qquad (1.6)$$

where a and b are constants.

1.4 Sensor parameters

In order to characterize the quality of the output signal produced by a sensor, some specific parameters are generally used [31,32,33,34,35,36]. The most

important parameters are intensity, reversibility, response and recovery times, sensitivity, specificity, selectivity, stability and dynamical range. The static and dynamic properties of a gas sensor are tested by means of experimental apparatuses capable to perform fast changes of the partial pressure of the gas "*I*" (p_i) [1].

Figure 1.7 shows the typical response signals *x'(t)* of a sensor during its exposure to two different analytes ("*1*" and "*2*") at partial pressures p_1 and p_2, respectively. The response of a "reliable" sensor to fast stepwise increases and decreases of p_1 and p_2 (Figure 1.7a) is shown in Figure 1.7b: the baseline has no drift ("C"); the signal rise $(dx' / dt)_{t0}$ upon gas exposure at t_0 is fast; the overall response time *t* or the 90% response time t_{90} upon exposure to p_1 ("D") is short; the measuring signal *x'* is stable ("E") and it is an unequivocal function of p_1 ; the signal decay after removing p_1 ("F") is fast.

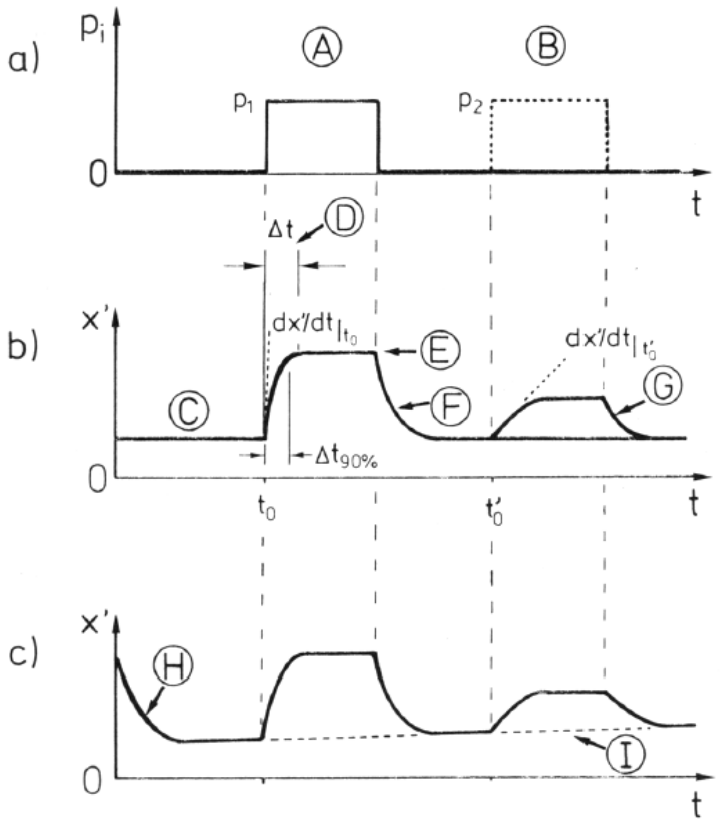

Figure 1.7: (a) Increases and decreases of the partial pressures p_1 and p_2 of two different gases "*1* " and "*2* "; (b) and (c) typical response signals of different gas sensors as a result of the pressure changes in (a). (from reference [6]).

In the case of non-specific sensors, the sensor yields a signal in the presence of gas 2 (“G”) introduced at time t'_0 as well. Figure 1.7c points out some typical practical problems of real gas sensors, which are drifts of the baseline after switching on the sensor (“H”) and during sensor operation over longer times (“I”). As shown in Figure 1.7b, independent signals may also be obtained from the slopes $(dx' / dt)_{t0}$ or $(dx' / dt)_{t'0}$ measured after exposure of the sensor to gas “1 ” or “2 ” at time t_0 or t'_0.

1.4.1 Intensity

The output signal produced by a sensing element exposed to a particular analyte atmosphere changes going from a stable signal S_0 (the output signal without analyte) to the another stable signal S (the stable output signal in presence of analyte). The module of the difference between these two values ($|S–S_0|$) is called the intensity of the response I.

This parameter, which is generally influenced by a number of different factors (i.e. the nature of the analyte, the nature of the sensing element, the temperature, the analyte concentration etc..), represents the primary parameter in the evaluation of the sensing capabilities of a sensor.

Nevertheless, taking into account that every signal is characterized by a signal noise, it appears clear that the sensing capabilities of a sensor depend also on the signal-to-noise ratio; in particular the response intensity has to be greater than the signal noise. At this purpose, Figure 1.8 shows the comparison between two responses characterized by the same response intensity, but by two different signal noises; it is easy to note that the response characterized by a lower noise level (Figure 1.8a) presents better sensing capabilities than the response characterized by higher noise level (Figure 1.8b). Taking into account this consideration, the parameter intensity/noise ratio is often used instead of the intensity parameter.

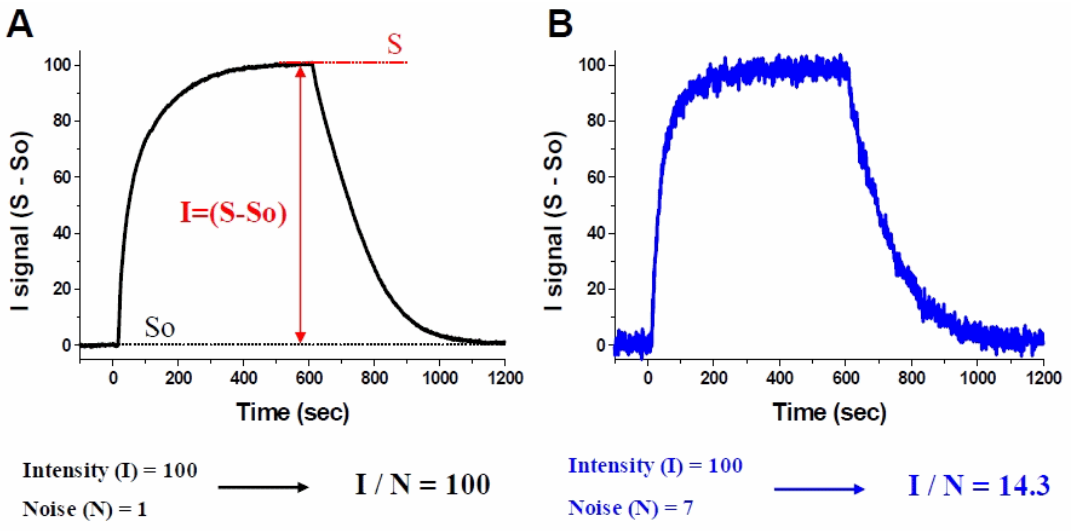

Figure 1.8: Explanation of the concept of intensity and intensity/noise ratio in sensors.

1.4.2 Reversibility

For a simplified data evaluation, time-independent and stable calibration curves are required: therefore the response signal must be reversible. In other words the output signal produced by a sensing element is demanded to return to its initial value (S_0) when the analyte atmosphere is removed.

This reversibility condition can be expressed, in the multi-dimensional cases where the response signal *x'* is a n-dimensional function of all the detected gases "*i* " with $1 \leq i \leq n$, by the following mathematical formula:

$$dx' = (\delta x'/\delta p_1)_{pj \neq 1,T} \cdot dp_1 + (\delta x'/\delta p_2)_{pj \neq 2,T} \cdot dp_2 + \ldots + \ldots (\delta x'/\delta p_i)_{pj \neq i,T} \cdot dp_i + \ldots + (\delta x'/\delta T)_{pj} \cdot dT$$

and hence $\S dx' = 0$ in the n-dimensional space.

For the case of two gases "1" and "2" this concept is well shown in Figure 1.9.

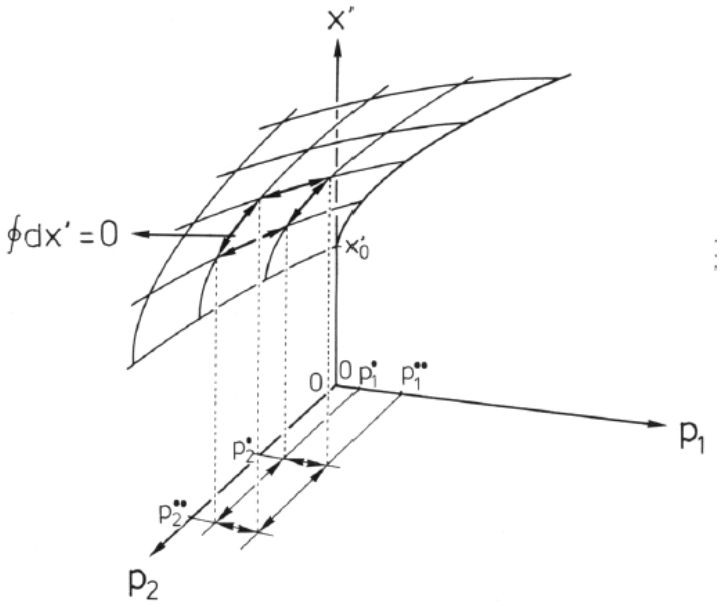

Figure 1.9: Response signal x' of a gas sensor as a function of partial pressures p_1 and p_2 of gases "1" and "2" (from reference [6]).

Over large ranges of pressures and temperatures this is usually not fulfilled, but for limited ranges the values x' are often found to be independent on the history of the sensor (Figure 1.9).

The empirical determination of the ranges of complete reversibility of a gas sensor is a very important task to test its potential future applications.

Taking into account the specific scope of this PhD work, where only mono-dimensional responses are treated, the reversibility process can be explained by introducing the recovery parameter *R* which is defined as the module of the difference between the signal after recovery (S_{AFT}) and the signal during analyte exposure (*S*). Figure 1.10 shows that the recovery *R* can be larger, equal or lower than the response intensity *I*.

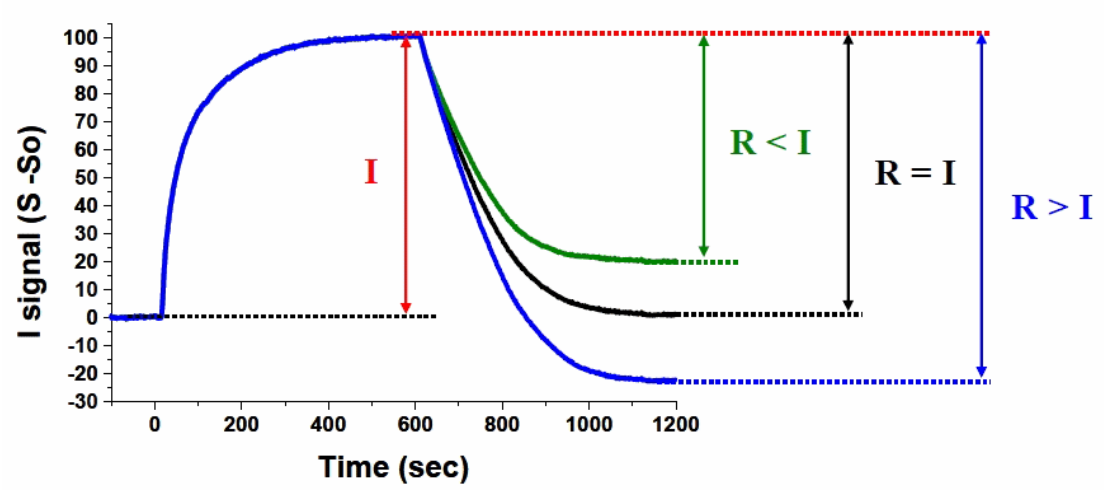

Figure 1.10: Explanation of the reversibility concept in sensors.

In order to evaluate the reversible degree of a sensor response, the percentage recovery degree *%R* will be used in this work, where:

$$\% R = |R-I| / I \times 100$$

It is worth noting that this mathematical formula points out that the *%R* is 100% when the process is completely reversible (*R* = *I*), while *%R* is <100% in both the cases in which *R* > *I* and *R* < *I*.

1.4.3 Response and recovery times

It takes time for any sensor to produce its full response upon the exposure to an analyte [37]. There are several causes for that, the most important of which is the diffusion time of the analyte inside the active material [38,39]. In order to establish the response speed of a sensor, which represent a primary topic in gas sensing field, response times *t* are generally used.

Response times *t* are defined as the times to achieve a certain percentage of the final change in the sensor signal upon exposure to the gas "1" at pressure p_1. The most used parameters are the t_{90} and t_{50}, defined respectively as the time to achieve the 90% (t_{90}) or 50% (t_{50}) of the final

change in the sensor signal. Similarly recovery times are the times to recover a certain percentage of the signal change after removal of analyte, where the most used parameters are t_{50} and t_{10}. These concepts are more clearly explained in the picture below.

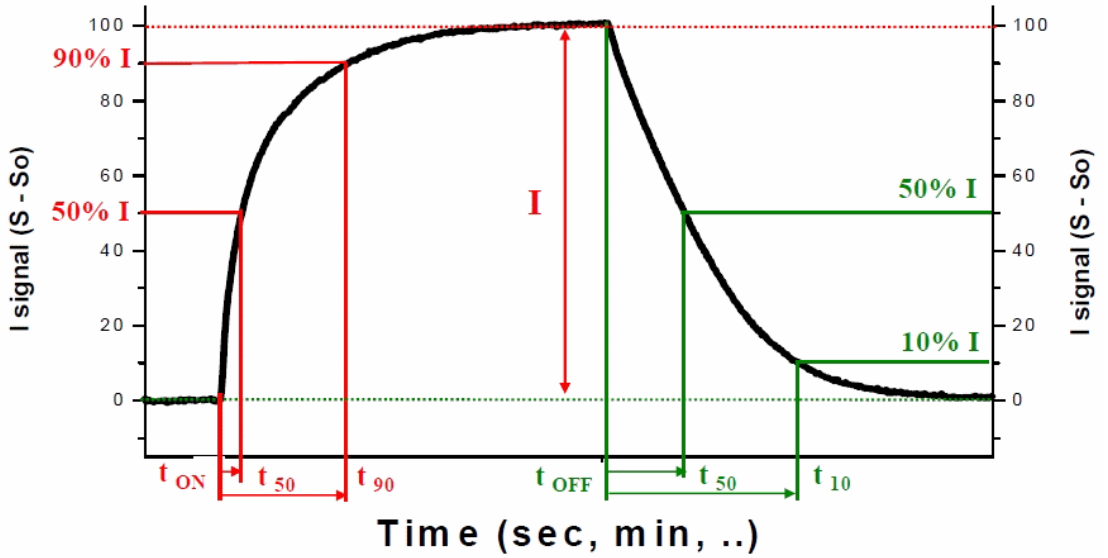

Figure 1.11: Explanation of the response times (t_{50}, t_{90}) and recovery times (t_{50},t_{10}) in sensors.

1.4.4 Sensitivity and calibration curves

As well shown in Figure 1.12, sensors give different responses (Figure 1.12a) upon exposures to different concentrated analyte atmospheres (Figure 1.12b); in particular, the response intensity increases at increasing concentration.

In order to establish the capability of a sensor to distinguish an analyte concentration from another one, the calibration curves and the concept of sensitivity have been introduced.

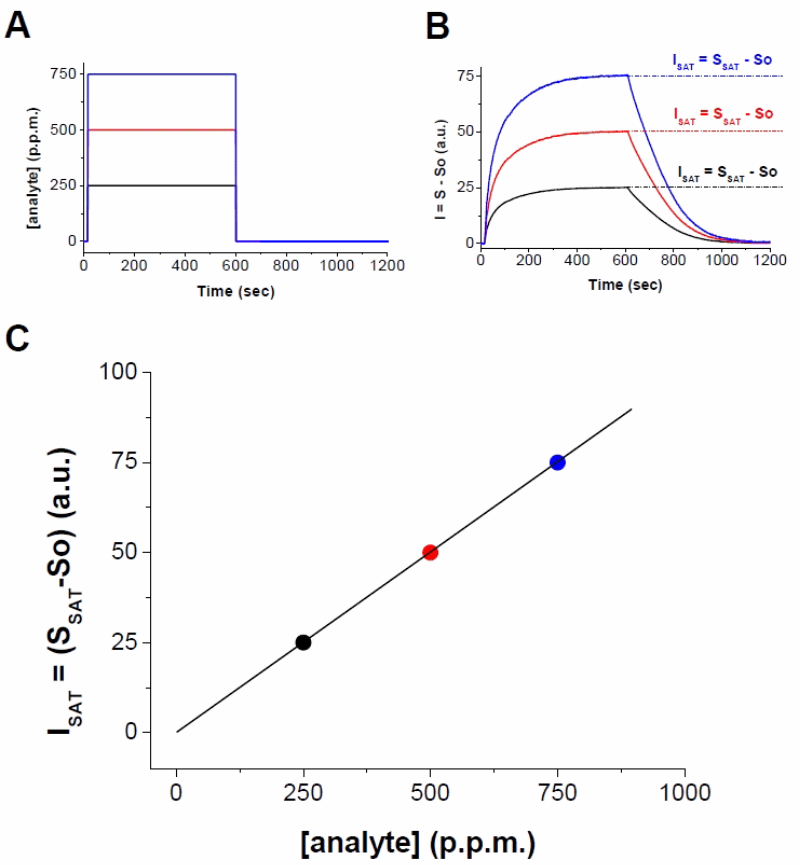

Figure 1.12: Explanation of sensitivity concept in sensors. Different analyte exposures (a), different responses (b) and the corresponding calibration curve (c) are reported.

The calibration curve of a sensor upon exposure to a certain analyte (Figure 1.12c) is obtained by reporting the values of analyte concentrations and of the corresponding response intensities on the abscissa and ordinate axis, respectively.

The sensitivity of a sensor is defined as [40]:

$$sensitivity = (I(c_1)-I(c_0))/(c_1-c_0)$$

where $I(c)$ is the response intensity of the sensor at the concentration c.

Obviously, the higher the sensitivity, the better the sensing capabilities of the sensor. For most practical sensor devices $x' = f(p1)$ is a non-linear function and γ_1 depends on p_1, as shown in Figure 1.13.

For this reason it is better to define the quantity using the incremental rapport, according to the following definition:

sensitivity (c) = $lim_{h\to 0}$(I(c+h)-I(c))/h=dI(c)/dc

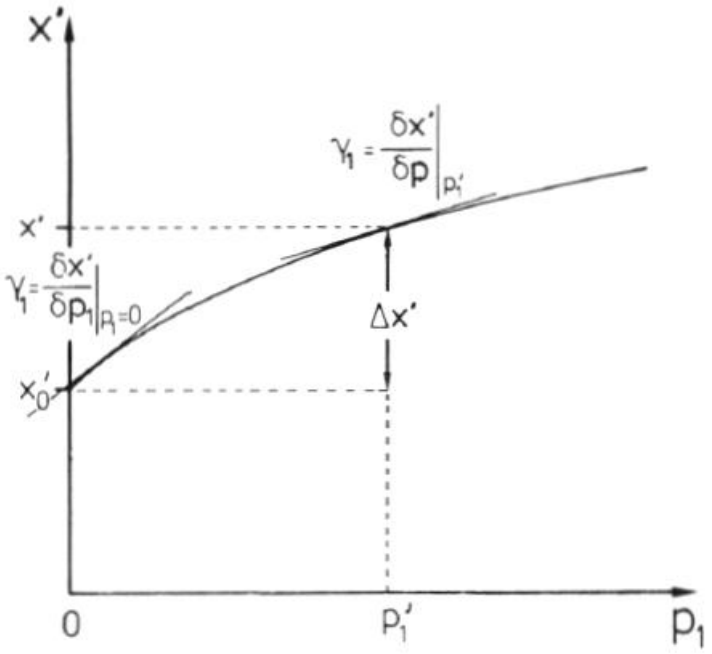

Figure 1.13: Calibration curve of a gas sensor after exposure to different partial pressures p_1 of a gas “1”. (from reference [6]).

However, for limited ranges of pressure of gas “1” the calibration curve is normally linear.

1.4.5 Specificity

A sensor is specific when only one of the different partial sensitivities $\delta x'/\delta p_i$ is large as compared to the others. A specific sensor can determine quantitatively the partial pressure p_i of the gas “*i* ”.

1.4.6 Selectivity

Selectivity Ξ of a sensor is usually defined by the ratio of the different partial sensitivities related to the gases to be monitored and to the interfering gases. Therefore, in the case of the selectivity of a sensor towards a particular gas "*i* " in the presence of the gases "*j* ", with $1 \leq j \leq n$ and $i \neq j$ it will be:

$$\Xi = \gamma_i / \gamma_{j \neq i} = (\delta x' / \delta p_i) / (\delta x' / \delta p_{j \neq i}).$$

1.4.7 Instabilities and drifts

Instabilities and drifts are important problems for a gas sensor because they affect its measurement accuracy. Non-cumulative drifts are related to statistical changes of the sensor signal, while cumulative drifts lead to irreversible changes of the calibration curves. On the other hand, short-term drifts may occur after switching the sensor on (see for example Figure 1.7c, "H"), but when the steady-state conditions are achieved, the drifts disappear. Long-term drifts are related to the stability of the baseline and are usually independent on the presence of the gases to be measured. Long-term drifts involve a periodic recalibration of the reference value x'_0 .

1.4.8 Dynamic range

The dynamic range of a sensor is characterized by the lowest detectable amount of a gas, which is related to the sensor noise, and by the maximum detectable amount which is for example limited by saturation effects of the sensor.

1.5 Materials in gas sensing field

Since the 1970's, when Bardeen et al. discovered [41] that gas adsorption onto a semiconductor produces a conductance change, a great amount of research was carried out in order to realize commercial semiconductor devices for gas detection. The microelectronic chemical sensor has been explored as a low-cost alternative to laboratory chemical sensing methods.

Initially the microelectronic sensor technologies are based on conductivity changes in a material in response to chemicals in the environment; the simplest of these conductivity-based sensors, the thin-film sensor, was first introduced into the research community in the early 1970's.

The thin-film sensor (Figure 1.14) is a film of chemically sensitive material, such as tin oxide [42,43], whose conductivity changes in response to reducing or oxidizing chemicals in the sensing environment.

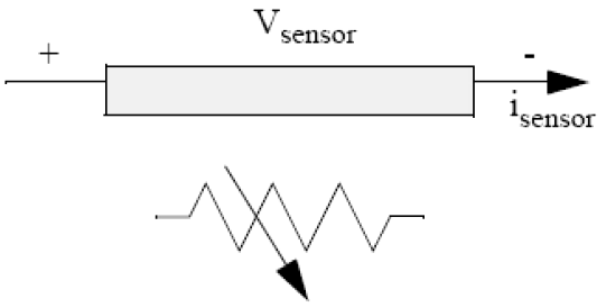

Figure 1.14: Basic structure of a conductivity based thin-film sensor.

The metal oxide thin films sensors are the only miniaturized chemical sensors that have significant impact in commercial markets. For example, tin oxide (SnO_2) [44,45] and iron oxide (Fe_2O_3) [46] have frequently been used to detect hydrocarbons and combustible gases in a variety of applications.

By far, the most popular of these sensors has been the Taguchi-type sensor, manufactured by Figaro Engineering in Japan; these sensors are made up of primarily tin oxide modified with various catalysts and additives to detect particular hazardous gases such as carbon monoxide and methane [47].

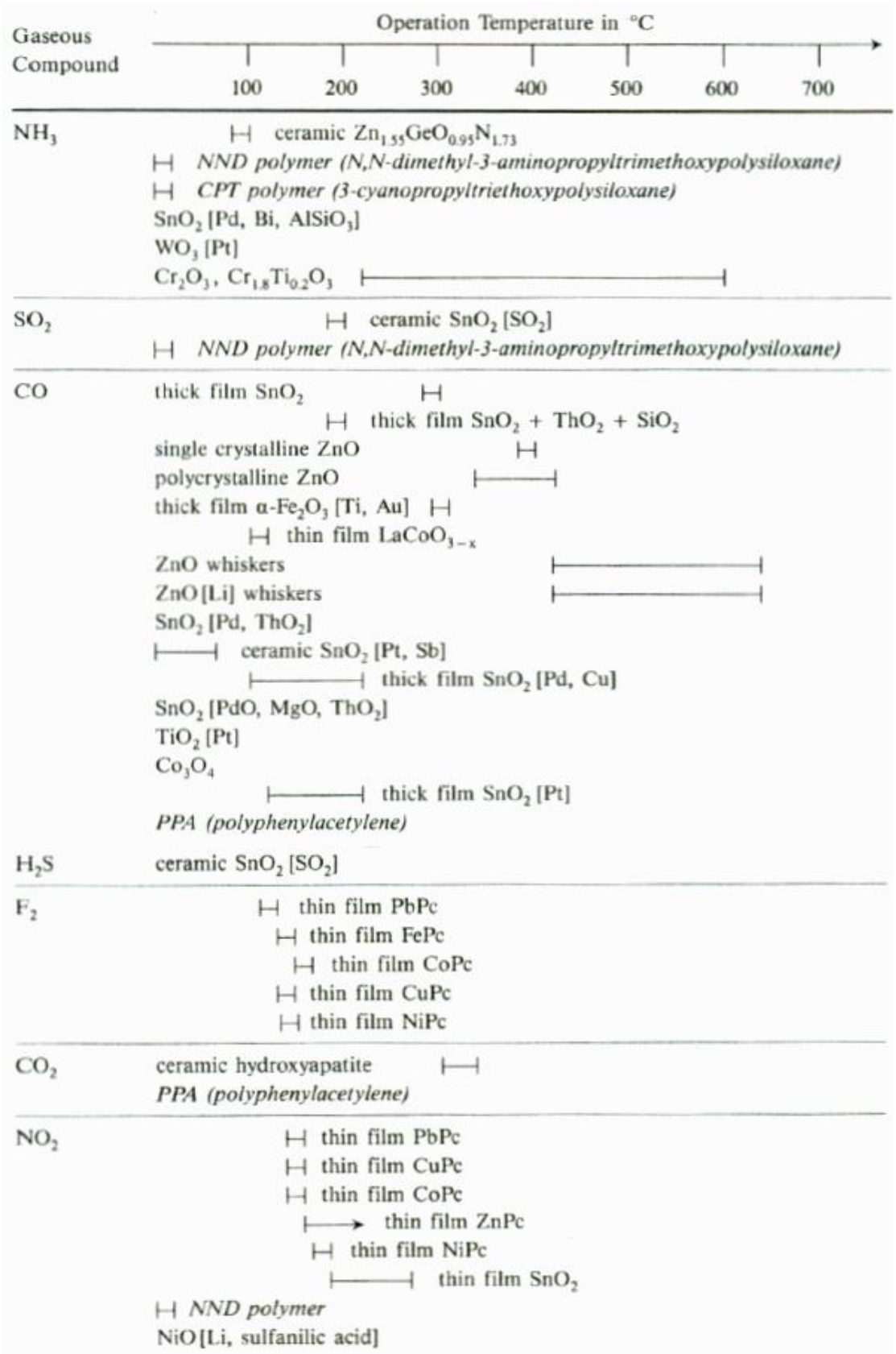

Table 1.4: Some chemically sensitive materials for the detection of environmental gases.

Thus, as previously reported, SnO_2 has been the most investigated material, the first devices being based on a thick film or ceramic layer of tin oxide. Nevertheless many other metal oxides, such as TiO_2 [48,49], ZnO [50,51,52], CeO_2 [53,54], Cu_2O [55], Nb_2O_5 [56], Ga_2O_3 [57] have been studied aiming their utilization as sensing material in gas sensing field; binary compounds, such as $SrTiO_2$ [58] and $BaTiO_3$ [59], have been also studied for these purposes.

Owing to the growing importance to gas sensing applications and the basic role which the materials play in this research field, in the last decades great attention has been spent from the scientific community in the study of innovative materials going beyond the metal oxide classes and pushing on as far as the organic materials. In fact, several organic materials have been used for gas sensing applications, such as polyethylene [60], PVC [61], polyimides [62] and phthalocyanines [63]. In Table 1.4 some examples of chemically sensitive materials for the detection of environmental gases are reported.

As previously said, the aim of this thesis is to investigate and optimize the sensing properties of inorganic nanostructures (metal oxides nanowires) and organic nanomaterials (quasi-crystalline molecular thin films), towards novel hybrid architectures which can exploit a synergy of their strong points.

[1] *Electrical Transducers Nomenclature and Terminology*, ANSI Standard MC6.1-1975 (ISA S37.1) Research Triangle Park, NC, Instrument Society of America (1975)

[2] D. Hesse, H. Kuttner, *Industrie-Elektrik und Elektronik*, 28 (1983) 36.

[3] J. Schubert, *Physicalische Effekte*, Weinheim, FRG: Physik-Verlag, 1984.

[4] K.S. Lion, *Transducers: Problems and Prospects*, IEEE Transaction IECI-16 (1969).

[5] R.L. Smith, The Engineering Handbook, Chapter 151 Sensor and Transducers, Second Edition, 2005, California

[6] W. Göpel, K.D. Schierbaum, in *Sensors: A comprehensive survey*, Eds. W. Göpel, T.A. Jones, M. Kleitz, J. Lundström, T. Seiyama, VCH Publishers In, NewYork, 1991, Vol. 2, p. 1.

[7] Proceedings of the *International Meeting on Chemical Sensors*, Fukuoka, Japan, Sept. 19-22, 1983; Editors: T. Seyma, K. Fueki, J. Shiokawa and S. Suzuki, Elsevier-Kodanscha, Amsterdam and Tokyo, 1983.

[8] H. Wohltjen, *Anal. Chem.* 87 A (1984) 56.

[9] T.E. Edmonds (ed.=, Chemical Sensors, Blackie and Sons Ltd., London, 1988.

[10] J. Janata, R.J. Huber (eds.), *Solid State Chemical Sensors*, Academic Press., New York, 1985.

[11] C. Nylander, *J. Phys. Sci. Instr.*, 18 (1985) 736.

[12] J. Janata, A. Bezegh, *Anal. Chem.*, 60 (1988) 62.

[13] S. Middlehoek, *Sens. Actuators* 10 (1986) 142.

[14] F. Scheller, F. Schubert, D. Pfeiffer, R. Hintsche, I. Dransfeld, R. Renneberg, U. Wollenberger, K. Riedler, M. Pavlova, M. Kuhn, H.G. Muller, P.M. Tan, W. Hoffmann, W. Moritz, *Analyst* 114 (1989) 653.

[15] M.A. Arnold, M.E. Meyerhoff, *Anal. Chem.* 20 (1988) 149.

[16] G. Sberveglieri (ed.) *Gas Sensors – Principles, Operation and Developments*, Kluwer Academic Publisher, Dordrecht (1992).

[17] J. Chou (ed.), *Hazardous Gas Monitors – A Practical Guide to Selection, Operation and Applications*, SciTech Publishing (2000).

[18] S. Capone, A. Forleo, L. Francioso, R. Rella, P. Siciliano, J. Spadavecchia, D.S. Presicce, A.M. Taurino, *J. Optoelectr. Adv. Mater.* 5 (2003) 1335.

[19] N. Yamazoe, *Sens. Actuators B 108* (2005) 2.

[20] A. Yuwono, P. Schulze Lammers, Agricoltural Engineering International: the CIGR Journal of Scientific Research and Development, Vol. VI, Uly, 2004.

[21] J.W. Gardner, K.C. Persuad (eds.), *Electronic Noses and Olfaction* (2000): 7th Symposium on Olfaction and Electronic Noses, Brighton, UK, July 2000, IOP Publishing (2001).

[22] J.W. Gardner, P.N. Barlett, *Electronic Noses – Principles and Applications*, Oxford University Press., 1999.

[23] P. Mielle, F. Marquis, C. Latrasse, *Sens. Actuators B* 69 (2000) 287.

[24] K. Arshak et al., *Sensor Rev.* 24 (2004) 181.

[25] G. Guillaud, J. Simon, J.P. Germani, *Coord. Chem. Rev.* 178-180 (1998) 1433.

[26] L. Yu, Kupriyanov, *Semiconductor sensors in physico-chemical studies*, Elsevier Science BV, Amsterdam, 1996.

[27] J.E. Lennard-Jones, *Trans. Faraday Soc.* 28 (1932) 333.

[28] J.E. Lennard-Jones, *Proc. Roy. Soc. A* 106 (1924) 463.

[29] I. Langmuir, *J. Am. Chem. Soc.* 38 (1916) 2221.

[30] S. Yu. Elovich, G.M. Zhalrova, *Zhur. Fizich. Khim.* 13 (1939) 1761.

[31] H.N. Norton, *Sensor and Analyzer Handbook*, Englewood Cliffs, NJ: Prentice Hall, 1982.

[32] *Terms and Definitions in Industrial-Process Measurement and Control*, IEC 65-Secretariat-84 draft, International Electrotechnic Committee, 982; and VDI/VDE 2600, Metrologie, Dusserdolf, 1973.

[33] H.L. Chau, K.D. Wise, *IEEE Trans. Electron Devices* ED-34 (1987) 859.

[34] P.R. Gray, R.G. Meyer, *Analysis and Design of Analog Intergated Circuits*, New York, Wiley, 1986.

[35] B.P. Lathi*, Signals, Systems and Communications*, New York: Wiley, 1961.

[36] R. E. Tasker, *Sensors* (1988) 22.

[37] M. Horn, *Sens. Actuators B* 26-27 (1995) 217.

[38] G. Boisdè, A. Harmer, in G. Boisdè, A. Harmer (Eds.), *Chemical and Biochemical Sensing with Optical Fibers and Waveguides*, Artech House, Inc. Boston, 1996, p. 113.

[39] O. Worsfold, C.M. Dooling, T.H. Richardson: *Colloids and Surfaces A* 198-200 (2002) 859.

[40] M. Tabib-Azar, in T. Grandke, W.H.Ko (Eds.), *Sensors: A Comprehensive Survey*, Verlagsgesellschaft, Weinheim, 1989, 18.

[41] W.H. Brattain, J. Bardeen, *Bell. Syst. Tech. J.*, 32 (1953) 1.

[42] G. Heiland, D. Kohl, Physical and chemical aspects of oxidic semiconductor gas sensors, in T. Seiymana (ed.), *Chemical Sensor Technology*, Vol. 1, Kodansha, Tokyo/Elsevier, Amsterdam, 1988.

[43] W. Gopel, *Future trends in the developments of gas sensors*, in G. Sberveglieri (ed.), Gas Sensors, Kluwer, Dordrecht, 1992, Ch. 11, 365.

[44] V. Demarne, R. Sanjines, D. Rosennfeld, F. Levy, A. Grisel, Sens. *Actuators B*, 6-7 (1992) 704.

[45] G.N. Advani, A.G. Jordan, *J. Electron. Mater.*, 9 (1980) 29.

[46] G. Sberveglieri, *Sens. Actuators B* 23 (1995) 103.

[47] N. Taguchi, *Gas detecting element and methods of making it*, US Patent No. 3644795 (1972).

[48] U. Kirner, K.D. Schierbaum, W. Gobel, B. Leibold, N. Nicoloso, W. Weppner, D. Fisher, W.F. Chu, *Sens. Actuators B* 1 (1990) 103.

[49] A. Bernasik, M. Radecka, M. Rekas, M. Sloma, *Appl. Surf. Sci.* 65-66 (1993) 240.

[50] U. Lampe, J. Muller, *Sens. Actuators B*,18 (1989) 269-284.

[51] G. Sberveglieri, P. Nelli, S. Groppelli, F. Quaranta, A. Valentini, L. Vasanelli, Mater. *Sci. Eng. B* 7 (1990) 63.

[52] G. Sberveglieri, S. Groppelli, P. Nelli, F. Quaranta, A. Valentini, L. Vasanelli, *Sens. Actuators B* 7 (1992) 747. 150

[53] M. Fleisher, H. Meixner, *Sens. Actuators B* 4 (1991) 437.

[54] H.J. Beie, A. Gnorich, *Sens. Actuators B* 4 (1991) 393.

[55] M. Ristov, G.J. Sinadinovski, M. Mitreski, *Thin Solid Films*, 167 (1988) 309.

[56] H. Kondo, H. Takahashi, T. Takeuci, I. Igarashi, *Proc. 3rd Sensor Symp.*, Japan, 1983, 185.

[57] S. Enzo, P.P. Macrì, G. Sbervegleri, S. Groppelli, C. Perego, *Appl. Surf. Sci.* 65-66 (1993) 277-282.

[58] J. Gerblinger, H. Meixner, *J. Appl. Phys.*, 67 (12) (1990) 7453.

[59] U. Lampe, J. Gerblinger, H. Meixner, Sens. Actuators B 7 (1992) 787.

[60] E. Bakker, P. Buhlman, E. Pretsch, *Chem. Rev.* 97 (1997) 3083.

[61] M. Reza Ganjali, P. Norouzi, F. Faridbod, M. Yousefi, L. Naji, M. Salavati-Niasari, *Sens. Actuators B* 120 (2007) 494.

[62] A. Quaranta, S. Carturan, M. Bonafini, G. Maggioni, M. Tonezzer, G. Mattei, C. de Julian Fernandez, G. Della Mea, P. Mazzoldi, *Sens. Actuators B* 118 (2006) 393.

[63] G. Maggioni, S. Carturan, M. Tonezzer, M. Bonafini, A. Vomiero, A. Quaranta, C. Maurizio, F. Giannicci, A. Scandurra, F. Dacapito, G. Della Mea, O. Puglisi, *Chem. Mater.* 19 (2006) 1726.

Chapter 2

Metal oxide nanostructures

Chemical and biological sensors have nowadays acquired a strong influence in many areas: personal safety, public security, medical diagnosis, detection of environmental toxins, semiconductor processing, agriculture, automotives, aerospace industries [1,2,3,4]… During the past few decades there has been a strong development of several simple, robust, solid-state sensors whose operation is based on the transduction of the binding of an analyte at the active surface of the sensor to a measurable signal that most often is a change in the resistance or capacitance of the active element.

The evolution of gas sensors is closely following developments in microelectronics because the architecture of sensing elements is influenced by design trends in planar electronics, and one of the major goals of the field is to design nano-sensors that could be easily integrated with modern electronic fabrication technologies.

For example, the current goal is the replacement of the large arrays of macroscopic individual gas sensors used for many years for multi-component analysis (each having its associated electrodes, filters, heating elements, and temperature detection) with an “electronic nose” embodied in a single device that integrates the sensing and signal processing functions in one chip [5,6,7,8].

Multi-component gas analysis with these devices is accomplished by pattern recognition analogous to odour identification by highly evolved organisms (Figure 2.1) [9,10,11].

By increasing the sensitivity, selectivity, the number of sensing elements, and the power of the pattern recognition algorithms, one can envision a potent device that can detect tiny quantities (ultimately few or even one molecule) of an explosive, biohazard, toxin, or an environmentally sensitive substance against a real, complex and changing background, then signal an alert or take “intelligent” actions.

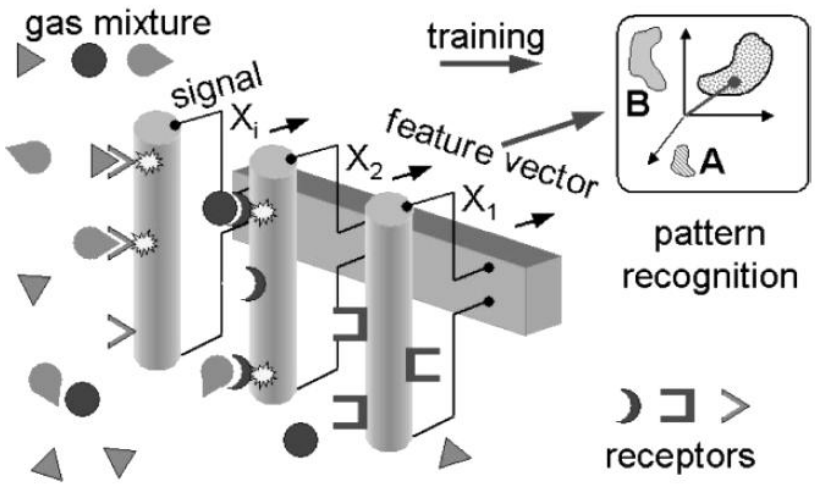

Figure 2.1: A simple sketch of a nanowire-based electronic nose. The nanowire surfaces are functionalized with different molecule-selective receptors. The operation is based on molecular selective bonding, signal transduction, and odour detection through complex pattern recognition.

However, this requires an increase in the sensitivity and selectivity of active sensor elements despite the loss of active area and the increased proximity of neighbouring individual sensing elements as the individual components are miniaturized. Recent progress in materials science and the many new sensing paradigms originating out of nanoscience and nanotechnology, particularly from *bottom-up* fabrication, makes scientists optimistic that these goals are within reach.

Metal oxides show a wide range of electronic, chemical, and physical properties that are often highly sensitive to changes in their chemical environment. Because of these properties, metal oxides have been widely studied, and most commercial sensors are based on appropriately structured and doped oxides. Nevertheless, much new science awaits discovery, and novel fabrication strategies remain to be explored in this class of materials by using strategies based on nanoscience and technology. Traditional sensor fabrication methods make use of pristine or doped metal oxides configured as single crystals, thin and thick films, ceramics, and powders through a variety of detection and transduction principles, based on the semiconducting, ionic

conducting, photoconducting, piezoelectric, pyroelectric, and luminescence properties of metal oxides [4,12,13,14].

Chemical and biological sensors having nanostructured metal oxides (and especially metal-oxide nanowires) benefit from the comprehensive understanding that exists of the physical and chemical properties of their macroscopic counterparts [15].

This chapter will be limited mainly to semiconducting devices with quasi-one-dimensional nanostructures such as nanowires and nanorods. Likewise, we restrict ourselves to two related device configurations: conductometric elements and field effect transistors.

Numerous quasi-one-dimensional oxide nanostructures with useful properties, compositions, and morphologies have recently been fabricated using so-called *bottom-up* synthetic routes. Some of these structures could not have been created easily or economically using *top-down* technologies.

A few classes of these new nanostructures with potential as sensing devices are summarized schematically in Figure 2.2. These achievements in oxide one-dimensional nanostructure synthesis and characterization were reviewed by Xia et al. [16] and others elsewhere [17,18,19].

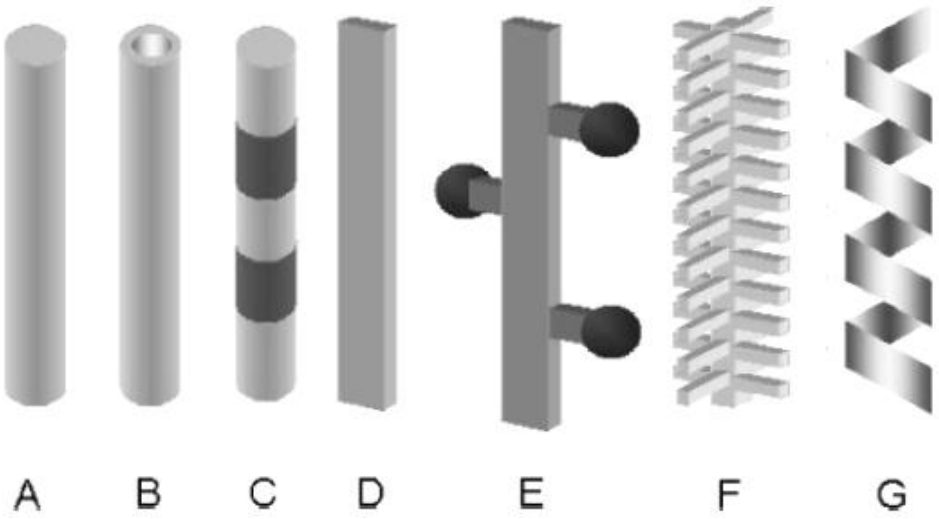

Figure 2.2: Schematic summary of the kinds of quasi-one-dimensional metal oxide nanostructures already reported (see references [16,17]). (A) nanowires and nanorods; (B) nanotubules/nanopipes and hollow nanorods;

(C) heterostructures; (D) nanobelts/nanoribbons; (E) dendrites, (F) hierarchical nanostructures; (G) nanosprings.

The properties of bulk semiconducting oxides have been extensively studied and documented in the past decades. Not so those of quasi-one-dimensional oxide nanostructures, which are demonstrating to possess novel characteristics for the following reasons:

(*a*) A large surface-to-volume ratio means that a significant fraction of the atoms or molecules in such systems are surface atoms that can participate in surface reactions.

(*b*) The Debye length λ_D (a measure of the field penetration into the bulk) for most semiconducting oxide nanowires is comparable to their radius over a wide temperature and doping range, which causes their electronic properties to be strongly influenced by processes at their surface. As a result, one can envision situations in which a nanowire's conductivity could vary from a fully nonconductive state to a highly conductive state entirely on the basis of the chemistry transpiring at its surface. This results in better sensitivity and selectivity. For example, sensitivities up to 10^5-fold greater than those of comparable solid film devices have already been reported for sensors on the basis of individual In_2O_3 nanowires [20]. The signal-to-noise ratio obtained indicates that ~10^3 molecules can be reliably detected on a 3 μm long device. By shortening the conductive channel length to ~30 nm, the adsorption of as few as 10 molecules could, in principle, be detected.

(*c*) The average time it takes photo-excited carriers to diffuse from the interior of an oxide nanowire to its surface (~10^{-12}-10^{-10} seconds) is greatly reduced with respect to electron-to-hole recombination times (~10^{-9}-10^{-8} seconds). This implies that surface photoinduced redox reactions (Figure 2.3) with quantum yields close to unity are routinely possible on nanowires. The rapid diffusion rate of electrons and holes to the surface of a nanostructure provides another opportunity as well.

The recovery and response times of conductometric sensors are determined by the adsorption-desorption kinetics that depends on the operation temperature. The increased electron and hole diffusion rate to the surface of the nanodevice allows the analyte to be rapidly photo-desorbed from the surface (~a few seconds) even at room at temperature.

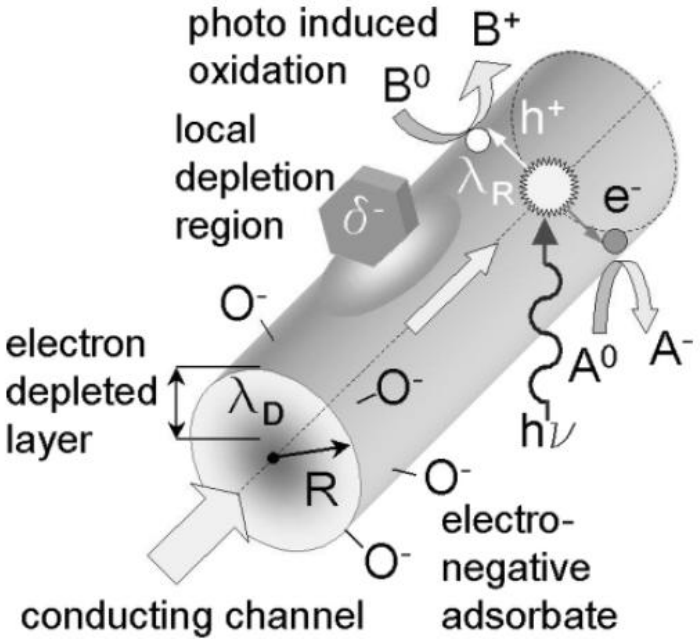

Figure 2.3: A summary of a few of the electronic, chemical, and optical processes occurring on metal oxides that can benefit from reduction in size to the nanometre range.

(*d*) Semiconducting oxide nanowires are usually stoichiometrically better defined and have a greater level of crystallinity than the multigranular oxides currently used in sensors, potentially reducing the instability associated with percolation or hopping conduction.

(e) Nanowires are easily configurable as field-effect transistors (FETs) and potentially integratable with conventional devices and fabrication techniques. Configured as a three-terminal FET, the position of the Fermi level within the bandgap of the nanowire could be varied and thus used to alter and control surface processes electronically.

(*f*) Finally, as the diameter of the nanowire is reduced, or as its materials properties are modulated either along its radial or axial direction, one can expect to see the onset of progressively more significant quantum effects [21].

2.1 Surface reactions on one-dimensional oxides

The exploration of the metal-oxide nanostructures as a platform for chemical sensing is a quite recent. Yang and co-workers fabricated and tested the performance of individual SnO_2 single-crystal nanoribbons configured as four-probe conductometric chemical sensors both with and without concurrent UV irradiation [22]. Photoinduced desorption of the analyte can lead to rapid detection and reversible operation of a sensor even at room temperature.

A detection limit ~3 ppm and response/recovery times of the order of seconds were achieved for NO_2.

A wide array of potentially useful one-dimensional metal-oxide nanostructures, including nanobelts, were synthesized and characterized in Wang's group [19,23] and in other laboratories [16,17]. Comini et al. [24] configured groups of the SnO_2 nanobelts between platinum interdigitated electrodes and assessed their behaviour at 300-400°C under a constant flux of synthetic air.

The nanobelt sensors showed excellent sensitivity toward CO, ethanol, and NO_2. NO_2 could be detected down to a few parts per billion.

Individual SnO_2 and ZnO single-crystalline nanobelts (30-300 nm width and 10-30 nm thickness) [23] were configured as FETs and studied by Arnold et al. [25]. The electrical properties of these individual nanobelts in vacuum, in air, and under oxygen, as a function of thermal treatment, suggested that the oxygen adsorption and desorption dynamics depends sensitively on the concentration of surface oxygen vacancies, which, in turn, affect the electron density in the nanobelt. The conductance of single nanowires exposed to 200 ppm of NO_2 (an oxidizing gas) at room temperature dropped by ~30%.

Kolmakov et al. used nanoporous alumina as a template for synthesizing arrays of parallel Sn nanowires, which were converted to polycrystalline SnO_2 nanowires of controlled composition and size [26].

Conductance measurements on these individual nanowires were carried out in inert, oxidizing, and reducing environments in the temperature range ~25-300°C [27].

At high temperatures and under an inert or reducing ambient, the nanowires behaved as highly doped semiconductors or quasi-metals with high conductances that depended weakly on temperature. When exposed to oxygen, the nanowires were transformed to weakly doped semiconductors with a high conductance activation energy. The switching between the high and low conductance states of the nanowires was fully reversible at all temperatures.

Configured as a CO sensor, a detection limit of ~a few 100 ppm for CO in dry air and at 300°C was measured with these SnO_2 nanowires, with sensor response times of ~30 s.

The above observations can be largely accounted for in terms of mechanisms developed over many years to explain the function of polycrystalline metal-oxide gas sensors [28,29,30,31]. This mechanism is outlined below, using SnO_2 nanowires in the presence of oxygen (an electron acceptor) and CO (an electron donor) as a model system for oxide semiconductor systems more generally. Specific departures from this general picture are pointed out for individual cases and for other surface adsorbate molecules when necessary.

The surface of stoichiometric tin oxide (a large bandgap semiconductor) is relatively inert. Even moderate annealing in vacuum, or under an inert or reducing atmosphere, causes some of the surface oxygen atoms to desorb, leaving behind oxygen vacancy sites (Figure 2.4). Likewise, exposure to UV results in oxygen photodesorption (or of other surface species) even at low temperatures.

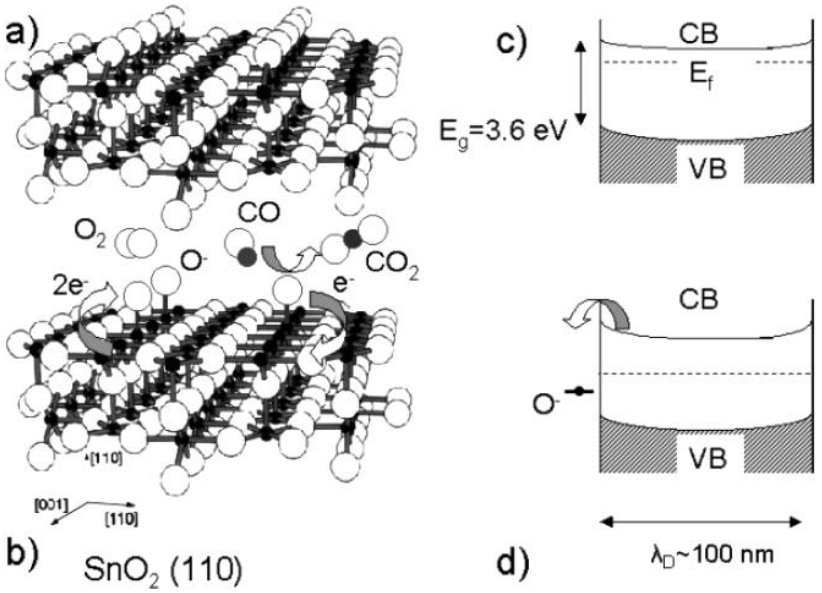

Figure 2.4: (*a*) Stoichiometric SnO_2 (110) surface, (*b*) partially reduced SnO_2 with missing bridging oxygens. Molecular oxygen binds to the vacancy sites as an electron acceptor. CO molecules react with pre-adsorbed oxygens, releasing electrons back to the nanowire. (*c*) Oxygen vacancies make SnO_2 into an *n*-type semiconductor. (*d*) When the Debye length is comparable to the radius of the nanowire, adsorption of electron acceptors shifts the position of the Fermi level away from the conduction band (from reference [14]) .

Essentially, all experiments carried out on metal-oxide nanowires (or other nanostructures) indicate that the role of oxygen vacancies dominates their electronic properties as they do in bulk systems. Each vacancy results in the formation of a filled (donor) intra-gap state lying just below the conduction band edge (Figure 2.4*c*). The energy interval between these states (or at least some of them) and the conduction band is small enough that a large fraction of the electrons in the donor states is ionized even at low temperatures, thus converting the material into an *n*-type semiconductor.

At a given temperature the conductance of the nanowire, $G = \pi R^2 e \mu n / L$, is determined by the equilibrium conditions determining the relative concentrations of ionized surface vacancy states, which determine the electron concentration in the bulk of the material.

The conductance of SnO_2 changes rapidly with gas adsorption as a result of a multi-step process wherein the first is the adsorption of a molecule (for example, with O_2, might dissociate into two surface oxygen ions after chemisorption) with a consequent molecule-to-SnO_2 charge transfer (or vice versa). With oxygen as the adsorbate, the afore-mentioned surface vacancies are partially repopulated, which results in ionized (ionosorbed) surface oxygen of the general form $O^{-\alpha}{}_{\beta S}$.

The resulting equilibrium surface oxygen coverage, θ, depends on the oxygen partial pressure and the system temperature through the temperature-dependent adsorption/desorption rate constants, $k_{ads/de}$, on the concentration of itinerant electrons n, and the concentration of unoccupied chemisorption (vacancy) sites N_s.

$$\beta / 2\ O_2^{gas} + \alpha\ e^- + N_s = \quad O^{-\alpha}_{\beta s}$$

$$k_{ads}\ \ N_s\ \ n\ \ p^{\beta/2}{}_{O2} = k_{des}\ \ \theta$$

(where α, β = {1,2} accounts for the charge and molecular or atomic nature of the chemisorbed oxygen [32]). In forming ionosorbed oxygen, electrons become localized on the adsorbate, creating a ~20-50 nm thick, electron-deficient surface layer corresponding approximately to the Debye length for SnO_2 (in the temperature range 300-500 K), which results in band bending in the surface region of bulk samples.

For 10-100 nm diameter nanowires, the charge depletion layer affects the entire nanowire resulting in a so-called *flat band conditions* wherein the relative position of the Fermi level shifts away from the conduction band edge not only at the surface but throughout the nanowire (Figure 2.4d). Ultimately, a new kinetic equilibrium among the free electrons and the neutral and ionized vacancies is established. Under these nearly flat band conditions at moderate temperatures and for electron momenta directed radially, electrons can reach the surface of the nanowire with essentially no interference from the low electrostatic barrier. As a result, the electrons become distributed homogeneously throughout the entire volume of the nanowire.

Accordingly, the charge conservation condition simplifies to

$$N_s \, \theta = R / 2 \, (n - n_m),$$

where n_m is the density of itinerant electrons remaining in the nanowire after exposure to the adsorbate. The accompanying electron depletion $\Delta n = 2 N_s \theta / R$ results in a significant drop in conductance:

$$\Delta G = \pi R^2 e\mu / L \cdot 2N_s \theta / R$$

and the corresponding depopulation of the shallow donor states results in an increase in activation energy [27].

Upon adsorbing a reducing gas such as CO, the following surface reaction takes place with the ionosorbed oxygen

$$\beta \, CO^{gas} + O^{-\alpha}{}_{\beta S} \rightarrow \beta \, CO^{gas}{}_2 + \alpha \, e^-$$

which results in the reformation of the adsorption defect sites and the re-donation of electrons to the SnO_2 (Figure 2.4b). It can be shown that under flat band conditions the increase in electron concentration, $\Delta n_{CO} \sim p^{\beta/\alpha+1}{}_{CO}$, and therefore in the conductivity of the nanowire, $\Delta G_{CO} \sim e \cdot \Delta n_{CO}(T) \cdot \mu(T)$, increases monotonically with CO partial pressure [32]. This was confirmed experimentally on nanowires assuming O^- (α, β = {1}) to be the dominant reactive surface species [27].

The foregoing simple mechanism is able to account for the operation of tin oxide nanowire sensors under ideal ambients consisting of dry oxygen and a combustible gas such as CO. In a real-world environment, a large array of other molecules (chief among them, water) complicates the picture. Surface hydroxyls and hydrocarbons can temporarily or permanently react with adsorption sites modifying or adding to the possible reaction pathways.

A consequence of being able to shift the position of the Fermi level of the oxide nanowire by applying an external field or by doping the nanowire is the possibility of controlling molecular adsorption onto its surface (resulting in

the oscillation of the adsorbate between an electron donor and acceptor). An interesting instance of this was reported [33] with In_2O_3 nanowires exposed to NH_3: for nanowires with a low density of oxygen vacancies (corresponding to a Fermi level lower in energy within the bandgap), the adsorbate behaved as an electron donor causing the resistivity of the nanowire to increase upon exposure to ammonia.

With a higher oxygen vacancy density (the Fermi level nearer to the lower edge of the conduction band) the NH_3 behaved as an acceptor, quenching the nanowire's conductance (Figure 2.5).

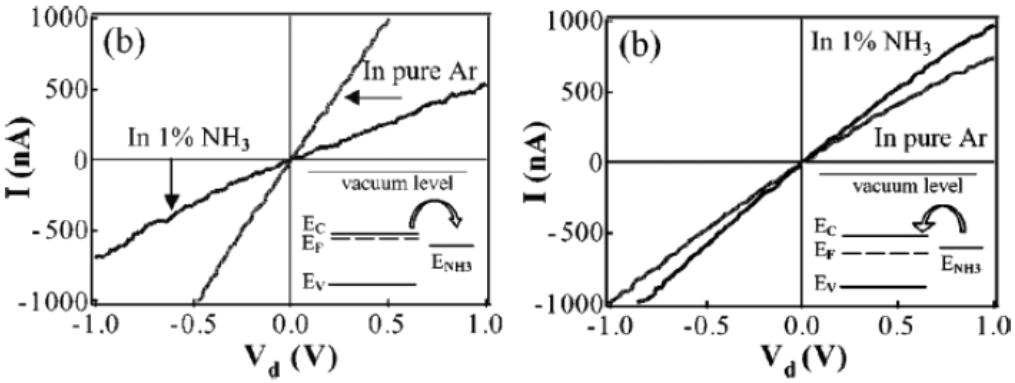

Figure 2.5: Alternating donor (*right plot*) versus acceptor (*left plot*) behaviour of NH_3 adsorbate as a function of the doping level of an In_2O_3 nanowire (from reference [33]).

2.2 ZnO nanowires growth: a novel mechanism discovered[†]

The controlled synthesis of quasi one-dimensional materials, such as nanowires and nanotubes, is nowadays one of the key research directions in nanotechnology. If these materials are to be useful in real applications (in electronics, biology and medical fields for example), full control of their

[†] The following part is based on L.C. Campos and M. Tonezzer, A.S. Ferlauto, L.O. Ladeira and R.G. Lacerda*, **"Epitaxially induced, low temperature growth of ZnO nanowires from solid Au-Zn catalyst"**, ***Advanced Materials***, 20, (2008),1499.

structure and properties is needed, and this can be achieved through precise control of their growth processes [34,35,36,37].

To obtain this, a clear picture of the growth kinetics is fundamental, especially for those nanomaterials which are grown via catalyst-assisted methods [38,39,40]. Nevertheless, in spite of significant advances in controlling the growth of nanowires, the various proposed growth mechanisms are still controversial and subject of strong debate [41,42]. In the 1960s, Wagner proposed a model to explain the growth of catalyst-assisted silicon whiskers based on a vapour-liquid-solid (VLS) mechanism [43].

This mechanism implies a growth temperature above the eutectic point of the seed catalyst particle and the nanowire material. The VLS model offers an adequate description for nanowire growth in simple classical systems, such as silicon (Si) and germanium (Ge) nanowires deposited at temperatures above the eutectic point [44,45].

Recently, the universal applicability of the VLS model has been questioned for the growth of hybrid III-V and II-VI nanowires (like, for example, GaAs, InP) and also for Ge and Si nanowires under certain growth conditions [38,39,41,46,47,48].

For these cases, a growth mechanism based on a vapour-solid-solid (VSS) regime has been proposed. In this framework, the various growth mechanisms of another important nanowire system (zinc oxide) are not comprehensively understood.

Zinc oxide has been demonstrated to be a quite complex and appealing material with a variety of different structures, such as nanowires, nanobelts, tetrapods, etc. Each of these structures can be formed by a different growth mechanism under a broad range of different thermodynamic conditions [36,37,49,50]. For instance, ZnO nanostructures have been grown directly (without a catalyst) from a solid source, such as a Zn foil [51], or using a ZnO film as a nucleation centre for the Zn atoms [52].

Those methods are usually described as being governed by a vapour-solid (VS) deposition process. Furthermore, Zinc oxide nanowires have also been grown by vapour deposition methods using metal nanoparticles (usually gold) as a catalyst at high [37,50] and low temperatures [53,54]. The VLS model

has been used to explain the growth mechanism at high temperatures, but a clear understanding of the growth process at low temperatures is still lacking.

The growth regime of ZnO nanowires is more difficult to understand under low temperature conditions due to the complexity of the Au-Zn phase diagram, if compared to that of the Au-Si or the Au-Ge systems phase diagrams, where only a small temperature range occurs in which the VLS mechanism is possible. In addition, intricate aspects of the growth mechanism, such as the nature of the catalyst particles during growth (solid or liquid) and the role of oxygen (including the oxidation process itself), necessary for the ZnO nanowire formation, still remain unclear.

The present section of this thesis will provide a basic theory for the mechanism of vapour-solid-solid (VSS) zinc oxide nanowires growth at low temperatures and will try to give the fundamental reasons responsible for such growth.

We will demonstrate, by using a combination of synchrotron X-ray diffraction (XRD) analysis and high-resolution transmission electron microscopy (HRTEM), that the growth dynamics at low temperatures are not governed by the well-known VLS mechanisms [36,37]. Based on the Au-Zn phase diagram, temperature measurements and temperature-size effects, we will show that growth occurs via a novel VSS mechanism. The precise composition of the Au-Zn catalyst nanoparticle was determined to be γ-AuZn.

Furthermore, we will observe experimentally that there is an indication of an epitaxial relationship between the ZnO nanowires and the γ-AuZn seed particle. A critical, new insight on the driving factor behind VSS growth will be presented, in which the VSS process occurs by a solid diffusion mechanism that is driven by preferential oxidation of the Zn inside the alloy catalyst induced by an epitaxial match between the ZnO(10-10) plane and the γ-AuZn(222) plane.

We believe that these results are not only important for the understanding of ZnO nanowire growth, but they may also have a significant impact on the understanding of growth mechanisms of other nanowire systems.

2.2.1 Nanowires growth

Zinc oxide nanowires were synthesized by the well-known chemical vapour deposition method [36,37]. More specifically, the Zn source was obtained by a carbo-thermal reaction [49,52]: a mixture of ZnO (99.99%) and graphite (99%) powders (1:1 weight ratio) was used and the substrates were Si (100) wafers covered with a thick (1 mm) oxide layer and a thin (~4 nm) Au layer. The ZnO/graphite mixture was placed in the centre of a quartz tube (22 mm diameter), and was maintained at 930 °C under constant Ar flow (400 sccm).

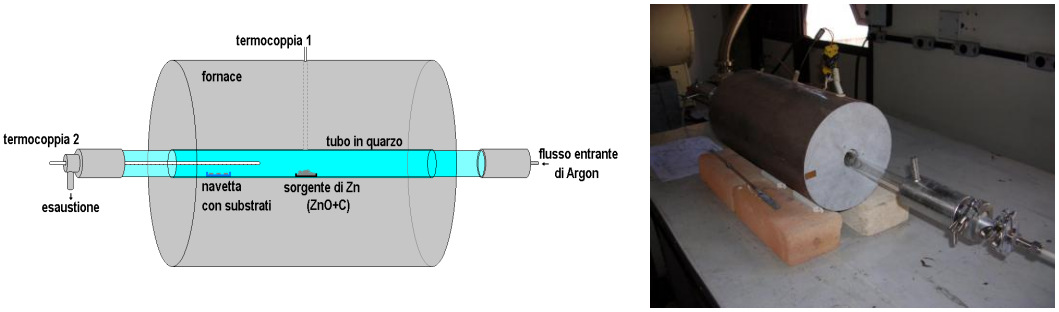

Figure 2.6: a) simple drawing showing the deposition system; b) picture of the real system used to grow the ZnO nanowires.

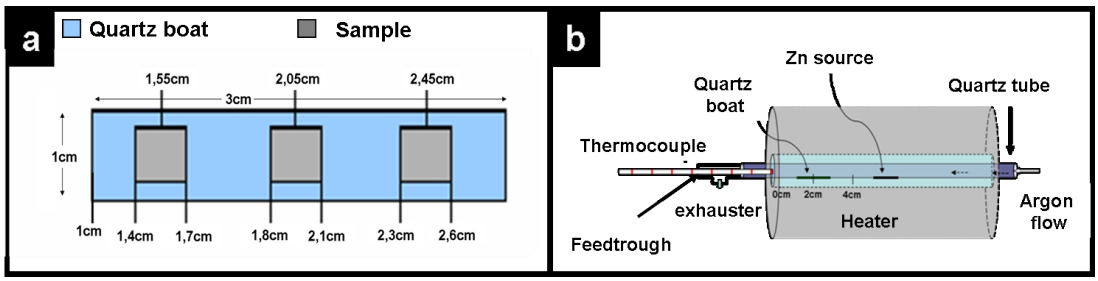

Figure 2.7: Diagram of the sample positions and temperature measurements inside the furnace. (a) The samples (silicon substrates) were placed on a quartz vessel in specific. The size of the Si substrates is also depicted in detail. (b) The temperature profile was obtained by setting up the CVD system in conditions exactly like those one performed during the

nanowire growth. A thermocouple inserted by a feedthrough was used to measure the temperature at each specific position. The feedthrough allows the change in position of the T_C in situ along the quartz tube. In other words, a temperature profile can be performed (with the Ar flux) in the exact growth conditions.

The substrates were positioned downstream in regions corresponding to temperatures ranging from 200 to 370 °C (Figure 2.8). The temperature calibration inside the tube was achieved by scanning a thermocouple along the length of the tube under flow and temperature equal to those of the growth conditions.

Typically, the temperature depends linearly on the position in the deposition region with a gradient of ~100 °C·cm^{-1}. Thus, for a typical sample the temperature difference between the edges is ~30 °C.

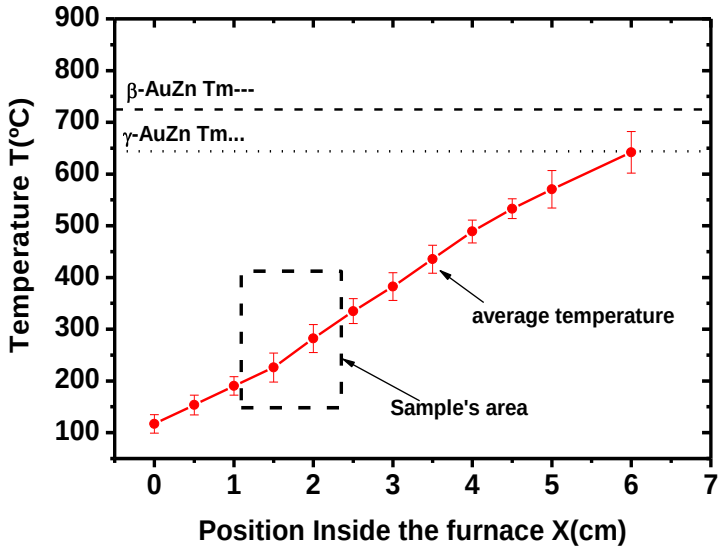

Figure 2.8: Temperature profile of the furnace. The position of the x axis corresponds to the distance from the left edge of the system. The horizontal lines (doted and dashed, respectively) are the melting temperatures of the γ-AuZn and β-AuZn alloys. The dotted square area is the representation

of the samples positions within the furnace (from 1.4 to 2.6 cm) which corresponds to a temperature range from 200 ^{o}C to 370 ^{o}C.

Scanning electron microscopy (SEM), transmission electron microscopy (TEM), and X-ray diffraction (XRD) analysis were used to characterize the morphological and structural properties of both the ZnO nanowires and the catalyst particles. The TEM was a JEOL 2010 equipped with a field-emission gun (FEG) emitter working at 200 keV and the spherical aberration corrector C_s = 0.5 mm.

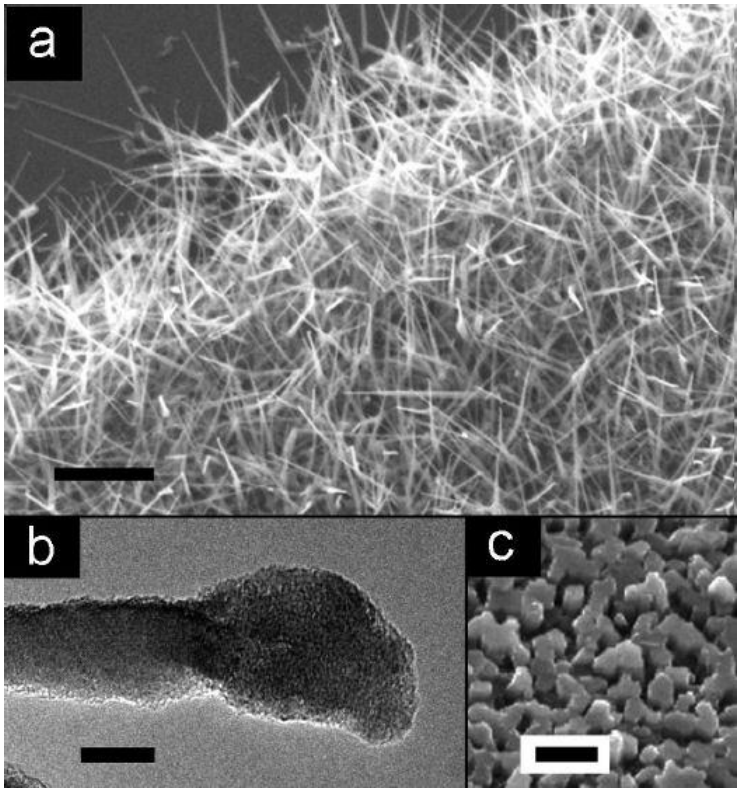

Figure 2.9: SEM and TEM images of materials formed at T = 350 °C. a) SEM image showing a high density of ZnO nanowires with nanowire diameters ranging from 20 to 100nm (scale bar: 1μm). b) TEM image of a typical catalytic particle. The irregular shape of the particle indicates that it was not liquid during the growth process (scale bar: 10 nm) c) SEM image of a polycrystalline ZnO film, which was formed when no thin gold film was used as catalyst (scale bar: 1 μm).

The XRD experiments were performed at the Brazilian National Synchrotron Laboratory using photons with λ = 0.15426 nm. Figure 2.9 shows typical SEM and TEM images of the ZnO nanowires obtained at T = 350 °C. Figure 2.9a demonstrates that a high density of nanowires was observed; the nanowires had a mean diameter of about 20 nm. Structures with similar morphologies were formed at temperatures as low as 300 °C, whereas at T>450 °C polycrystalline ZnO films were formed.

In order to determine the role of the gold catalyst in the formation of the ZnO nanowires, we performed deposition runs using Si/SiO_2 substrates without the Au layer. In this case, a polycrystalline ZnO film was formed instead of nanowires (Figure 2.9c). Figure 2.9b and Figure 2.10 show TEM images of typical catalytic particles.

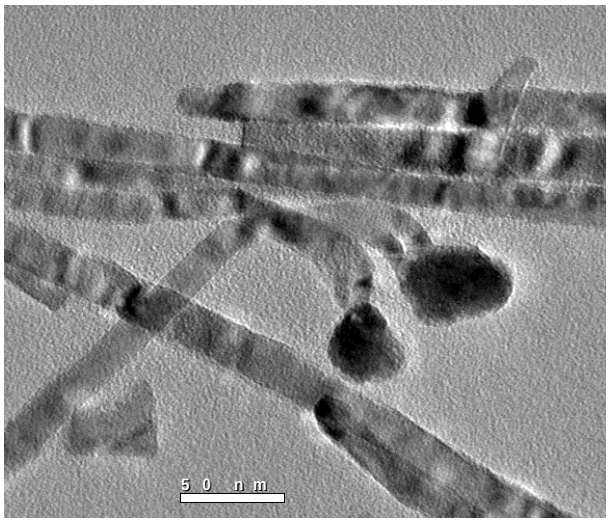

Figure 2.10: TEM pictures of the ZnO nanowires showing catalyst particles with irregular shape (see also Figure 2.9b).

Interestingly, the particle had an irregular shape rather than a rounded shape, which is normally observed in catalytically assisted nanowire growth via vapour-liquid-solid growth mechanism.

2.2.2 Nanowires characterization: XRD

Synchrotron X-ray diffraction analysis was performed to prove the crystalline structure of the ZnO nanowires and to investigate the nature of the catalyst particle at their tips. Figure 2.11 shows a typical XRD pattern for a sample grown at T = 350 °C. The majority of the peaks corresponds to the ZnO structure and their relative intensities are consistent with a reference powder diffraction pattern, which indicates that there is no preferential alignment of the zinc oxide wires.

There is also a broad peak (2θ= 47.88), which originates from the Si substrate (100). There is a clear peak at 2θ= 41.38 (corresponding to an interplanar spacing of 0.217 nm), which could not be assigned to ZnO or to Si. Thus, this peak has to originate from the catalyst particles. However, it does not match any of the possible reflections of the Au face-centred cubic (fcc) structure, nor of the zinc hexagonal close-packed (hcp) structure. In order to identify the origin of this peak, the diffraction patterns of several Au-Zn alloys were analyzed.

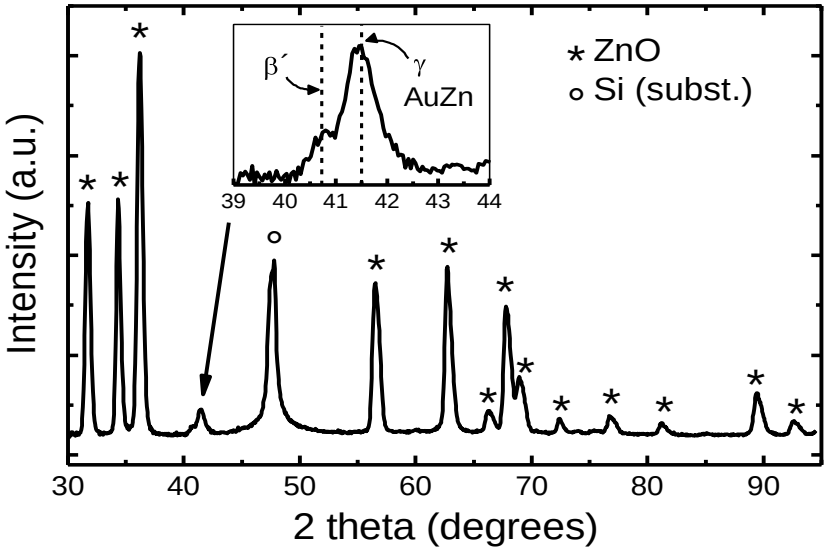

Figure 2.11: XRD pattern of the zinc oxide nanowires samples grown at T = 350 °C. All observed peaks correspond either to ZnO (*) or Si (o), except the peak at 2θ= 41.38 (shown in detail at the inset). This peak has been attributed to the (330) plane of the γ-brass Au-Zn alloy.

The inset of Figure 2.11 shows an enlarged view of the unknown catalyst peak. The magnification reveals that the peak is formed by two overlapping contributions: a major one centred at ~41.58, which has been attributed to the (330) and (411) reflections of the cubic gamma brass structure, γ-AuZn (lattice parameter, a= 0.922 nm) [55,56] and a smaller shoulder at ~40.88, which has been attributed to the (110) reflection of the base-centred cubic (bcc) beta structure, β'-AuZn (a = 0.314 nm) [57]. Both reflections were associated with the strongest lines in the corresponding powder diffraction patterns.

The structural identification of the catalyst particles has then been confirmed using HRTEM analysis of particles found at the nanowire tips, as can be seen in Figure 2.12.

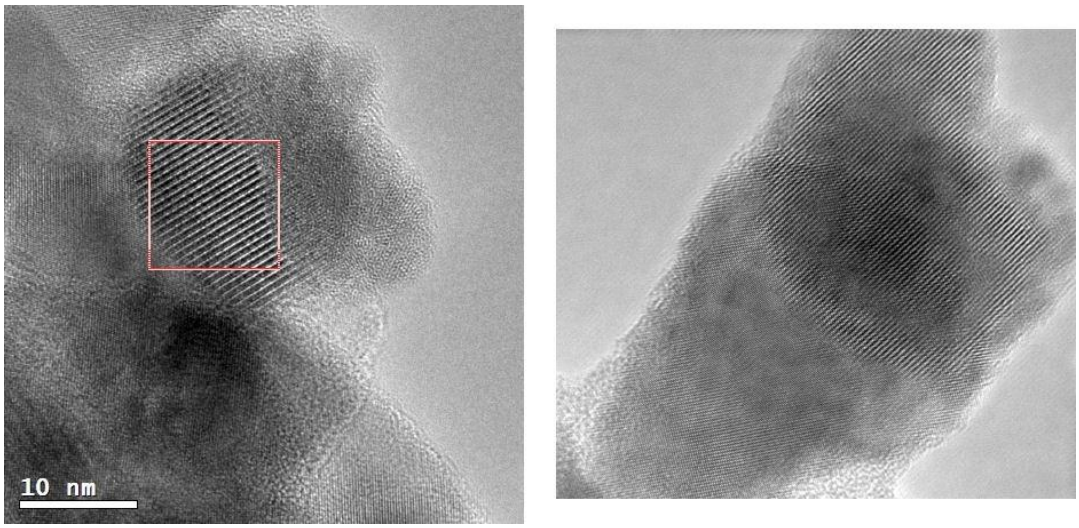

Figure 2.12: HRTEM pictures of typical catalyst particles. The observed lattice spacing in (a) and (b) can both be attributed to structure of the γ-AuZn alloy. (a) 0.65 nm corresponds to (110) and (b) 0.36 nm corresponds to (112).

Although there were several assignments possible for some of the observed periodicities found in the images, all the measured values of interplanar spacing could be attributed to the γ-AuZn phase (see Table 2.1).

Even though the results presented above relate to the post-synthesis state of the catalytic particles at room temperature, it is possible to make some inferences about their state during the deposition. Under atmospheric pressure and for T < 400 °C, the Au-Zn binary phase diagram indicates that an Au-Zn alloy will be in the solid state for all Zn concentrations (Figure 2.13).

Measured interplanar distance (nm)	**(hkl) in γ-AuZn**	**Calculated interplanar distance (nm)**
0.65	(110)	0.652
0.38	(211)	0.377
0.29	(310)	0.292
0.27-0.28	(311)	0.278
0.26-0.27	(222)	0.266

Table 2.1: Inter-planar spacing in the catalyst particles, determined from the HRTEM images such as the ones displayed in Figure 2.12. The corresponding spacings calculated by using a lattice parameter a=0.922 nm for the cubic γ-AuZn phase are given.

In particular, the congruent melting point (T_m) of the observed γ and β' phases is 644 °C and 725 °C, respectively, and the eutectic point between these two phases is 626 °C [58].

These values differ by more than 300 °C from the growth temperature. This observation implies that, under these growth conditions, those particles must be in a solid state during the ZnO nanowire growth.

Nevertheless, it is notorious that size effects can cause an important reduction of the T_m of the nanoparticles in comparison to that of the bulk values. In order to verify whether this effect would be significant in this case, the size dependence of the T_m of gold-zinc alloy particles has been calculated using the cohesive energy theory as reported by Qi.[59]

This model predicts successfully the melting temperature dependence of Sn and Pb particles with sizes ranging from 5-50 nm.

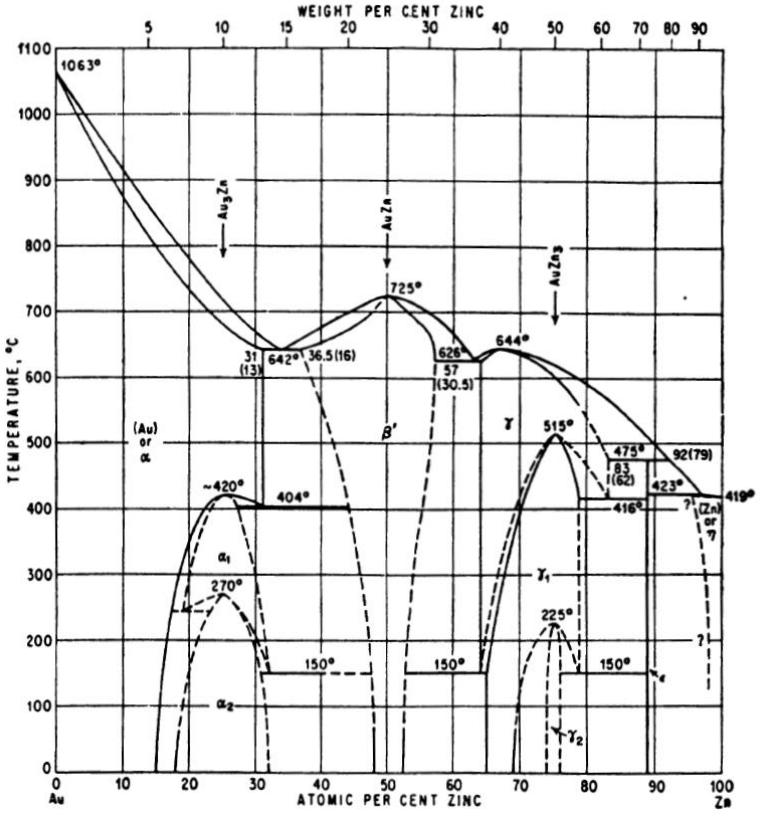

Figure 2.13: phase diagram of the Au-Zn binary system.

Figure 2.14 shows the calculated T_m as a function of the diameter of the catalyst particles for both the γ and β' phases. Significant decreases in T_m were only observed for particle diameters below 10 nm.

This excludes nanoscale effects on the phase diagram, and is a first strong clue about the catalyst particle state during the nanowire growth.

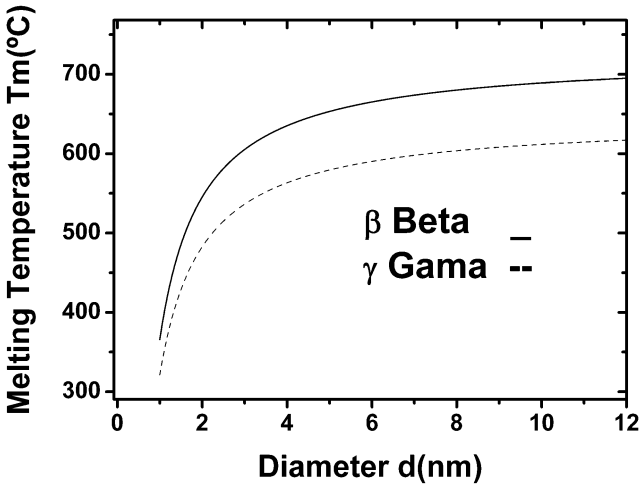

Figure 2.14: Dependence of the melting temperature (T_m) of the γ and β' phases on the diameter of the seed Au-Zn nanoparticles. Significant decreases in T_m were observed only for particle diameters below 10 nm for both materials.

2.2.3 Nanowires characterization: HRTEM

The HRTEM images of the AuZn nanoparticles showed a range of diameters between 20 and about 55 nm. The analysis presented in the previous section regarding the particle size and growth temperature demonstrates - in spite of not being able to perform this examination in situ - that the Au-Zn particles must have been in the solid state during the ZnO nanowires growth.

HRTEM analysis was performed on different ZnO nanowires. In all the cases where both nanowire and its nanoparticle were visible, it was possible to observe a correlation between the lattice fringes of the zinc oxide nanowire and the Au-Zn particle.

Figure 2.15 shows an example that illustrates clearly the epitaxial relationship between a ZnO nanowire and its Au-Zn particle.

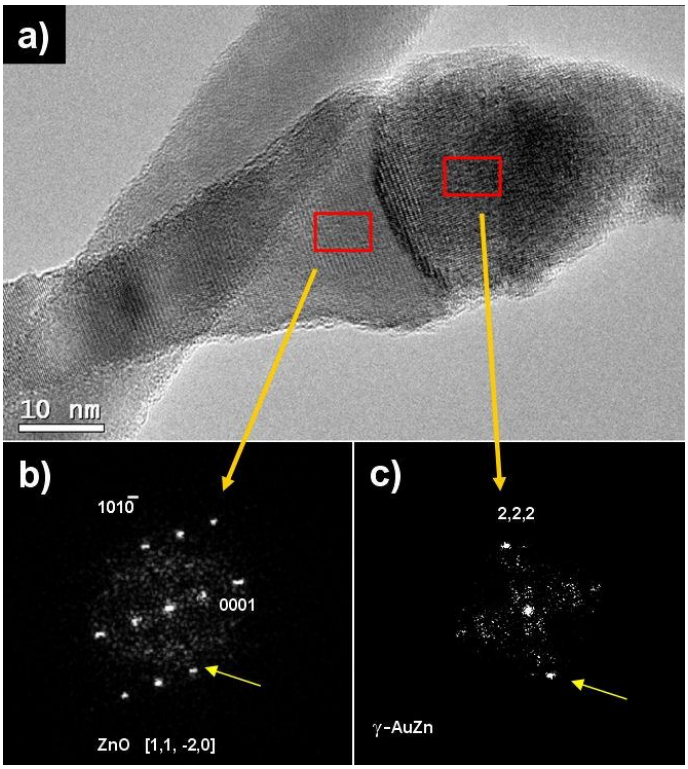

Figure 2.15. a) HRTEM image of the junction between ZnO nanowire and the γ-AuZn catalyst recorded along the ZnO[1,1,-2,0] zone axis. Images (b) and (c) show the FFT analysis of the ZnO nanowire and the γ-AuZn catalyst particle. The orientation relationship is evidenced by the coincidence of the two marked periodicities (see yellow arrows).

Selected regions of the HRTEM image shown in Figure 2.15a (orange rectangles) were Fourier-transformed and the results are shown in Figure 2.15b and c. The features observed in the fast Fourier transform (FFT) image of the nanowire region (Fig. 2.15b) could clearly be assigned to ZnO, corresponding to the (10-10) planes (d_{meas} = 0.28 nm, $d_{10\text{-}10}$=0.281 nm) and to the (0001) planes (d_{meas} = 0.52 nm, d_{0001}=0.521 nm). The latter plane corresponds to the growth direction, which is often observed for ZnO nanowires.

Likewise, the features observed in the FFT of the catalytic particle (Fig. 2.15c) can be assigned to the (222) planes (d_{meas} = 0.27 nm, $d_{2,2,2}$ = 0.266 nm) of the γ-AuZn phase. Most importantly, it is clear from the comparison of

the FFT images that the ZnO (10-10) planes have the same direction and almost the same spacing (6% strain) as the γ-AuZn (222).

Another indirect example that shows evidence of the epitaxial relationship between the ZnO nanowire and the Au-Zn particle can be seen in Figure 2.16. It must be stressed that in all cases where the crystalline structure of the nanowire and the AuZn particle were visible together, the epitaxial relationship could be found. These findings suggest that the ZnO nanowires were growing epitaxially from the solid catalytic particles [60].

The evidence presented above points out that catalytic Au-Zn particles remain solid during the growth of the ZnO nanowires. This discovery is in agreement with recent publications, which report that the catalytic particle is in the solid phase during the growth process for many different nanowire/ catalyst systems; examples include GaAs/Au [47], $Si/TiSi_2$ [46], and Ge/GeNi [48].

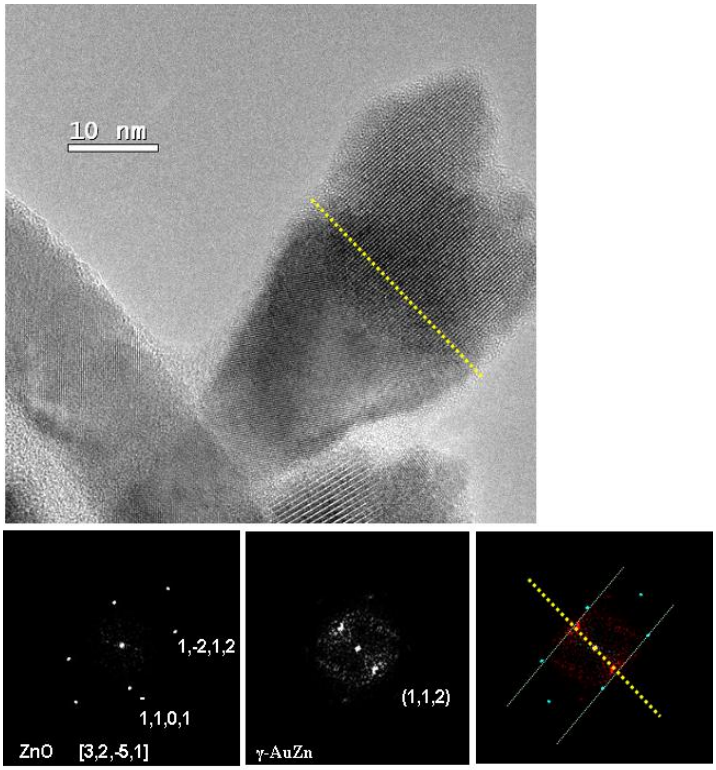

Figure 2.16: (a) HRTEM of the ZnO nanowire (the column was aligned in the direction [3,2,-5,1] of the ZnO). In this configuration, it is possible to observe simultaneously planes of the ZnO nanowire and planes of the particle. (b), (c) and (d) FFT performed showing that the projection of the ZnO

periodicities on the interface line (the yellow line) is approximately the same as the (1,1,2) periodicity of the γ-AuZn.

Moreover, recent observations have also indicated that chemical vapour deposition of carbon nanotubes also occurs via solid catalyst particles [61,62]. Therefore, we can say that the presence of a catalyst particle in the liquid phase is not a necessary condition for a catalyst-assisted 1D growth.

In the vapour-liquid-solid theory, the preferential incorporation of reactant species at the catalyst particle is a critical step to ensure anisotropic growth and a liquid particle provides an ideal ‘‘rough surface’’ to maximize such incorporation [43,63]. The VLS theory has been particularly successful in describing the growth of elemental semiconductors, such as Si and Ge, deposited at higher temperatures, but it seems to fail in describing growth processes for compound materials such as the III-V and II-VI semiconductors families and oxides [38,46,47,48].

On the other hand, since the pioneering works of Sears et al. [64], vapour-solid (VS) processes have been invoked to describe the formation of whiskers (1D nanostructures) and other anisotropic structures [63,65]. Vapour-solid processes are also believed to be effective to induce anisotropic growth for crystals that have low-index facets with large differences in the surface energy, such as ZnS and ZnO [66,67].

ZnO has a wurtzite structure with two non-polar surfaces, (10-10) and (11-20), and one polar surface, (0001). The latter has a surface energy that is roughly twice the value of the energy of the non-polar surfaces and thus corresponds to the fast growth direction. This explains the preferential growth of ZnO thin films and 1D nanostructures in the [0001] direction. However, it seems that pure VS mechanisms can only account for ZnO nanowires growth at supersaturated conditions, close to the onset of homogeneous nucleation of the ZnO crystals.[67]

Conversely, the formation of ZnO nanowires on substrates is usually facilitated by the presence of catalyst particles, such as Zn (self-catalyzed), Au, or other metals.[36,37] In the present experiments, one can understand the

low-temperature growth of ZnO nanowires from solid Au-Zn catalysts as being an intermediate between the VLS and VS processes.

The presence of solid Au-Zn catalyst particles on the Si/SiO_2 substrates is particularly significant in the initial growth stages in order to supply nucleation sites for the Zn vapour. Assuming that at the beginning of the growth the Si/SiO_2 substrate is covered with Au islands, such islands will be the preferential sites for Zn incorporation, since the SiO_2 surface has a relatively lower reactivity. Corroboration of the occurrence of this mechanism is given by the fact that continuous ZnO films are formed when the Au layer is missing (see insert Figure 2.9c).

Consequently, the zinc atoms can either condense directly from the vapour phase or be transported via surface diffusion from the adjacent regions of the substrate [68,69]. Then, they can rapidly diffuse into the Au clusters, forming Au-Zn clusters, as described by Yasuda et al. [70]. In this incubation period, the Zn concentration in the particles increases with time, but the particles remain solid.

At a certain zinc concentration threshold, the nanowires begin to form and consequently the catalyst acts as a sink for Zn atoms, which generates a Zn concentration gradient along the catalyst particle. Upon further Zn incorporation at the opposite end of the particle, the growth can proceed continuously. Diffusion of Zn through the bulk solid Au-Zn particle and/or via its surface will therefore set an upper limit for the nanowire growth rate.

An estimation of this limiting value for bulk diffusion can be made by assuming a simple 1D model, whereby Zn atoms have to travel approximately 30nm between the Zn source and the particle/nanowire interface; all Zn atoms arriving at this interface are readily oxidized to form the nanowire. Because values for Zn diffusion in Au-Zn alloys are unknown, diffusion values of Zn in bulk Au and of Zn in Zn (self-diffusion) were considered.

Growth rate values, calculated using the Zn self-diffusion coefficient obtained from the work of Persson et al. [69], were 28 and 448 nm/s for T = 316 and 418 °C, respectively. Similar calculations for Zn diffusion in bulk gold provided growth rate values of 0.62 and 2.0 nm/s for T = 300 and 400 °C, respectively [70]. The average growth rate measured from the analysis of SEM images of the deposited nanowires was about 0.7 nm/s.

This value was much lower than the limiting values corresponding to Zn self-diffusion and of the same order as those obtained for Zn diffusion in Au. For this latter comparison, it is worth mentioning that Zn diffusion in small Au particles (<10 nm) has been found to be up to 10 orders of magnitude larger than Zn diffusion in bulk gold [70].

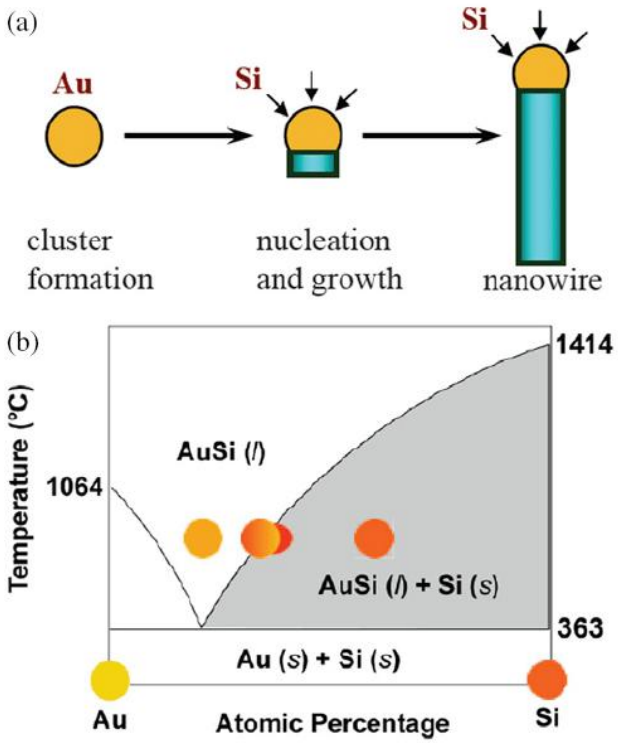

Figure 2.17: the simple phase diagram of Au-Si binary system. The catalyst nanoparticle, moving from left to right, increases it's Si percentage and at the "eutectic valley" right border starts to eject solid silicon which combines in a crystalline lattice, giving rise to the Si nanowire.

The above analysis demonstrates that a growth dynamic in which Zn diffuses through a solid Au-Zn catalyst particle offers a plausible explanation for the formation of ZnO nanowires at low temperatures.

Another open question is how the ZnO nanowires precipitate from the Au-Zn particle and why this happens only with particles having a narrow range of Zn concentrations (γ-AuZn phase, ~70 wt% Zn)? In order to make this clear,

we consider the conventional VLS mechanism in the Si/Au system. The solubility range of Si in the Au-Si liquid alloy is quite narrow due to the large eutectic melting point depression (Figure 2.17).

Therefore, upon Si incorporation, the liquid alloy readily becomes supersaturated and the Si nanowire is formed from precipitation. ZnO nanowire growth, on the other hand, cannot follow this simple picture. The Au-Zn binary phase diagram is much more complex than the Au-Si or Ge-Si diagrams and there is only a narrow temperature range (from ~640 to 725 °C) in which a mechanism similar to the Si/Au system could be activated (Figure 2.13).

Thus, for high temperatures (T>725 °C), an Au-Zn catalyst particle may become liquid, if the Zn concentration reaches a certain value. However, no Zn precipitation is expected to occur even if the Zn concentration becomes even higher (i.e., there is no solubility limit for Zn in the Au-Zn liquid alloy). In the low-temperature case (T<640 °C), upon Zn incorporation, the Au-Zn alloy will transform into phases with increasing Zn concentrations, where Zn precipitation can only take place at very large Zn concentrations (>90 at%).

In our case, ZnO nanowire growth occurred with solid AuZn nanoparticles in the γ-AuZn and β'-AuZn phases. Therefore, there must be another mechanism to promote the precipitation of ZnO nanowires from the Au-Zn particles only at these particular phases.

In this scenario, it is essential to consider that the oxidation process is a crucial step in ZnO nanowire formation. Wang and co-workers [71] have shown that the oxygen partial pressure strongly influences the growth yield and morphology of ZnO nanowires. However, they assert that the experimental effects are a consequence of changes in the carbo-thermal reactions responsible for the Zn vapour supply. Alternatively, Heo et al. have proposed that ZnO nanowire formation can take place via the oxidation of zinc through a reaction with Ag_2O inside Ag islands [72].

However, until these experiments, details of zinc oxidation reactions resulting in nanowire growth had never been presented. In the present case, it is likely that ZnO nanowires originate from the oxidation of Zn atoms within the solid Au-Zn alloy particle, since it is commonly known that the activity of

metals can be increased upon alloying. Moreover, it has also been observed that the internal oxidation of alloys, such as Zn-Ag and Zn-Cu, results in the formation of ZnO crystalline precipitates, which present preferential orientation relations with respect to the crystals of the remaining matrix metal [73].

In a similar manner, it can be expected that, during the growth process, the oxidation of Au-Zn particles will generate ZnO precipitates (i.e. the nanowires) having a fixed orientation with respect to the crystallographic particle orientation. In this sense, ZnO nanowire formation will occur preferentially at the (1,1,-2) or (1,-1,0) surfaces of the γ-AuZn particles, as observed experimentally. According to Figure 2.15b and c, the (1,1,-2) or (1,-1,0) surfaces are two possible low-index surfaces that could form an interface with the ZnO nanowire.

Such a preferential oxidation mechanism might explain why most of the observed catalyst particles consist of the γ-AuZn phase, since this phase provides a suitable surface wherefrom ZnO nanowires can grow in an epitaxial-like manner, whereby the ZnO(10-10) planes match the γ-AuZn(222) planes. Although calculations of the thermodynamics and kinetics of such oxidation mechanisms are beyond the scope of this work, it is reasonable to assume that the presence of a low-energy epitaxial interface between the solid catalyst particle and the nanowire will favour nanowire growth.

[1] W. Göpel, J. Hesse, J.N. Zemel, *Sensors: A Comprehensive Survey,* pp. 1-7. New York: VCH (1995)

[2] P.T. Moseley, B.C. Tofield, eds. 1987. *Solid-State Gas Sensors*. Bristol/Philadelphia: Hilger

[3] Sberveglieri G, *Gas Sensors:Principles, Operation and Developments.* Boston: Kluwer 1992.

[4] A. Mandelis, C. Christofides, *Physics,Chemistry and Technology of Solid StateGas SensorDevices.* New York: Wiley-Interscience (1993).

[5] W. Göpel, *Sensors Actuators B 21 (*1991) 4-7.

[6] W. Göpel, *Sensors Actuators A 102 (*1996) 56-83.

[7] C. Hagleitner, A. Hierlemann, D. Lange, A. Kummer, N. Kerness et al., *Nature* 96 *(*2001.) 414.

[8] S. Semancik, R.E. Cavicchi, M.C. Wheeler, J.E. Tiffany, G.E. Poirier et al., *Sensors Actuators B* 77 (2001) 579.

[9] W. Göpel, *Microelect. Eng.* 32 (1996) 75.

[10] K.J. Albert, N.S. Lewis, C.L. Schauer, G.A. Sotzing, S.E. Stitzel et al., *Chem. Rev.* 100 (2000) 2595.

[11] T.C. Pearce, S.S. Schiffman, H.T. Nagle, J.W. Gardner eds., *Handbook of Machine Olfaction: Electronic Nose Technology.* Weinheim: Wiley-VCH (2003).

[12] P.T. Moseley, *Sensors Actuators B* 6 (1992) 149.

[13] N.M. White, J.D. Turner, *Meas. Sci. Technol.* 8 (1997) 1.

[14] D. Kohl, *J. Phys. D* 34 (2001) R125.

[15] V.E. Henrich, P.A. Cox, *Surface Science of Metal Oxides*. Cambridge/New York: Cambridge (1996).

[16] Y.N. Xia, P.D. Yang, Y.G. Sun, Y.Y Wu, B. Mayers et al., *Adv. Mater.* 15 (2003) 353.

[17] Z.L. Wang, *Nanowires and Nanobelts: Materials, Properties and Devices.* Dordrecht/ London/New York: Kluwer (2003).

[18] S. Bandyopadhyay, H.S. Nalwa eds., *Quantum Dots and Nanowires.* Stevenson Ranch, CA: American Scientific (2002).

[19] Z.R. Dai, Z.W. Pan, Z.L. Wang, *Adv. Funct. Mater.* 13 (2003) 9.

[20] C. Li, D.H. Zhang, X.L. Liu, S. Han, T. Tang et al., *Appl. Phys. Lett.* 82 (2003) 1613.

[21] W.I. Park , G.C. Yi , M. Kim, S.J. Pennycook, *Adv. Mater.* 15 (2003) 526.

[22] M. Law, H. Kind, B. Messer, F. Kim, P.D. Yang, *Angew. Chem. Int. Ed.* 41 (2002) 2405.

[23] Z.W. Pan, Z.R. Dai, Z.L. Wang, *Science* 291 (2001) 1947.

[24] E. Comini, G. Faglia, G. Sberveglieri, Z.W. Pan, Z.L. Wang, *Appl.Phys. Lett.* 81 (2002) 1869.

[25] M.S. Arnold, P. Avouris, Z.W. Pan, Z.L. Wang, *J. Phys. Chem. B* 107 (2003) 659.

[26] A. Kolmakov, Y. Zhang, M. Moskovits, *Nano Lett.* 3 (2003) 1125.

[27] A. Kolmakov, Y. Zhang, G. Cheng, M. Moskovits, *Adv. Mater.* 15 (2003) 997.

[28] J.N. Zemel, *Thin Solid Films* 163 (1988) 189.

[29] W. Göpel, *Sens. Actuators* 16 (1989) 167.

[30] D. Kohl, *Sens. Actuators* 18 (1989) 71.

[31] N. Barsan, R. Grigorovici, R. Ionescu, M. Motronea, A. Vancu, *Thin Solid Films* 171 (1989) 53.

[32] N. Barsan, U. Weimar, *J. Electroceram.* 7 (2001) 143.

[33] D.J. Zhang, C. Li, X.L Liu, S. Han, T. Tang, C.W. Zhou, *Appl. Phys. Lett.* 83 (2003) 1845.

[34] C. M. Lieber, Z. L. Wang, MRS Bull. 32 (2007) 99.

[35] C. Thelander, P. Agarwal, S. Brongersma, J. Eymery, L.F. Feiner, A. Forchel, M. Scheffler, W. Riess, B.J. Ohlssoni, U.Go¨ selej, L. Samuelson, *Mater. Today* 9 (2006) 28.

[36] M. H. Huang,Y.Y.Wu, H. Feick, N. Tran, E. Weber, P. D.Yang, *Adv. Mater.* 13 (2001) 113.

[37] P. Yang, H. Yan, S. Mao, R. Russo, J. Johnson, R. Saykally, N. Morris, J. Pham, R. He, H.-J. Choi, *Adv. Funct. Mater.* 12 (2002) 323.

[38] K.A. Dick, K. Deppert, T. Martensson, B. Mandl, L. Samuelson, W. Seifert, *Nano Lett.* 5 (2005) 761.

[39] Y. Wang, V. Schmidt, S. Senz, U. Goesele, *Nat. Nanotech.* 1 (2006) 186.

[40] J. C. Harmand, G. Patriarche, N. Péré-Laperne, M.-N.Mérat-Combes, L. Travers, F. Glas, *Appl. Phys. Lett.* 87 (2005) 203101.

[41] S. Kodambaka, J. Tersoff, M. C. Reuter, F.M. Ross, *Science* 316 (2007) 729.

[42] V. Schmidt, U. Gosele, *Science* 316 (2007) 698.

[43] R.S. Wagner, W.C. Ellis, *Appl. Phys. Lett.* 4 (1964) 89.

[44] A.M. Morales, C.M. Lieber, *Science* 208 (1998) 279.

[45] W. Lu, C. M. Lieber, *J. Phys. D: Appl. Phys.* 39 (2006) R387.

[46] T.I. Kamins, R.S. Williams, D.P. Basile, T. Hesjedal, J.S. Harris, *J. Appl. Phys.* 89 (2001) 1008.

[47] A.I. Persson, M.W. Larsson, S. Stenstrom, B.J. Ohlsson, L. Samuelson, L.R. Wallenberg, *Nat. Mater.* 3 (2004) 677.

[48] H.Y. Tuan, D.C. Lee, T. Hanrath, B.A. Korgel, *Chem. Mater.* 17 (2005) 5705.

[49] X.D. Wang, J.H. Song, Z.L. Wang, *J. Mater. Chem.* 17 (2007) 711.

[50] H.J. Fan, W. Lee, R. Hauschild, M. Alexe, G. Le Rhun, R. Scholz, A. Dadgar, K. Nielsch, H. Kalt, A. Krost, M. Zacharias, U. Gosele, *Small* 2 (2006) 561.

[51] X. Wen, Y. Fang, Q. Pang, C. Yang, J. Wang, W. Ge, K. S. Wong, S. Yang, *J. Phys. Chem. B* 109 (2005) 15303.

[52] J. Wang, J. Sha, Q. Yang, X. Ma, H. Zhang, J. Yu, D. Yang, *Mater. Lett.* 59 (2005) 2710.

[53] X. Wang, Q. Li, Z. Liu, J. Zhang, Z. Liu, R. Wang, *Appl. Phys. Lett.* 84 (2004) 4941.

[54] J.-J. Wu, S.-C. Liu, *Adv. Mat.* 14 (2002) 215.

[55] A.J. Bradley, J. Thewlis, *Proc. R. Soc. London A* 12 (1926) 678.

[56] L.K. Brandon, R.Y. Brizard, P.C. Chieh, R.K. Mcmillan, W.B. Pearson, *Acta Crystallogr. B* 30 (1974) 1412.

[57] H. Ipser, A. Mikula, P. Terzieff, *Monatshefte für Chemie* 114 (1983) 1177.

[58] M.G. William, in *The Handbook of Binary Phase Diagrams* (Ed: W. G. Moffatt), General Electric Corporation, Schenectady NY (1981).

[59] Q.H. Qi, *Physica B* 368 (2005) 46.

[60] R. Buonsanti, V. Grillo, E. Carlino, C. Giannini, M.L. Curri, C. Innocenti, C. Sangregorio, K. Achterhold, F.G. Parak, A. Agostiano, P.D. Cozzoli, *J. Am. Chem. Soc.* 128 (2006) 16953.

[61] S. Helveg, C. Lopez-Cartes, J. Sehested, P.L. Hansen, B.S. Clausen, J.R. Rostrup-Nielsen, F. Abild-Pedersen, J.K. Norskov, *Nature* 427 (2004) 426.

[62] S. Hofmann, G. Csanyi, A.C. Ferrari, M.C. Payne, J. Robertson, *Phys. Rev. Lett.* 95 (2005) 036101.

[63] E.I. Givargizov, *Highly Anisotropic Crystals*, D. Reidel Publishing Company, Dordrecht, The Netherlands (1987).

[64] G.W. Sears, *Acta Met.* 1 (1953) 457.

[65] K.A. Jackson, S.M. Arnold, *J. Appl. Phys.* 35 (1964) 2993.

[66] A. Colli, S. Hofmann, A.C. Ferrari, C. Ducati, F. Martelli, S. Rubini, S. Cabrini, A. Franciosi, J. Robertson, *Appl. Phys. Lett.* 86 (2005) 153103.

[67] Z.R. Dai, Z.W. Pan, Z.L. Wang, *Adv. Funct. Mater.* 13 (2003) 9.

[68] L.E. Jensen, M.T. Bjork, M.T, S. Jeppesen, A.I. Persson, B.J. Ohlsson, L. Samuelson, *Nano Lett.* 4 (2004) 1961.

[69] A.I. Persson, L. E. Froberg, S. Jeppesen, M. T. Bjork, L. Samuelson, J. Appl. Phys. 101 (2007) 034313.

[70] H. Yasuda, H. Mori, *Phys. Rev. Lett.* 69 (1992) 3747.

[71] J.H. Song, X.D. Wang, E. Riedo, Z.L. Wang, *J. Phys. Chem.* B 109 (2005) 9869.

[72] Y.W. Heo, D.P. Norton, L.C. Tien, Y. Kwon, B.S. Kang, F. Ren, S.J. Pearton, J.R. LaRoche, *Mater. Sci. Eng. R* 47 (2004) 1.

[73] W.P. Vellinga, J.T.M. DeHosson, *Acta Mater.* 45 (1997) 933.

Chapter 3

Tin oxide single-nanowire sensors‡

During the last decades many fields, from industrial processes control to safety systems, from disease diagnostics to environmental monitoring, strongly increased their demand for highly sensitive gas sensing devices. Metal-oxide based gas sensors, whose response rely on the change of their electrical resistance upon the interaction with the target gas [1], have been widely studied and commercialized.

Tin oxide (SnO_2) is one of the most important and widely used metal-oxide semiconductors used in gas sensors [2] mainly due to its sensitivity towards different gaseous species [3]. A first improvement in metal-oxide gas sensors has been reached with the use of thin films [4,5].

Miniaturization of the sensing device leads indeed to many advantages, mainly lower power consumption and intrinsic higher response. Recently, several different nanostructures have been produced and could be an effective sensor fundamental building block: nanowires [6], nanorods [7], nanobelts [8], nanosprings [9], nanosheets [10], nanospheres [11]…

The use of nanostructured materials is useful mainly for its huge surface-to-volume ratio, which leads to improved gas response. A resistive metal-oxide sensor uses indeed surface chemical reactions and the subsequent change of its conductivity (change in the density of conduction band electrons or valence band holes). The use of single nanowire (NW) devices allows to investigate their gas sensing properties without any average effect on different nanowires. The use of monocrystalline nanostructures also avoids the potential effect of grain boundaries, permitting to focus on the properties of the nanostructure under investigation.

‡ This chapter is based on M. Tonezzer*, N.V.Hieu, **"Size-dependent response of single-nanowire gas sensors",** accepted by ***Sensors and Actuators B: Chemical.***

Because of their tiny diameter, comparable to the Debye length, monocrystalline nanowires' electronic properties are strongly influenced by the processes that take place at their surface.

This means that a smaller diameter leads to higher gas response. Even though the space charge model has been confirmed in many works [12,13], there are still few reports on the diameter-dependence of nanowires gas response [14]. In the present work we show how the single-nanowire gas sensors performance behave as a function of the nanowires diameter. The increase of the gas response as a function of the NW diameter decrease, demonstrates that the potential of metal oxide nanostructures has not been exploited yet.

3.1 Materials and methods

Tin oxide (SnO_2) nanowires were grown by chemical vapour deposition in a horizontal quartz tube inside a horizontal furnace (Lingdberg Blue M). Pure tin powder was put in an alumina boat at the centre of the furnace, as evaporation source. The substrate, consisting in a piece of silicon wafer deposited by sputtering with a thin film (2-5 nm) of gold acting as catalyst, was put at each end of the alumina boat (around 1 cm from it).

The CVD system was then pumped to low vacuum (10^{-2} mbar) by a rotary pump, and then purged with high purity argon (99.999%). These two steps were repeated at least three times, and then the system was let pumping to its limit pressure. Then the furnace was switched on, increasing the temperature from 25°C to 800°C in 30 minutes.

After 5 minutes at 800°C (in order for the temperature to stabilize), the oxygen mass-flow controller was opened, introducing 0.35 standard cubic centimetres (sccm) oxygen gas into the system. The growth time was 30 minutes, after which the system was switched off, and let cool down naturally. When the temperature was lower than 200°C, the vacuum pump was switched off and the system could be vented.

The samples were presenting a white thick soft film (75 μm, measured by cross-sectional SEM), which is a homogeneous SnO_2 nanowires forest. As-grown SnO_2 nanowires were characterized by X-ray diffraction using a Philips Xpert Pro operated with a CuKα radiation generated at 40kV. The transmission electron microscopy (TEM) characterization was made by using a JEM-100CX operated at 90 kV, while the field-emission secondary electron microscopy (FE-SEM) images were taken by a Hitachi S-4800.

As dimethylformamide (DMF) has been found to be the best solvent for metal oxide nanowires dispersion [15], the as-grown nanowires were then dispersed in DMF by sonicating the sample for few seconds. The nanowires dispersion was then spin-coated onto a Si/SiO_2 wafer at 6000 rounds per minute, obtaining the best single-nanowire density. Standard UV lithography and RF sputtering were then used to deposit an array of Ti/Au (10 nm / 200 nm) electrodes over the dispersed nanowires, in order to contact them.

Once found by optical microscopy and resistance measurement, the single nanowires (SNW) devices, consisting in single nanowires bridging two metal electrodes, were investigated by SEM imaging. By SEM investigation, five different nanowires were chosen with different size, in order to characterize their properties as a function of their diameter. The SNW gas sensors performances were then measured in a home-built apparatus consisting in a test chamber with a heatable sensor holder, gas mass-flow controllers, a Keithely 2410 multimeter and a data acquisition system (LabView, National Instruments).

Initially, the I-V characteristics were studied within ±10V range, finding that the titanium/platinum electrical contacts show a good ohmic behavior. In order to improve the repeatability, the devices were conditioned at 300 °C at 1V in N_2 for 3 hours prior the measurements to stabilize their nanostructure and guarantee that their electrical properties would not change during gas tests [16]. The resistance of the sensors was in the range of 2 – 10 MΩ range under nitrogen exposure. The sensors were operated by applying a constant (1V) voltage between the Ti/Pt contacts and were tested for different NO_2 concentrations, in the temperature range of 50 - 400 °C.

The working temperature of the sensors was controlled by a feedback on the thermocouple of the sensor holder. The NO_2 concentration (50 -1000 ppm) was controlled by changing the mixing ratio of dry parent gases (x% NO_2) and dry synthetic N_2. A flow-through technique with a constant flow rate of 200 sccm was used. By monitoring the output current across the sensor, the resistances of the sensor in nitrogen or in NO_2 could be measured, and their ratio gives the gas response.

3.2 Nanowires Characterization

Figure 3.1 shows the XRD pattern of the as-grown tin oxide nanowires forest on the sample just after the chemical vapour deposition process. All the diffraction peaks in the spectrum match the cassiterite (tetragonal rutile) SnO_2 profile (a = 4.738 Å and c = 3.187 Å) as can be found in JCPDS 77-0450 card.

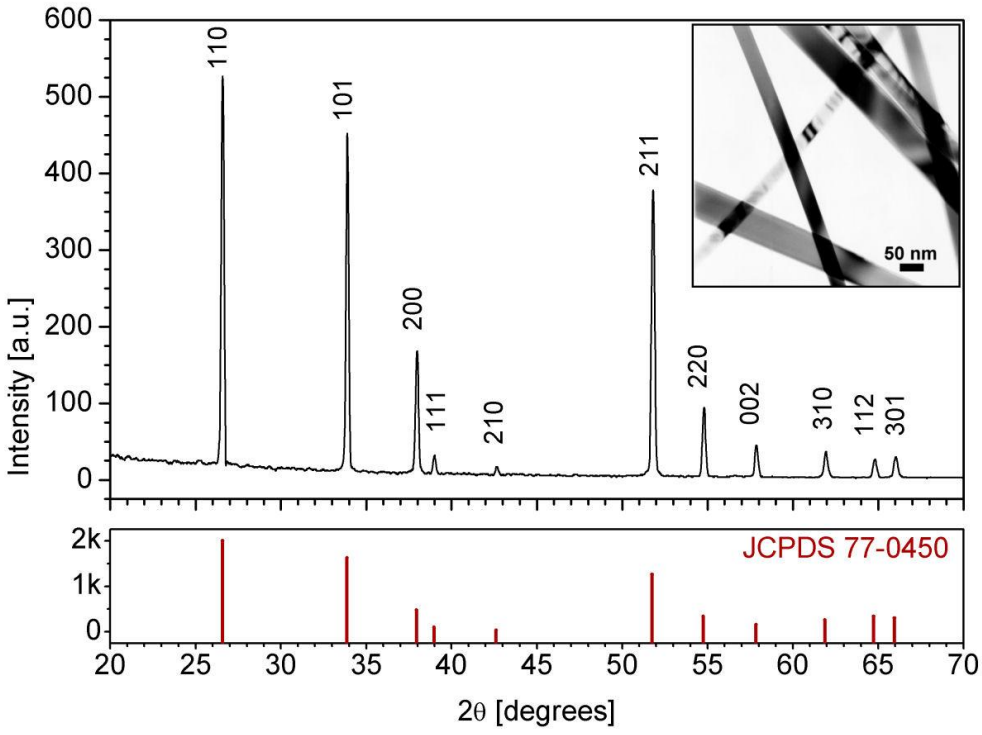

Figure 3.1: XRD pattern of as-grown SnO_2 nanowires. The bottom graph (in red online) shows the reference card. The inset shows a TEM image of the nanowires.

The inset shows a TEM image, confirming the size and structure of the nanowires. Figure 3.2 shows a SEM picture of the same SnO_2 nanowires forest, showing its uniformity and the NWs' size homogeneity.

The inset in Figure 3.2 shows the nanowires diameter distribution, calculated on several SEM pictures, taken in randomly chosen spots on the sample. The Gaussian fitting function is centred in 90 nm and has a sigma of 17 nm.

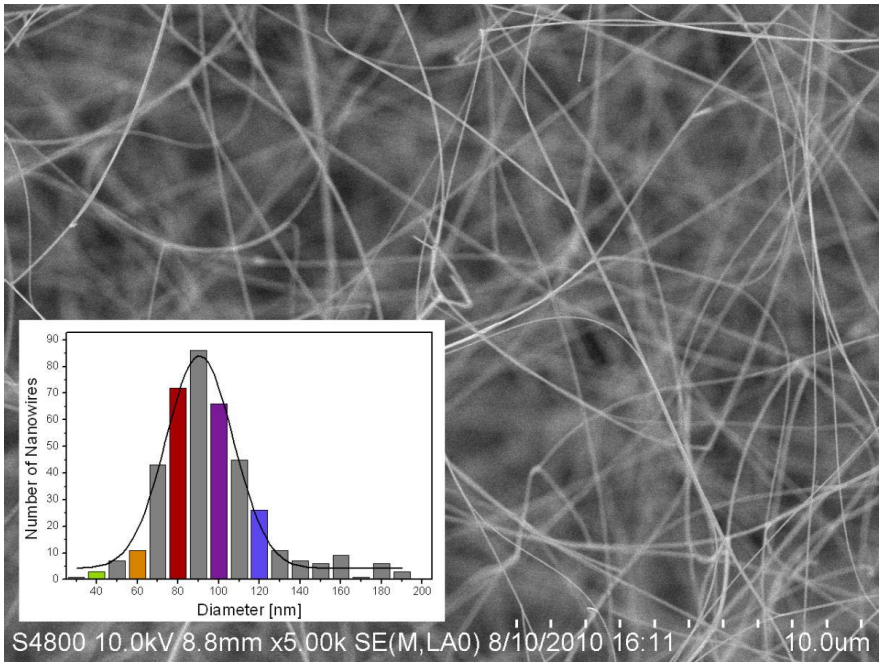

Figure 3.2: SEM image of the as-grown nanowires forest. The inset shows the NW diameter distribution, calculated on images randomly chosen on the sample.

Then, five single-nanowire devices were chosen with different diameters, in order to investigate their gas sensing properties as a function of their radial dimension. In Figure 3.2, the inset shows the different distribution points were each SNW device was chosen: nanowires diameter around 120 nm (blue), 100 (violet), 80 (red), 60 (orange) and 40 (green). Figure 3.3A shows the largest of the five SNW devices (117 nm diameter), with the SnO_2 nanowire bridging to Ti/Pt electrodes. The same colours used in the inset of

Figure 3.2 are used as borders in Figure 3.3B, showing a zoom of each of the five nanowires used as resistive gas sensors. From bottom up, we find SEM images zooms of 117 nm (blue), 103 (violet), 78 nm (red), 62 nm (orange) and 41 nm (green) nanowires used as SNW gas sensors.

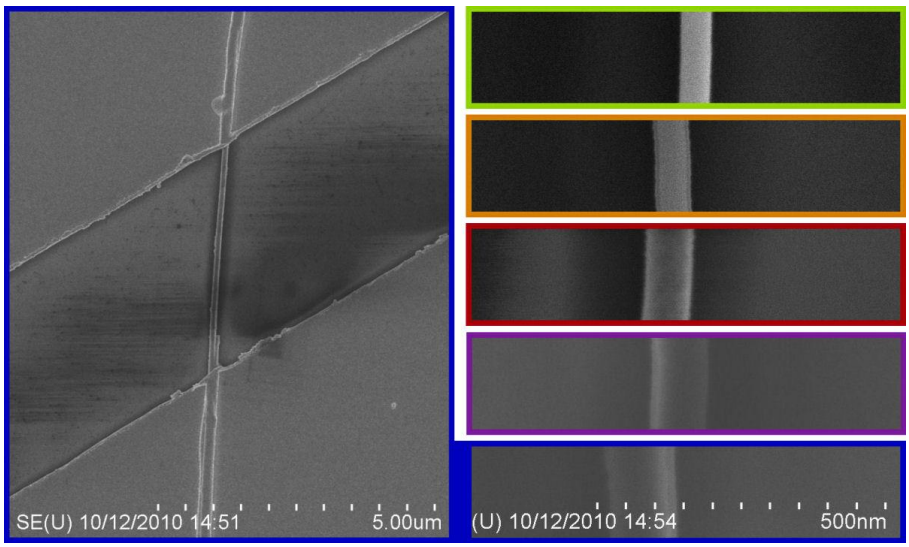

Figure 3.3: A) SEM image of a single-nanowire device, composed by the SnO_2 nanowire (117 nm diameter) bridging the two Ti/Pt electrodes. B) Zoom images of the different nanowires investigated: from bottom up, we have 117 nm (blue), 103 (violet), 78 nm (red), 62 nm (orange) and 41 nm (green).

3.3 Gas Response

3.3.1 Response as a function of working temperature

Once chosen and characterized each of the different single nanowires devices, they were put in a home-made apparatus to test their NO_2 gas sensing properties. The responses of the sensors were first checked at different temperatures ranging from 50 to 400 °C to optimize their working temperature. Figure 3.4 shows that working temperature greatly affects the

sensors response to 500 ppm of NO_2 gas. In this paper we use the definition of sensor response as $S_R = R_G / R_N$, where R_N and R_G are the electrical resistance of the nanowires exposed to nitrogen without and with NO_2 gas, respectively.

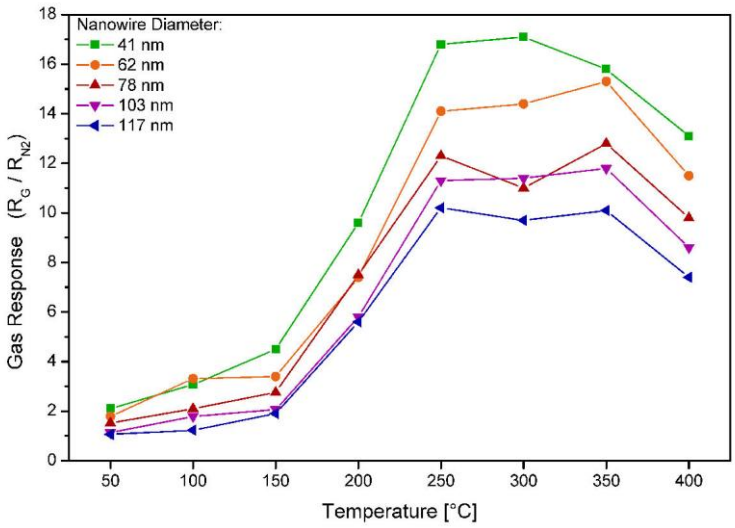

Figure 3.4: Gas response of the five SNW sensors to 500 ppm NO_2 as a function of working temperature. In the colour version (online), plot colours are the same used in Figure 2 and Figure 3.

All the five gas sensors show a bell-shape response as a function of working temperature, with a maximum response around 300°C (a plateau from 250°C to 350 °C). Such a kind of bell-shape behaviour has already been found [17,18] and is well explained by the diffusion theory [19]. All of the sensors (but the largest one) start to respond to NO_2 gas at a working temperature as low as 100 °C, but reach their maximum response at the same temperature of 250 °C. Figure 3.4 shows clearly that the maximum gas response is affected by the nanowires diameter, as is the gas response along the whole temperature range.

3.3.2 Response as a function of gas concentration

The single-nanowire gas sensors have been then investigated in terms of their response as a function of NO_2 gas concentration. As working temperature, the minimum temperature which gives an optimal response was chosen, i.e. 250 °C. Figure 3.5 compares the gas response of different diameter SNW devices to different concentrations of NO_2 gas, measured at 250 °C.

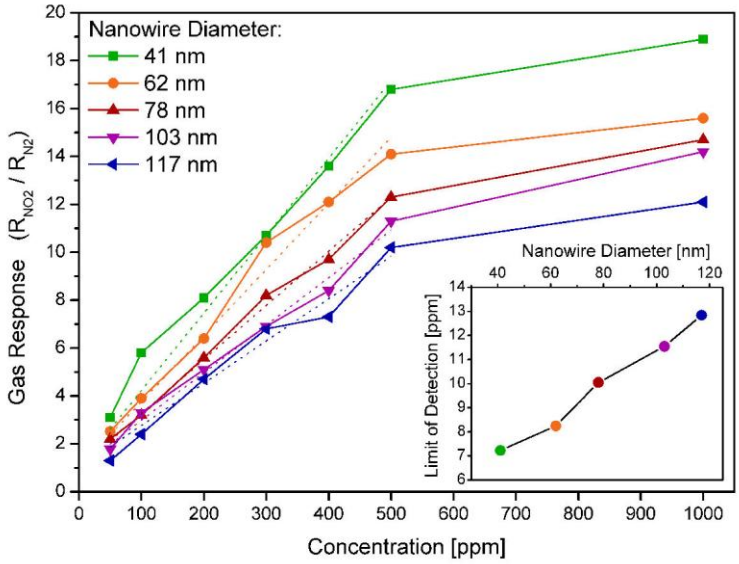

Figure 3.5: Gas response of the five devices to NO_2 concentrations ranging from 50 ppm to 1000 ppm at 250 °C. Colours are the same ones used in previous Figures.

It is easy to see in Figure 3.5 that the gas response of the device is affected by the diameter of the nanowires with which it's fabricated, along the while investigated concentration range. When the sensors were exposed to the NO_2/N_2 mixture as opposed to pure nitrogen, the resistance of the sensors rapidly increased reaching a relatively stable value. When the gas system was switched to pure nitrogen again, the resistance abruptly decreased and rapidly reached its former value. It is clear that the response of all sensors increases with increasing concentration of NO_2 from 50 ppm to 500 ppm, and

then starts to saturate. The sensor response ranges from 1.3 for 50 ppm to 12.1 for 1000 ppm of NO_2 for the largest diameter nanowire (117 nm) and from 3.1 for 50 ppm to 18.9 for 1000 ppm of NO_2 for the smallest diameter nanowire (41 nm).

Linear fits of the sensor responses in the range 50 – 500 ppm are shown in Figure 3.5. Using the slope of these linear fits, and the error on the response signal, it is possible to calculate the limit of detection (LoD) for each SNW device. In this paper we use the definition of limit of detection as three times the standard deviation of the signal, obtaining the limits of detections shown in the inset of Figure 3.5. The full circles in the inset have the usual colours used in previous Figures. It is clear that the limit of detection behaves linearly with the nanowires diameter.

3.3.3 Response stability

The gas response of the five SNW sensors is quite stable and reproducible, as can be seen in Figure 3.6. It shows the gas response of the 78 nm diameter nanowire sensor to 500 ppm of NO_2 gas at different working temperatures.

It is clear that the working temperature influences greatly the gas response. It is also evident that the gas response reacts very quickly to the injection or evacuation of the target gas, as will be discussed in the next paragraph. As a result of the initial thermal annealing at high temperature in inert atmosphere, the nanowires systems are very stable. Their response is therefore reversible and reproducible during different gas cycles (as shown for example in Figure 3.6 for 500 ppm NO_2 gas for the 78 nm diameter SNW sensor).

To express the reversibility of the sensors response, we use in this paper the definition of percentage recovery degree %R, which at maximum results to be around 2%. Such a small value confirms the good operation of the sensors in time.

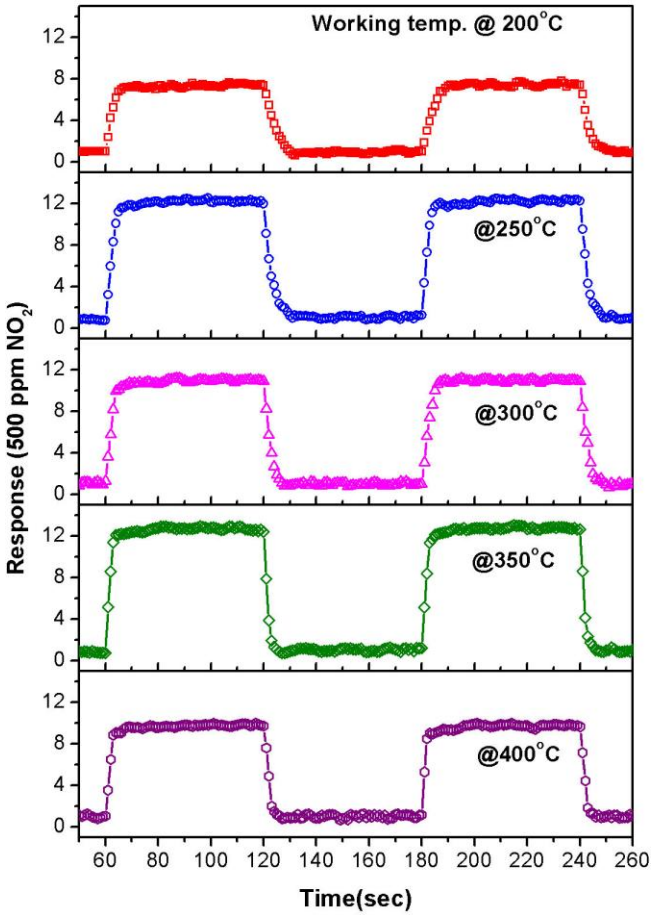

Figure 3.6: Dynamic response to 500 ppm NO_2 at different working temperatures (78 nm diameter nanowire sensor). Colours used are not related to NW diameters.

3.3.4 Response time and recovery time

Figure 3.6 makes evident that SWN gas sensors are very fast in responding to the target gas injection and to its evacuation. It is also clear, qualitatively, that both response time and recovery time are affected by the working temperature. To study more quantitatively the response time as a function of working temperature for the different SNW devices, they have been plotted in Figure 3.7a.

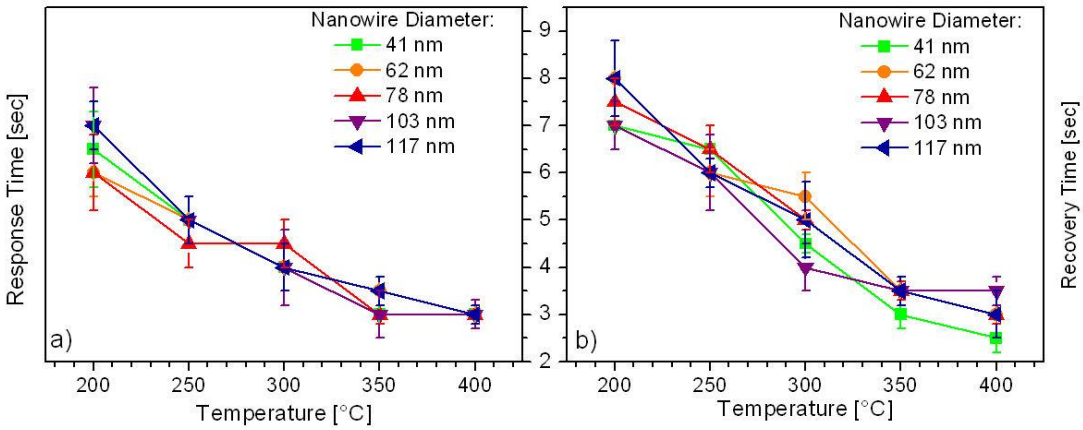

Figure 3.7: a) Response time and b) Recovery time, as a function of working temperature for the five single nanowires sensors. Colours (online version) are the same used in Figures 3.2-3.5, related to the single nanowires diameter.

Recovery times as a function of working temperature for the five SNW devices are shown in Figure 3.7b on the same time scale, for comparison. Response times range from 3.7 seconds at 200 °C to 3 seconds working at 400 °C.

Recovery times are a bit longer, ranging from 8 seconds at 200 °C to 3 seconds at 400 °C. These times are much shorter if compared with the average times for nanoparticles-based devices [20] or many-nanowires-based sensors [21,22]. In previous works, some additional methods were used to decrease the recovery time, such as UV illumination [23], high temperature treatment [24] or gate refreshing [25].

These fast response and recovery make this kind of sensing structures the ideal candidate for real-time sensing in many fields and applications. The linear dependence of both response time and recovery time is evident, while the nanowires diameter doesn't seem to affect them appreciably.

3.3.5 Depletion layer modulation model

In the previous sections we compared the sensing performance of five different single nanowire devices with different diameters. Figures 3.4 and 3.5 demonstrated that a smaller diameter gives rise to a higher response at the same working temperature. Figure 3.7a and 3.7b showed that response time and recovery time don't depend on the nanowires diameter.

In this section we use the depletion layer modulation model [26,27], that has been used before to explain the sensing mechanism of metal-oxide nanowires [28,29], to explain the gas response dependence on the nanowires diameter. Tin oxide is a well know n-type semiconductor, and nitrogen dioxide is an oxidizing gas.

When NO_2 molecules are adsorbed onto the nanowire surface, they are negatively charged, draining electrons from the tin oxide. This decreases the number of the free electrons in the SnO_2 nanostructure, leading to a depletion zone down from the surface, and increasing the resistance of the SNW sensor [30].

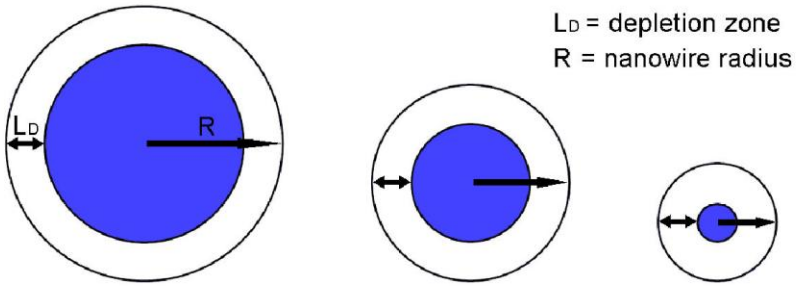

Figure 3.8: Simple sketch of the depletion layer modulation model. While the depletion depth keeps constant, the nanowires radius decreases, increasing the ratio and thus the gas response.

In the same conditions of temperature, nanostructure material and gas concentration, the depletion depth is constant in nanowires with different diameters, because it's not related to their radial dimension. A constant depletion depth and a decreasing nanostructure radius (as shown in Figure 3.8) lead to a higher gas response due to a higher ratio of conducting wire cross sections.

The whole nanowire circular section is conducting in absence of target gas. As a first approximation, we can consider that, when a certain concentration of nitrogen dioxide is injected into the chamber, the external annular region of the wire is depleted.

The depth of this depleted zone is constant in different size nanowires, giving the following simplified equation for the gas response:

$$Resp = const \cdot [R / (R - L_D)]^2 \qquad (3.1)$$

Obviously this formula assumes an external annular zone which is completely empty of charge carriers (white area in Figure 3.8), and a an internal circular zone in which the charge carriers density remains constant (blue area). This picture is maybe naïve, but can be used to calculate the depletion layer depth, and check if the whole gas sensing response can ascribed to this effect along a monocrystalline nanowires.

In order to confirm this mechanism, we plotted in Figure 3.9 the gas response of the five different sensors at different NO_2 gas concentrations. It is evident that the gas response increases with the nanowire diameter decreasing, for every gas concentration.

The symbols in Figure 3.9 are the experimental data, while the curve lines are the best fits using the equation (3.1). From these seven fits at different gas concentrations, we can extract different values for the depletion zone depth, to evaluate it.

The results obtained from the fits in Figure 3.9 are shown in Figure 3.10, as a function of NO_2 gas concentration. The average value obtained by the linear horizontal fit is 13.4 nanometres.

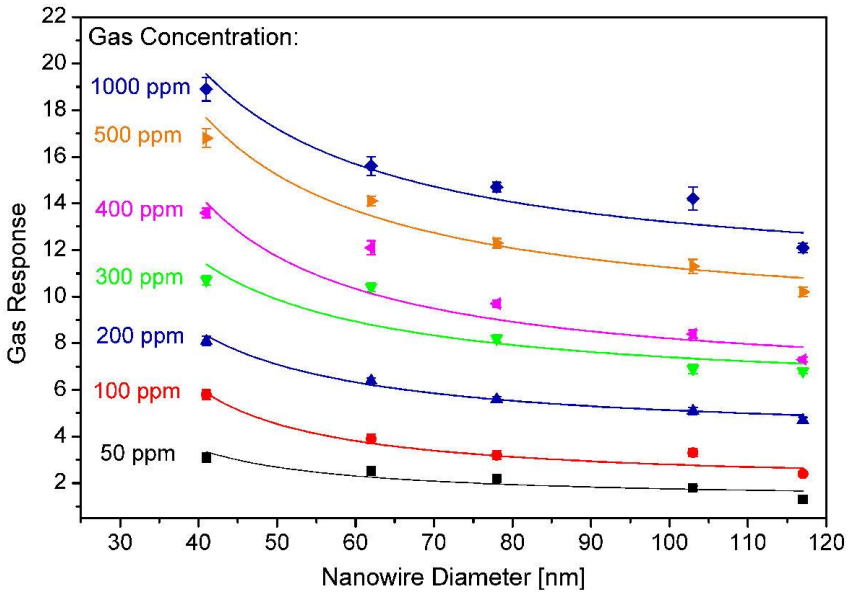

Figure 3.9: Gas response of the five SNW sensors, as a function of the NO_2 gas concentration. Colours (online) are not related to the NWs diameter.

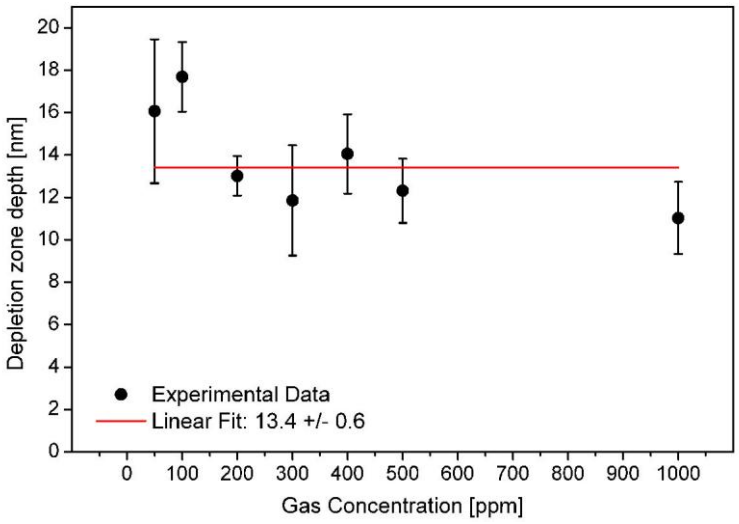

Figure 3.10: Depletion layer depth, calculated from the different fits in Figure 9.

The depletion layer depth, based on the results of Ogawa et al. [31] and McAleer et al. [32], depends on the charge carrier density, and this could

explain the different values we found (from 11.0 nm for 1000 ppm to 17.7 for 100 ppm).

It is well known indeed that metal oxide nanostructures can differ very much in their stoichiometry, due to a very rich defects chemistry. This means that, even grown in the same process, the five nanowires could have different charge carrier densities, leading to different L_D values. Anyway, the final value for the depletion zone depth, obtained from the horizontal linear fit in Figure 3.10 is 13.4 ± 0.6 nanometres. This value is in good agreement with literature [31,32].

This result confirms the depletion layer modulation model as gas sensing mechanism for monocrystalline single nanowires devices.

[1] B. Hoffheins, *Solid state, Resistive gas sensors, Handbook of Chemical and Biological Sensors*, Ed. R.F. Taylor and J.S. Schultz, Philadelphia 1996.

[2] Q. Wu, J. Li and S. Sun, *Current Nanosci.* 6 (2010) 525-538.

[3] M.E. Franke, T.J. Koplin and U. Simon, *Small* 2 (2006) 36.

[4] V. Malyshev, A. Pislyakov, *Sens. Actuator B* 123 (2007) 71-81.

[5] G. Korotcenkov, *Mater. Sci. Eng. B* 139 (2007) 1-23.

[6] Y. Yin, G. Zhang and Y. Xia, *Adv. Funct. Mater.* 12 (2002) 293.

[7] P. Yang and C.M. Lieber, *J. Mater. Res.* 12 (1997) 2981.

[8] Z.R. Dai, J.L. Gole, J.D. Stout and Z.L. Wang, *J. Phys. Chem.* B 106 (2002) 1274.

[9] X.Y. Kong and Z.L. Wang, *Nanolett.* 3 (2003) 1625.

[10] C.S. Moon, H. Kim, G. Auchterlonie, J. Drennan and J. Lee, *Sens. Actuator B* 131 (2008) 556-564.

[11] G. Korotcenkov, *Sens. Actuator B* 107 (2005) 209-232.

[12] S.M. Sedghi, Y. Mortasavi and A. Khodadadi, *Sens. Actuator B* 145 (2010) 7-12.

[13] N. Yamazoe, G. Sakai and K. Shimanoe, *Catalysis Surv. Asia* 7 (2003) 63-75.

[14] F. Hernández-Ramírez, A. Tarancón, O. Casals, J. Arbiol, A. Romano-Rodríguez and J.R. Morante, *Sens. Actuator B* 121 (2007) 3-17.

[15] F.L. Deepak, P. Saldanha, S.R.C. Vivekchand and A. Govindaraj, *Chem. Phys. Lett.* 417 (2006) 535-539

[16] A. Tischner, T. Maier, C. Stepper, A. Köck, *Sens. Actuator B* 134 (2008) 796-802.

[17] L.V. Thong, N.D. Hoa, D.T.T. Le, D.T. Viet, P.D. Tam, A. Le and N.V. Hieu, *Sens. Actuator B* 146 (2010) 361-367.

[18] A. Forleo, L. Francioso, S. Capone, F. Casino, P. Siciliano, O.K. Tan and H. Hui, *Sens. Actuator B* 154 (2011) 283-287.

[19] G. Sakai, N. Matsunaga, K. Shimanoe, N. Yamazoe, *Sens. Actuators B* 80 (2001) 125-131.

[20] N.M. Shaalan, T. Yamazaki and T. Kikuta, *Sens. Actuator B* 153 (2011) 11-16.

[21] Y. Choi, I. Hwang, J. Park, K.J. Choi, J. Park and J. Lee, *Nanotechnology* 19 (2008) 095508.

[22] B. Kim, D. Lim, J. Park, Y. Choi and J. Park, *Appl. Surf. Sci.* 257 (2011) 4715-4718.

[23] J.D. Prades, R. Jimenez-Diaz, F. Hernandez-Ramirez, S. Barth, A. Cirera, A. Romano-Rodriguez, S. Mathur and J.R. Morante, *Sens. Actuator B* 140 (2009) 337-341.

[24] D. Briand, H. Wingbrant, H. Sundgren, B. van der Schoot, L.G. Ekedahl, I. Lundstrom and N.F. de Rooij, *Sens. Actuator B* 93 (2003) 276-285.

[25] Z. Fan and J.G. Lu, *Appl. Phys. Lett.* 86 (2005) 123510.

[26] J. Goldberger, D. Sirbuly, M. Law and P. Yan, *J. Phys. Chem. B* 109 (2005) 9-14.

[27] D. Wang, Y.L. Chang, Q. Wg, J. Cao, D. Farmer, R. Gordon and H. Dai, *J. Am. Chem. Soc.* 126 (2004) 11602-11.

[28] L. Liao, H.B. Lu, J.C. Li, H. He, D.F. Wang, D.J. Fu, C. Liu, W.F. Zhang, *J. Phys. Chem. C* 111 (2007) 1900.

[29] M. Tonezzer and R.G. Lacerda, *Sens. Actuator B* 150 (2010) 517-522.

[30] Y. Shimizu, M. Egashira, *MRS Bull.* 24 (1999) 18-24.

[31] H. Ogawa, M. Nishikawa, A. Abe, *J. Appl. Phys.* 53 (1982) 4448.

[32] J.F. McAleer, P.T. Moseley, J.O.W. Norris, D.E. Williams, *J. Chem. Soc. Faraday Trans.* 1 (83) (1987) 1323-1346.

Chapter 4

Small conjugated molecules

4.1 Organic semiconductors

Organic materials offer nowadays a series of properties that stimulate fundamental investigations in physics, chemistry and materials science [1]. Through careful design and manipulation of a wide range of carbon-based structures, organic/polymer materials are able of acting as electronic conductors, semiconductors, and insulators [1]. For these reasons, the organic materials seem to be the answer to several problems [2], especially playing a crucial role in devices fabrication.

The goal behind the experimental work which lead to this thesis (the part concerning organics), was the realization of ordered structures of small-molecules thin films usable towards sensing applications. In the following, we will describe in brief the small molecules of interest for possible applications in the field of electronics and sensing.

Figure 4.1 shows the structures of the organic semiconductors which we used as investigation molecules for the growth of thin films by Supersonic Molecular Beam Deposition (SuMBD). As all the molecules used as organic semiconducting materials, they are characterized by a large π-conjugation. This electron delocalization is accountable for how these organics interact with light and behave in electronic transport properties and hence for their semiconducting [3],photovoltaic [4],and gas sensing [5] properties, which make these molecules technologically very attractive.

The interesting perspective opened by the chemical design of molecular properties faces a series of complications that present research efforts are dealing with: energy and electron transport strongly depend on structure and morphology of the material and of the its interfaces.

So a better understanding and control of charge injection requires order and purity in the solid state [6], control and understanding organic-inorganic (metal contacts) [7,8,9] and organic-organic [10] interfaces and stability in various working environments, including exposure to oxygen and light [11]. All these aspects will be critical for the technological impact of the field molecular electronics.

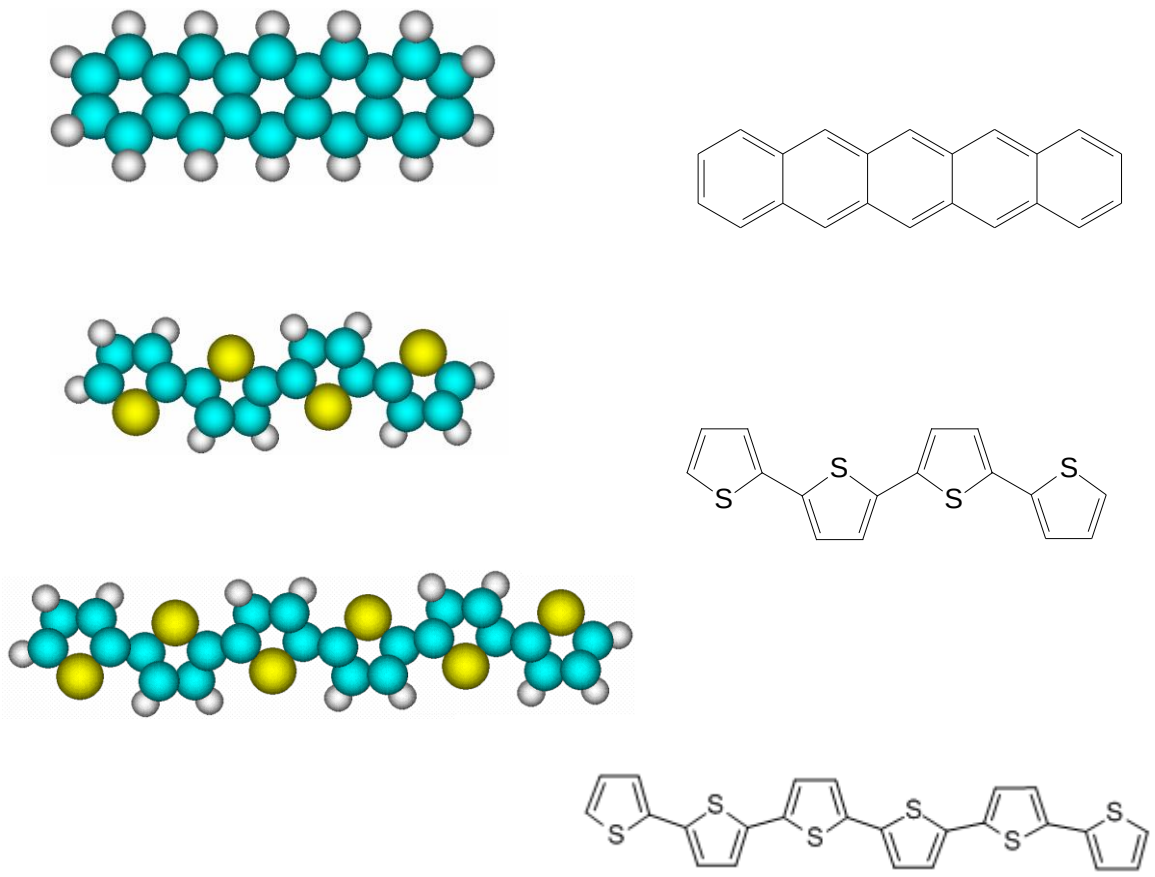

Figure 4.1: Chemical structure of some organic semiconductors that have been used for testing the supersonic molecular beam deposition. From top to down: Pentacene (Pen); alpha-quaterthiophene (α-4T); alpha-sexithiophene (α-6T).

Up to now the research efforts were intended principally at understanding which are the bottlenecks restraining the performance of these

materials related to interfaces [9], and to the growth of well-ordered structures [12]. How the metal-organic (MO) or organic-organic (OO) interfaces are formed determines the injection of charge carriers into the thin molecular films and the charge transport from side to side of the device.

Given their evident importance, these MO and OO semiconductor interfaces have been the focus of many fundamental and phenomenological studies aimed at understanding their electronic and chemical structure, at controlling interface energy barriers and, in the case of MO interfaces, at optimizing the injection of charge carriers [13] to improve device performance.

We know that interfaces control is of main importance in the fabrication of performing devices, but the second aspect (the growth of ordered films) plays a crucial role in the interface creation too. In fact, the electronic properties of organic semiconductors are strongly dependent on the structure and morphology of the films. In general, organic semiconductors are molecular solids with quite weak van der Waals interactions.

The large molecular dimension and asymmetry, typical of these compounds, facilitates the presence of different crystalline packings with dissimilar optical and electronic properties. Often a number of of these structures coexist in the same film [14], a phenomenon called *polymorphism*. Since the molecules have more degrees of freedom than atoms, the growth scenarios are much more complex than for inorganic semiconductors. Consequently, very often the thin films are amorphous or polycrystalline.

The presence of a large amount of grain boundaries decreases the carrier *mobility* (the figure of merit that characterizes the performance of semiconductor devices) due to the existence of potential barriers that the carriers need to pass in order to move inside the film. Hence, the stimulus for maximizing the structural order and the charge injection (*ohmicity*) of contacts [8].

4.2 Growth technique: Supersonic Molecular Beam Deposition

The first molecular beam experiment carried out by Dunoyer (in 1911) was realized immediately after the invention of the high speed vacuum pump (1910). Following this pioneering work, free jets and supersonic molecular beam methods were used for over a half century in many historical experiments investigating basic principles of modern physics [15], several of which were awarded with the Nobel prize.

As examples of fundamental discoveries made thanks to this technique we cite the confirmation of the Maxwell-Boltzmann velocity distribution in 1920 by O. Stern using Ag atom beams, and the famous experiment by W. Lamb and R. Rutherford demonstrating in 1947 the fine structure of the first electronically excited state of the hydrogen atom.

In the sixties, a theoretical treatment of the expansion was made. Ashkenas and Sherman gave an important step in this direction in 1964 [16], when they showed that using the Mach number (M) distribution and the classical equations of isoentropic expansion, the local pressure, the number density and temperatures can easily be calculated. The limitation of this treatment concerning supersonic free jets is that the equation is valid only for expansion in a perfect vacuum [17].

From the experimental point of view, if the background pressure (P_b) is higher than about 10^{-3} Pa, the background molecules invading the free jet are detrimental to the free expansion. Working at higher P_b ($1 < P_b < 100$ Pa) is also possible, but in this case the free jet develops a typical shock wave structure which lets the core portion of the expansion unaffected by the background conditions; this area is called the "*zone of silence*" [18].

This area is limited by the *Mach disk*, which for axis-symmetrical free jets is defined by: $X_M / D = 0.67 \cdot (P_0/P_b)^{1/2}$ where X_M is the axial distance with respect to the nozzle, D the nozzle diameter and P_0 the stagnation pressure. Inside the "zone of silence" the molecular properties can be treated as if they were in a free expansion in vacuum [18]. Another noteworthy characteristic shown by Kantrowitz and Grey in 1951 [19], is that the physical properties of

the supersonic molecular beams skimmed from a free jet expansion are the same as those in the final stage of the expansion.

Hence, the stagnation temperature, T_0, gives the final kinetic energy of the jet molecules, the product $P_0 \cdot D$ gives information about the number of single collision between the molecules and $P_0^2 \cdot D$ gives information about the three-body collision [15].

The geometrical form of the skimmer is crucial to avoid any perturbation of the supersonic expansion, particularly in the case of continuous flow, if a high value of $P_0 \cdot D$ has to be achieved [18].

The supersonic beams have become very popular as the ideal setting to investigate free molecules because of their narrow velocity distribution and the strong cooling effects that permit to study the spectroscopy of large cold molecules [17,18,20] to characterize their properties in the fundamental state [21]. Furthermore, many other remarkable modifications and results from the supersonic expansion can be investigated and exploited in molecular beams skimmed from free jets, such as:

- alignment of the rotational momentum [22]
- high vibrational and very low rotational temperatures
- production of van der Waals molecules, clusters, and nanoparticles, a new low-density state of matter [17]
- developments in nanoscience and nanotechnology [23].

The supersonic molecular beam which started out as a peculiarity of the gas phase in the early experiments in the middle of XX, century nowadays shows diverse and very interesting possible applications.

We can resume this little excursion on the supersonic free jets saying that a supersonic molecular beam source converts the “molecular chaos” of a gaseous medium into a focussed and collision-less beam allowing to take advantage of its propagation (and kinetic energy) and to produce local interactions with another beam (gas or laser) or with a surface.

This last aspect plays a crucial role in our research towards the develop of new growth (“interaction with surface”) methods that permit to

reach an improved control in the realizing ordered structures of thin film of organic molecules.

4.2.1 Supersonic Seeded Beams vs MBE

We will now briefly summarize the principal differences between usual MBE and SuMBD. The most important dissimilarity, is that Knudsen cells and the effusive beams are characterized by processes at the thermal equilibrium, while supersonic beam sources and free jets are characterized by non-equilibrium processes. Indeed, comparing the Knudsen number K_n, the spatial evolution of temperature (from T_0 to final value T_f) and pressures (from P_0 to the final P_f) we find very different behaviours.

The main differences between an effusive and a supersonic beam can be schematically summarized as follows:

- Knudsen number K_n: while for effusive beams $K_n > 1$, its value becomes $K_n << 1$ for supersonic beams. In the latter case, the gas is *underexpanded*. At the nozzle exit an isoentropic expansion and a huge number of collisions take place, giving rise to a series of non-equilibrium processes. The flow becomes completely free without any molecular collision (as in typical effusive beams) after a distance of some nozzles diameters.
- Final velocity (v_f): starting from the same initial conditions, in supersonic beams v_f is generally much larger than in effusive beams, and seeding effects play a very important role in free jets. In fact, using species with lighter mass as carrier gas, the final velocity increases while using a heavier species (hydrodynamic acceleration) it decreases. The velocity of an effusive beam reproduces instead the energy distribution defined by the Boltzmann law for that particular oven temperature.
- Velocity spread: in an effusive beam, this value is defined by the temperature of the oven (again the Maxwell-Boltzmann dstribution). In a free jet this value depends on the Mach number M. In a very good

expansion this value can become very low ($\Delta v / v < 1\%$). Figure 4.2 shows a comparison between a free jet with M = 50 and a Knudsen cell originating from the same temperature conditions in the source.

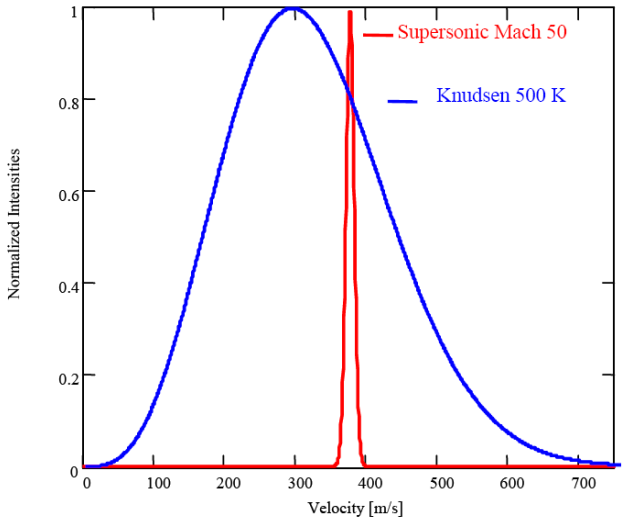

Figure 4.2: Velocity distribution comparison between supersonic beam (red) and Knudsen cell (blue). Both sources are at the same stagnation temperature. Adapted from reference [23].

- T_f and P_f: for a supersonic beam these values are considerably smaller with respect to the stagnation values, and they depend on M. In a Knudsen cell at thermal equilibrium, there is no difference between initial and final temperatures and pressures.
- Cooling down of internal degrees of freedom: the free jet expansion produces a very fast and effective cooling of the internal degrees of freedom of the seeded species. The efficiency depends on the energy spacing of the roto-vibrational states of the molecules. No such effect is present in a Knudsen cell. Here the population of each state is defined by the standard distribution given by the temperature of the source.
- Angular distribution: supersonic molecular beams have a very high forward intensity, narrowly peaked along the beam axis, while in effusive molecular beams the intensity follows a cosine-like angular distribution as shown in Figure 4.3.

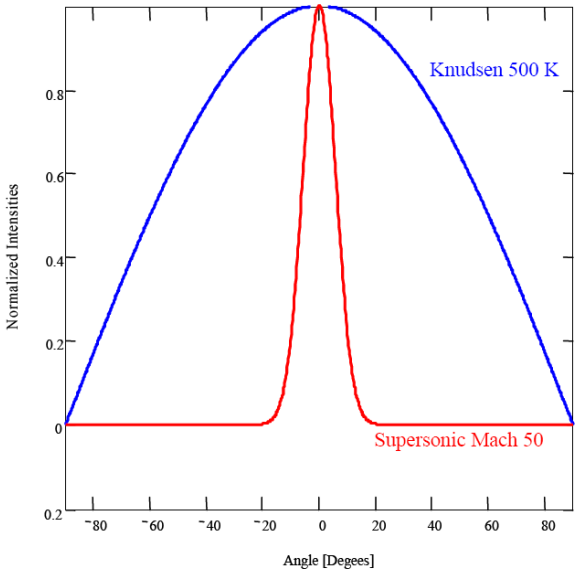

Figure 4.3: Angular distribution comparison between supersonic beam (red) and Knudsen cell (blue). Both sources are at the same stagnation temperature. Adapted from reference [23].

4.3 Organic thin film growth

As we have seen in the previous chapters, our goal is the development of a growth method for organic semiconductors that permits to achieve a better control of the final properties of the film. Since the molecules have to be sublimed in order to be seeded into the supersonic molecular beam, we shall centre our attention on three low molecular weight compounds (small conjugated molecules): α-quatertiophene, α-sexithiophene and pentacene.

This choice is also motivated by the fact that these materials are suitable for fundamental studies, mainly because they form well-ordered crystalline structures [24] and can be considered as model systems for understanding the properties of polymers, in particular the mechanisms governing the charge transport. Although the detailed mechanism governing the transport of electrical charges in organic materials is at present not well understood, it is understandable that the structure of the molecular solid through which the charge carriers travel plays a fundamental role [25].

In order to better understand the processes involved in the growth of the organic layer and in the interaction between molecules and surface, we will illustrate the gas-surface interaction and give a general overview of the processes involved. After this brief discussion, we will describe in detail the thin film growth method and the principal laws that control the vacuum deposition processes.

We will then detail the growth of the different small conjugated molecules comparing the results achieved with high energy SuMBD with "standard" low energy depositions, and illustrate the advantages of the control on the energetic parameters of the precursor.

In a high vacuum MBE classical deposition, the evaporation or sublimation of the material occurs in thermal equilibrium conditions. In these conditions, the molecules or atoms hit the substrate at thermal energies and go through a series of possible processes described in figure 4.4 [26].

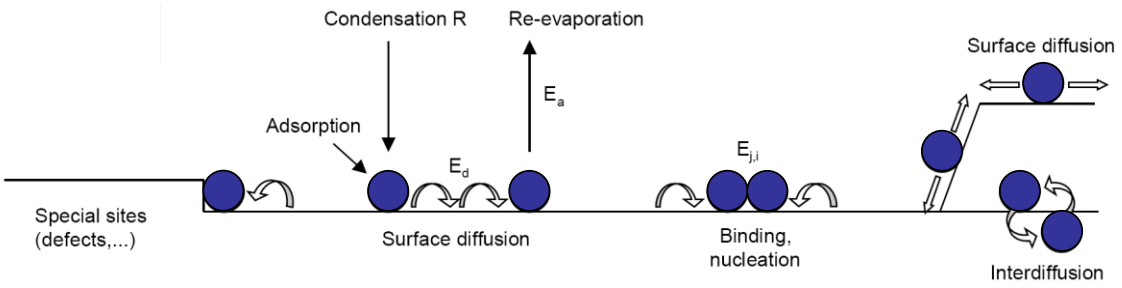

Figure 4.4: Processes and energies involved in nucleation and growth on a surface. Adapted from reference [27].

We assume a constant rate of arrival *R,* given by the equation $R = P\cdot(2\pi mkT)^{-1/2}$ where *P* is the vapour pressure of the gas, *m* the molecular weight, *k* the Boltzmann constant and *T* the source temperature. When an adsorbate reaches the substrate, it may diffuse on the surface with a diffusion energy E_d that consents the adsorbate to move on the surface. It may re-evaporate into vacuum, where this re-evaporation process is characterized at low coverage by a characteristic time τ_a which can be written as:

$$\tau_a = \upsilon^{-1} e^{\left(\frac{E_a}{kT_s}\right)} \tag{4.1}$$

where T_s is the substrate temperature, υ a characteristic surface vibration frequency and E_a the energy necessary for the adsorbate to re-evaporate. It may also nucleate in 2D or 3D islands where E_i is the nucleation barrier height. The adsorbate can aggregate with existing islands where E_j is the binding energy of a molecule in a cluster of j molecules. These last two energies (E_i and E_j) provide information about the smallest amount of molecules needed to form a stable cluster that will be the starting point for the island formation.

Alternatively, the adsorbate may undergo inter-diffusion processes generated by chemical reactions or by defect sites (I must stress that on real surfaces a distribution of dislocations and point defects can strongly affect absorption, diffusion and nucleation). Also, steps or surface defects act as nucleation sites promoting local island formation. If the adsorbate has enough energy, it will be even capable to “climb a step” on a molecular monolayer and grow over it.

Steps introduced by the forming island are worthy of particular attention in this respect: if the adsorbate has enough energy to climb such steps, the formation of a second layer will start *before* the first layer is completed, giving rise to 3D growth. Finally, re-arrangements may occur if the initially formed adsorbate cluster or island is not in its most stable form: it will rearrange in many different ways to minimize its energy. These processes may include shape changes by diffusion or coalescence, annealing of defects, etc. The final morphology of the film is the result of part or even all these processes.

In general, once the aggregation process begins, thin films can grow in atomic MBE in one of the three ways reported in figure 4.5, as discussed in [27,28]:

- *Layer by layer (*or *Frank-Van der Merwe)*: occurs when the adatoms diffuse to form 2D islands. In this case, the adsorbates are more strongly bonded to the substrate then to other adsorbates. Only after the complete formation of the first monolayer, the second one begins to grow. To favour diffusion, the deposition rate must be not too high

(the same effect can be reached in some cases by increasing the substrate temperature). In this mode, the formation of a new layer begins just before the old one is almost complete.

- *Cluster or Island (*or *Volmer-Weber)*: occurs when the interactions among the adsorbates are stronger then those with the substrate, leading to 3D islands. It begins with the nucleation of small clusters and then proceeds with the growth of 3D islands. This mode usually occurs also when the deposition rate is high and the diffusion length of the adatoms on the substrate is low.
- *Layer plus Island (*or *Stranski-Krastanov)*: the film develops islands after one or more uniform layers. This regime can be considered as an intermediate case. Since the layer-by-layer growth imposes an energy barrier to nucleate new islands every time a layer is completed, this initial process tends to convert into a much faster, defect-assisted growth mode such as the *cluster or island mode*. There are many possible reasons for this to happen: for instance, if the lattice parameter or the molecular orientation in the growing film is not consistent with that of the bulk crystal the surface high free energy may favour subsequent island formation [29]. Examples of this growth mode are organics on metals or insulators [25,30].

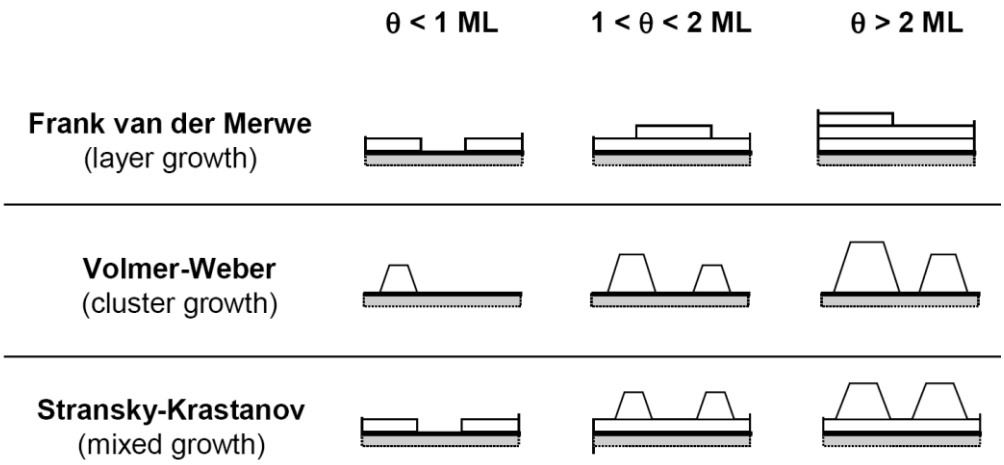

Figure 4.5: Typical MBE growth regimes: (a) 2D *layer by layer* (b) 3D *island* (c) mixed *layer plus islands*. Adapted from reference [27].

The ideal conditions for a given growth mode are a delicate equilibrium of the anisotropic interactions between the molecules and their neighbours as well as with the substrate [31].

A general representation, helpful to understand the growth of different organic materials such as pentacene, is the *diffusion-mediated growth* model that explains the formation of the first monolayer through the description of different phases of the growth. The evolutions of islands size, density and distribution become functions of the coverage θ and of the deposition rate *R.* The description of the model involves four steps [32]:

- The first step is the *low-coverage nucleation regime.* The molecules diffuse on an almost uncovered substrate and when a critical number of them meet together, a stable nucleus is formed [33]. In this regime, the island density is much smaller than the monomer density, so that the probability of island growth is much smaller than the probability of nucleation. Therefore, the average island size results very small.
- The second one is the *intermediate coverage regime.* Here the adsorbates still nucleate new islands but also start to aggregate with the existing ones. As the coverage increases, the monomer density begins to decrease, while the island density continues to increase but much more slowly than in the nucleation regime.
- In the third one, the *aggregation regime*, the incoming material aggregates with the existing islands. No more formation of new islands happens. The monomer density in this case decreases very rapidly. The island diameter is of the order of the distance between the islands, while the portion of the surface covered by islands is large enough that one must take into account the probability of deposition onto an island as well as onto the substrate.
- Finally, in the *coalescence and percolation regime*, the islands begin to merge and eventually penetrate each another. Due to this effect, the island density rapidly decreases while the monomer density increases (but obviously this is due to the formation of a second layer).

This model is suitable especially in the case of dendritic islands growth. Also in the case of organic materials, the description given by this model may be considered fitting [34,35].

The condensation regime plays a key role in the growth process. The homogeneous nucleation and growth is based on the rate-equation formalism that has been systematically developed in particular by Venables [27,36] and experimentally verified for inorganic systems; in these last years several studies applied this model trying to make the growth of organic materials on dielectric substrates clear [30,37].

The main principles of this model can be summarized as follows: any evaporation or condensation process is characterized by the "rate equations" which relate parameters such as the grain density *N,* the deposition rate *R*, a growth determining constant *p* and the total energy *E* of the system. The constant *p* is defined by the critical nucleus size *i* of the deposited material. The solution of the rate equations leads to a characteristic island size distribution and the island density, *N*, can be written as

$$N \propto R^{p} e^{\left(\frac{E}{kT_s}\right)} \qquad (4.2)$$

In other words, in the case of homogeneous nucleation, the density of stable islands is expected to vary as a power law with the deposition rate *R* and as an activated Arrhenius law with the substrate temperature T_s.

Thus *N* decreases when T_s increases and when *R* is decreases. *E* is a function of the activation energy for desorption (re-evaporation) of molecules from the substrate E_a, and of the free energy difference E_i (defined as the difference of energy between the *i* molecules in the forming island and in the adsorbed state), and the diffusion energy E_d.

Note that *i* denotes the critical nucleus size, meaning that an island of *i* molecules is almost unstable and will dissociate, while stable islands start to grow from a size equal to *i*+1. The exact dependence of *E* on the various activation energies E_a, E_d and E_i depends on the condensation regime as well as the dimensionality of the clusters (2D *vs* 3D). In some cases, different

authors reported different values of the critical nucleus size *i* [30,37,38] for similar growth conditions (type of surface, deposition rate etc.).

In most of the cases this is related to different experimental conditions or different points of view on the starting point of the experiment (i.e. if the re-evaporation process is considered more or less important in the applied model) [27,39].

In particular, three different condensation regimes [27] can be considered:

- *Complete condensation*: occurs if all adsorbates arriving at the substrate reside there by binding or nucleation. Therefore, the desorption energy E_a does not enter in the total energy equation and re-evaporation from the substrate can be ignored.
- *Extreme incomplete condensation*: describes the opposite case, when re-evaporation plays a crucial role.
- *Initially incomplete condensation*: occurs when condensation is incomplete on the substrate, but clusters capture atoms by surface diffusion. The bond between adatoms is stronger than that with the substrate. Note that when the island coalescence stage is reached, this regime corresponds to complete condensation [27].

Regime	**Parameters p,E**	**p(i=1)**	**p(i=2)**	**p(i=3)**
Extreme Incomplete	$p=i$ $E\approx[E_i+(i+1)E_a-E_d]$	1	2	3
Initially Incomplete	$p=i/2$ $E\approx1/2(E_i+iE_a)$	0.5	1	1.5
Complete ($E_a=0$)	$p=i/(i+2)$ $E\approx(E_i+iE_d)/(i+2)$	0.33	0.5	0.6

Table 4.1: Growth regimes and parameters as a function of the nucleus size *i.*

Table 4.1 reports the typical value obtained for the parameters that characterize the growth processes for the three regimes.

After this introduction a question arises: “Is it possible to modify the growth parameters to improve the order in our films?”. Considering molecular beam deposition (MBD), we have the possibility to operate only on a few parameters, that are:

- *The nature and morphology of the substrate:* the substrate’s chemical properties and structure (crystalline or amorphous, flat or rough) play a fundamental role in the formation of the first adsorbate layer. The morphology of the substrate affects the nucleation of aggregates, and can be the determining factor in limiting the degree of order inside the thin film. Defects and impurities can act as traps for the adsorbates, leading to an increase of nucleation and formation of irregular grains. The surface energy, determined by the hydrophobic or hydrophilic character of the substrate, modifies the type of interaction between substrate and adsorbate [40]. Obviously, the surface properties depend on the treatment the surface has been subjected to i.e. cleaning processes or chemical modification.
- *Temperature of the substrate* T_S: as already mentioned, a higher temperature may enhance the diffusion of the adsorbates on the substrate, inducing a higher degree of order in the growth for some materials. On the other hand, at higher substrate temperatures the re-evaporation of adsorbates may be enhanced, reducing the diffusion length of the adsorbate on the substrate and thus the coalescence of the grains can be affected by this process, giving rise to different regimes of growth [27,35].
- *Deposition rate R:* it depends on the flux of impinging particles *F* and on their diffusion length on the substrate *D* ($R = F / D$). The formation of the first layers can be understood in terms of atomistic theory like the kinetic rate equation [41], which describes the concentration of particles on the substrate resulting from the balance between the number of impinging molecules (governed by deposition rate) and those evaporating or nucleating to form islands.

- *Film thickness*: etero-epitaxial layers have the substrate lattice spacing in the plane, but a different spacing out of the plane. The associated lattice strain is relieved at a critical thickness where the elastic strain energy equals the interface energy increase upon strain relief. Hence, if the growth exceeds the critical thickness, the structure of the film changes. For example, pentacene thin films are often characterized by two co-existing phases: near the substrate a so-called “thin film phase” is often present with a crystalline form that is influenced by the substrate-adsorbate interaction. Instead, after the critical thickness has been reached, a different phase called “bulk” is present with a crystalline form that is less affected by the substrate and more similar to the single crystal phase [42].

On substrates characterized by weak interaction, such as oxides and most polymeric substrates, the general model of *diffusion mediated growth,* explained previously, can be applied to the pentacene first monolayer growth. In this case, in order to give a comprehensive panorama of the regimes defined for this model and strongly dependent of the growth parameters, it is useful to refer to Figure 4.6 where substrate temperature and deposition rate are considered as growth parameters to locate the different growth regimes.

- *Single phase layered growth*: presents a regime of growth of layer plus island (mixed growth) with the presence of terraces and ziqqurat structures. The dimensions of the terraces may vary depending on substrate temperature and deposition rate. The steps have typically the height of the molecules. Evidence of fractal structures and branches can be present, with different grain border morphologies and dimensions of the grains. Condensation is initially incomplete and the size of the critical nucleus, *i,* is 3 (stable islands starts to grow from size *i*+1) [37].
- *Low supersaturation and dislocation assisted growth*: in this regime, the diffusion of the adsorbates is so low that very highly dendridic structures are generated and extremely incomplete condensation occurs. At low supersaturation, the nucleation rate is very low and

growth occurs predominantly at surface steps and is associated with screw dislocations. This regime occurs at high substrate temperature and low deposition rates.

- *Amorphous film limit*: these conditions arise when the temperature of the substrate is too low or the deposition rate is too high and the adsorbate diffusion is too limited to produce a polycrystalline structure.

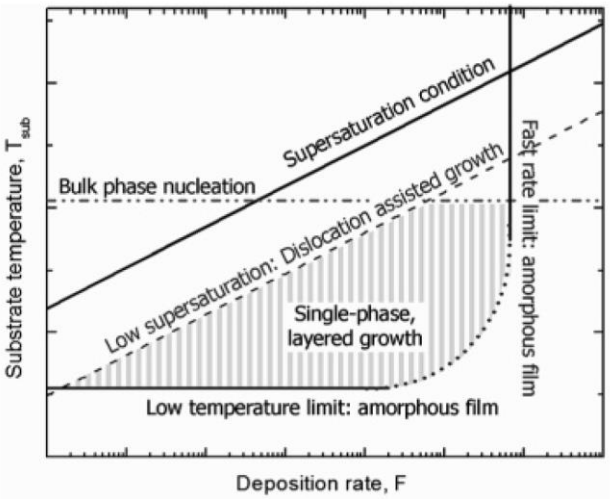

Figure 4.6: Qualitative description of the borders for layer-by-layer pentacene growth. A crystal can be grown below the line for the supersaturation condition. The high-temperature limit is set by the nucleation of the bulk phase. Amorphous films result at high rates or low substrate temperatures. At low supersaturations, growth may become dislocation-assisted. From reference [35].

The morphology of the grains is controlled by the coalescence regime and by the diffusion length of the adsorbates on the substrate, parameters that change also the condensation regime. In particular, at low deposition rates, the reduction of the diffusion length causes the formation of dendritic grains with irregular and diffused grain borders [30]. This fact implies that with MBE deposition it is a very difficult to obtain an accurate layer-by-layer growth with a low presence of grain boundaries.

Based on this discussion, the conditions to create larger grains are high substrate temperature and low deposition rate that also favours the

formation of irregular dendritic grains and deeper grain boundaries due to low diffusion length. Moreover, dendritic, irregular and randomly oriented grains form angles that hinder a correct matching of pentacene crystalline cells between two grains, and therefore prevent their coalescence in a larger crystallite. Instead if the grains are regular in shape and/or preferentially oriented one respect to the other, coalescence will easily occur, forming a continuous crystal.

4.3.1 Diffusion length and island shape

The shape of the island formed by the adsorbate on the substrate surface, in the first monolayer (and subsequently in the successive layers) can range from round and regular to fractal with ramified branches. These shapes strongly affect the morphology and the properties of the film. In fact, the probability of capture is larger for fractal islands than for compact islands, according to the relationship between the island cross section and its surface.

To give a correct explanation of the fractal or round shape of a grain, a more detailed picture has to be given of the interplay between surface diffusion and re-evaporation of molecules during the formation of the first monolayer. In the phenomenological capture zone model, proposed by Mulheran and Blackman [43], the stable nuclei grow at a rate proportional to the polygonal areas defined by Wigner–Seitz cells built on the initial distribution of nuclei in the substrate plane.

In fact, form factor and island size distributions can be interpreted in terms of a balance between the mean nearest neighbour (*NN*) island distance λ_{NN},, and the mean distance covered by a diffusing adsorbate before desorbing [44] λ_D, via the formula $\lambda_D = (D \cdot \tau_A)^{½}$, where D is the diffusion constant and τ_A the mean residence time of molecules on the substrate. While λ_{NN} varies as $N^{-½}$, λ_D is expected being constant at fixed T_s. We can distinguish two growth behaviours as a function of deposition rate, as shown in figure 4.7:

- $2\lambda_D < \lambda_{NN}$. In the case of low deposition rate, if an adsorbate lands on the surface far from an existing nucleus, its probability of re-evaporate is large due to the long diffusion path that it has to cover before reaching an island. Accordingly, the amount of admolecules incorporated into a given island is no longer determined by the geometrical area of its Wigner-Seitz cell, but depends on the island morphology and on the diffusion length, λ_D: at a given moment, the capture zone will be roughly defined as the area inside the dotted line exceeding the border of the dendritic island by λ_D as sketched in figure 4.7. This has several implications: first, the proportionality between the capture zone, defined as the Wigner-Seitz cell, and the growth rate of an island is no longer verified; secondly, in absence of overlap between adjacent capture zones, *NN* islands tend to grow in a uncorrelated way. This results in a broad island size distribution and a fractal island morphology typical for the diffusion limited aggregation (DLA) model.

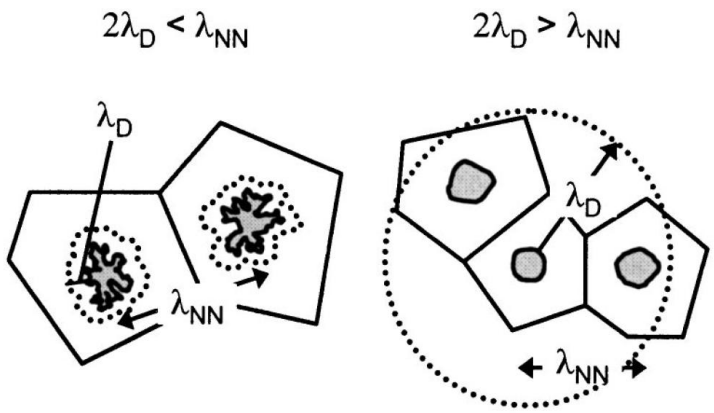

Figure 4.7: Simple sketch showing the effect of the interplay between the mean inter-grain distance λ_{NN} and the diffusion distance λ_D on the growth mechanism in the sub-monolayer regime. In the case $2\lambda_D<\lambda_{NN}$, the capture zones of the islands are delimited by the dotted lines, whereas for $2\lambda_D>\lambda_{NN}$ they coincide with the polygonal Wigner-Seitz cells. From reference [45].

- $2\lambda_D>\lambda_{NN}$. In this case, the diffusive areas of *NN* islands tend to overlap. Consequently, the capture zone of an island is determined by its local

environment and can be defined as the Wigner-Seitz cell. This implies that the *NN* domains grow in a correlated manner and thus leads to narrow and non-random spatial distributions. An equilibrium concentration of adsorbates between the islands develops during growth and ensures more compact island morphologies [34].

In summary, the formation of a round shaped island, with a regular structure that reflects the Wigner-Seitz cell form, may occur only if λ_D is larger than λ_{NN} because in such a way the adsorbates can move among the nucleation structures and this diffusion gives rise to a correct non-random spatial distribution. The formation of fractal structures occurs instead when λ_D is shorter then λ_{NN} and the adsorbates are blocked around a single island, growing in an uncorrelated manner.

According to this capture zone growth model it is possible to calculate the total amount of the grain boundaries per unit area. This value increases with increasing deposition rate. Thus, one of the most important aspects that we should consider is that with a supersonic molecular beam we can increase the adsorbate energy thereby increasing the value of λ_D.

[1] E. Reichmanis, H. Katz, C. Kloc and A. Maliakal, *Bell Labs Techn. J.*, 10 (2005) 87.

[2] G. Horowitz, *J. Mater. Res.,* 19 (2004) 1946.

[3] C.D. Dimitrakopoulos, P.R.L. Malenfant, *Adv. Mat.*, 14 (2002) 99.

[4] C.J. Brabec, N.S. Sariciftci, J.C. Hummelen, *Adv. Func. Mat.*, 11 (2001) 15.

[5] D.T. McQuade, A.E. Pullen, T.M. Swager, *Chem. Rev.*, 100 (2000) 2537.

[6] J. Fraxedas, *Adv. Mat.*, 14 (2002) 1603.

[7] G. Weiying, A. Kahn, *Org. Electr.*, 3 (2002) 53.

[8] Y. Shen, M.W. Klein, D.B. Jacobs, S.C. Scott, G.G. Malliaras, *Phys. Rev. Lett.*, 86 (2001) 3867.

[9] A. Kahn, N. Koch, W. Gao, *J. Pol. Science B*, 41 (2003) 2529

[10] H. Ishii, K. Sugiyama, E. Ito, K. Seki, *Adv. Mat.*, 11 (1999) 605.

[11] C.R. Kagan, A. Afzali, T.O. Graham, *Appl. Phys. Lett*., 86 (2005) 193505.

[12] R. Ruiz, D. Choudhary, B. Nickel, T. Toccoli, K.C. Chang, A.C. Mayer, P. Clancy, J.M. Blakely, R.L. Headrick, S. Iannotta, and G.G. Malliaras, *Chem. Mat.,* 16 (2004) 4497.

[13] W.R. Salaneck, K. Seki, A. Kahn, J.J. Pireaux, *Conjugated Polymer and Molecular Interfaces: Science and Technology for Photonic and Optoelectronic Applications*; Eds.; Marcel Dekker: New York, (2001).

[14] A.C. Mayer, A. Kazimirov and G.G. Malliaras, *Phys. Rev. Lett.*, 97 (2006) 105503.

[15] R. Campargue, *AIP Proceedings,* 762 (2005) 32.

[16] H. Ashkenas and F.S. Sherman, *Rarefied Gas Dynamics,* edited by J.A. Laurmann, Academic Press, 2 (1966) 84.

[17] *Atomic and Molecular Beams Methods,* edited by G. Scoles, Oxford University Press, (1988).

[18] R. Campargue, *J. Phys. Chem.,* 88 (1984) 4466.

[19] A. Kantrowitz and J. Grey, *Rev. Sci. Instrum.,* 22 (1951) 328.

[20] R.E. Smalley, B.L. Ramakrisma, D.H. Levy and L. Wharton, *J. Chem. Phys.,* 61 (1974) 4363.

[21] R.E. Smalley, D.H. Levy and L. Wharton, *J. Chem. Phys.,* 63 (1975) 4977.

[22] V. Aquilanti, D. Ascenzi, D. Cappelletti, F. Pirani, *J. Phys. Chem.*, 99 (1995) 13620.

[23] P. Milani and S. Iannotta, *Cluster Beam Synthesis of Nanostructured Materials*, Springer Ed. (1999).

[24] N. Karl, *Organic Semiconductors*, edited by O. Madelung, M. Schulz, and H. Weiss, Springer, Heidelberg (1985).

[25] G. Witte and C. Wöll, *J. Mater. Res.*, 19 (2004) 1889.

[26] B. Lewis, J. C. Anderson, *Nucleation and growth of thin films,* Accademic Press, New York (1978).

[27] J.A. Venables, G.D.T. Spiller, M. Hanbucken, *Rep. Progr. Phys.,* 47 (1984) 399.

[28] E. Bauer, *Z. Kristallogr*., 110 (1958) 372.

[29] K. Ploog, *Crystals: growth, properties and applications,* Springer-verlag, Berlin: (1980).

[30] S. Pratontep, M. Brinkmann, F. Nuesch, L. Zuppoli, *Phys. Rev. B,* 69 (2004) 165201.

[31] J. Last, A.C. Hiller, D.E. Hooks, J.B. Maxson, M. Ward*, Chem. Mater.,* 10 (1998) 422.

[32] J.G. Amar, F. Family, P.M. Lam, *Phys. Rev. B,* 50 (1994) 8781.

[33] M.C. Bartelt, J.W. Evans, *Phys. Rev. B,* 46 (1992) 12675.

[34] S. Pratontep, F. Nüesch, L. Zuppiroli and M. Brinkmann, *Phys. Rev. B,* 72 (2005) 085211.

[35] R. Ruiz, D. Choudhary, B. Nickel, T. Toccoli, K.C. Chang, A.C. Mayer, P. Clancy, J.M. Blakely, R. L. Headrick, S. Iannotta, and G.G. Malliaras, *Chem. Mat.,* 16 (2004) 4497.

[36] J.A. Venables, *Philos. Mag.*, 27 (1973) 693.

[37] R. Ruiz, N. Nickel, N. Koch, L. C. Feldman, R. F. Haglund, A. Kahn, F. Family, G. Scoles, *Phys. Rev. Lett.,* 91 (2003) 136102.

[38] P. Jensen, *Rev. Mod. Phys.,* 71 (1999) 1695.

[39] B. Stadlober, U. Haas, H. Maresch and A. Haase, *Phys. Rev. B*, 74 (2006) 165302.

[40] M. Drechsler, *Surface mobilities on Solid Materials,* Plenum Press New York (1983).

[41] G. Zinsmeis, *Vacuum*, 16 (1966) 529.

[42] R. Ruiz, B. Nickel, N. Koch, L.C. Feldman, R.F. Haglund, A. Kahn, G. Scoles, *Phys. Rev. B,* 67 (2003) 125406.

[43] P.A. Mulheran, J.A. Blackman, *Philos. Mag. Lett.,* 72 (1995) 55.

[44] P. Jensen, *Rev. Mod. Phys.*, 71 (1999) 1695.

[45] S. Pratontep, M. Brinkmann, F. Nuesch, L. Zuppoli, *Phys. Rev. B,* 69 (2004) 165201.

Chapter 5

Quasi-monocrystalline organic thin films

As mentioned in Chapter 4, small molecules are widely considered an interesting and viable way to understand the intrinsic properties and the processes involved in charge and energy transport in semiconductor conjugated polymers [1]. These are key issues in the fabrication of improved, reliable, and efficient devices for electronics, electro-optics and sensing applications [2]. In particular, oligothiophenes and pentacene are considered appealing compounds for their high degree of flexibility in ‘‘molecular engineering’’.

On the other hand major difficulties arise from the solid state packing of this class of molecules, where lack of control on structure, morphology and grain boundaries formation reduces the efficiency of the charge transport [3] limiting the performances of the organic devices [4].

The processes that control the thin films formation depend on the delicate equilibrium between molecule-molecule and molecule-surface interactions [5], which regulate the kind of growth (Frank van der Merwe, Volmer-Weber, Stransky-Krastanov; see Chapter 4) [6]. Nevertheless for the feeble nature of the forces involved in the formation of molecular solids and for the large number of polymorphs and orientations possible in the organics [7,8], it is hard to have a good control on growth.

The objective of our work is to improve the performances of devices, field effect transistor (FET) in particular, improving the control on the molecular assembling. This chapter will be divided in three parts, each concerning a different small conjugated molecules (α-quaterthiophene, α-sexithiophene and pentacene). Each section will show and discuss the experimental results obtained growing molecular thin films by SuMBD, exploiting the large potential con controlling the beam parameters (mainly the kinetic energy). We will demonstrate that usually, a better control of the source beam can not only give rise to a better morphology and higher degree

of order, but also improve the performance of organic devices fabricated with such ordered molecular thin films (e.g. OFETs).

5.1 Quaterthiophene thin film growth and devices[§]

Oligothiophenes are widely considered an interesting material for the realization of organic electronics for their high stability to oxidation processes [9]. Compared to other oligothiophenes, the performances of transistors based on alpha-quatertiophene are limited by its kind of growth on the typical materials used for device realization.

In this first section we will show that, via seeded supersonic beams, we can lead to a large improvement of both morphological and electrical properties of the quatertiophene (α-4T) film grown, through a better control of the initial state of the precursor in the vapour phase.

Using the high kinetic energy achievable in the supersonic beams, we can increase the dimensions of the grains and the coalescence of different islands, limiting the grain boundary formation. As consequence, the performance of the realized field effect transistors are enhanced of one order of magnitude.

5.1.1 Deposition and characterization techniques

Starting from these problematic and knowing the different works that have shown the importance of the state (in terms of translational, roto-vibrational and momentum) of the molecules in the processes involving their

[§] This section is based on T. Toccoli*, M. Tonezzer*, P. Bettotti, N. Coppedè, Silvia Larcheri, A. Pallaoro, L. Pavesi and S. Iannotta, **"Supersonic Molecular Beams Deposition of α-Quaterthiophene: Enhanced Growth Control and Devices Performances",** ***Organic Electronics,*** 10, 3 (2009) 521-526.

collision and the energy transfer with the surface [10], we will utilize a new approach to grow organic thin films, based on seeded supersonic beams [11].

As we have seen in previous chapter, supersonic beams give, indeed, the possibility to control the energetic state in terms of kinetic energy (E_k), momentum and internal degree of freedom of the impinging particles, by setting the initial working conditions such as the source nozzle dimensions, the temperature and pressure of the reservoir, etc. Seeding the vapors of the organic semiconductors in a lighter carrier gas (He in our experiments) that defines the conditions of the free jet expansion, makes it possible to control the final state of the seeded molecules [12].

During the supersonic expansion, the internal degrees of freedom of the molecules undergo a strong cooling process while the kinetic energy can be increased, from the few hundreds of meV of an effusive source, up to several eV by varying the degree of seeding [11]. For this reason, supersonic molecular beam deposition allows to surmount some of the difficulties intrinsic to the available techniques for the growth of films of organic molecules.

In this section we will show the results achieved in the growth of quaterthiophene on SiO_x/Si for the realization of organic field effect transistors by SuMBD. The α-4T molecules on this kind of surface typically present a 3D growth that strongly limits the performances in devices [13]. We will see that varying the E_k of the impinging molecules, it is possible to modify the growth of the α-4T, improving its morphology.

To verify the importance of E_k, we selected two different regimes of growth: the first one in which the seeded α-4T molecules have an average E_k of 3.0 eV and the second one in which their E_k is in the order of 7.5 eV. We have characterized the obtained films by atomic force microscopy to optimize the growth processes and to understand the effect of the kinetic energy of the impinging molecules on the thin film growth. We then used these films to fabricate FETs in bottom-gate top-contact configuration. Thus we are able to correlate the films morphology to the devices performance, showing that a higher control on the state of the molecules in the beam can improve the characteristic of our transistors.

The experimental apparatus used to realize the seeded supersonic beams of α-4T essentially consists of two chambers differentially pumped to

high vacuum, a hyperthermal source placed in the first chamber and an ultra high vacuum deposition chamber where the sample holder is placed. Behind the sample holder, a time of flight mass spectrometer (ToF-MS) is connected to the deposition apparatus, and used to verify the purity of the materials, to determine the energetic properties of the seeded molecules, and to precisely determine the molecular flux.

The ionization of the molecules/atoms in the beam is obtained by the use of the 4^{th} harmonic of a Nd::YAG laser (266 nm/4.66 eV), which photo-ionizes part of the molecular beam just behind the sample holder, in the middle of a series of electronic optics. The α-4T was grown on highly doped silicon (n^{++}) wafers covered with 50 nm thermally grown silicon oxide, cleaned in hot (325 K) isopropylic alcohol, treated with ozone for 30 min, and then outgassed at 455 K for 12 hours in ultra high vacuum inside the home-build apparatus. All the depositions were performed at room temperature with a flux of about 0.2 nm/min.

5.1.2 Organic thin films morphology

Topographic characterization of the different films has been performed by AFM microscopy in air, using a Smena SFC050 scanning head by NT-MDT. Depending on the sample, measurements have been carried out in semi-contact mode AFM (using NSG11 silicon cantilevers by NT-MDT) or in contact mode (using CSG10 Au-coated silicon cantilever by NT-MDT).

Figure 5.1 shows the typical morphology of our films grown on SiO_x/Si using 3.0 eV of E_k. In particular, Figure 5.1a reports a large area (10x10μm^2) where it is possible to recognize the kind of growth of the films. Two aspects are clear: the 3D (Volmer-Weber, see Chapter 4, page 93) growth and the crystallinity of the films. The first one is recognizable from the aspect of the grains that are developed in height presenting sharp walls (sharp color change in Z scale).

This is more evident when the thin films growth is stopped with a nominal thickness lower than a monolayer (ML). In this case, the islands

produced from the nucleation of the α-quaterthiophene molecules, typically present a height of about 5 nm (about 3 MLs) leaving uncovered most of the underneath surface. When increasing the coverage, we observe both a growing of the islands surface and height.

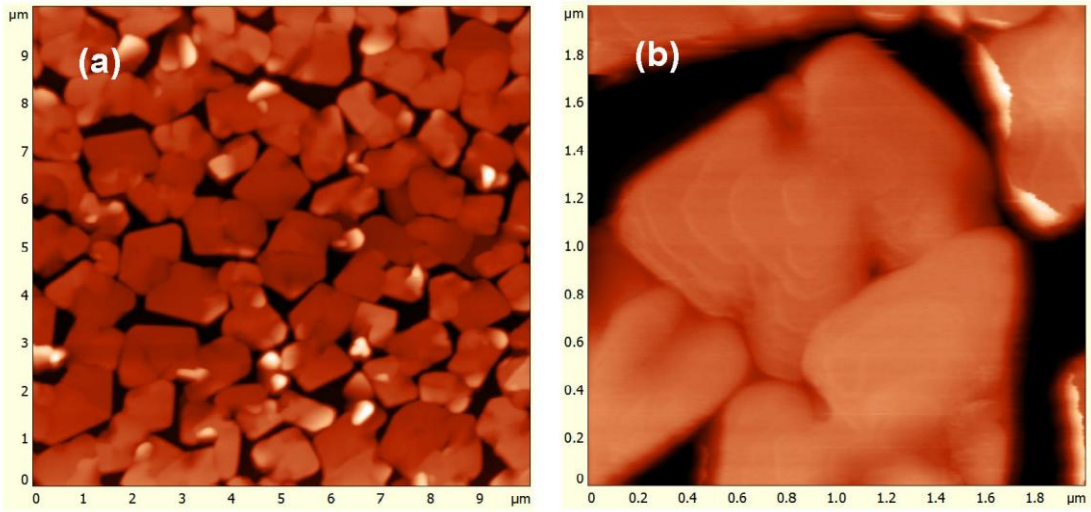

Figure 5.1: AFM topographic images of a film grown on SiO_x/Si with impinging molecules having 3.0eV of E_k. (a) Image 10×10µm^2 acquired in semi-contact mode; (b) detail of a grain (2×2µm^2) acquired in contact mode.

The coalescence of the islands starts when the nominal thickness of the films is of about 50 nm (clearly much larger than one monolayer). In these conditions the average islands height is about 100 nm, indicating that ~50% of the surface is uncovered by the molecules. Growing more, the islands start to join up in a ¨polycrystalline¨ film, whose thickness is already several layers (Figure 5.1a).

This growth results to be different if compared to the case of pentacene grown by SuMBD in which, in similar conditions, we observe the starting formation of islands of one molecule in height and their coalescence without the formation of the second layer [14]. For pentacene films about 50 nm thick, we find 1-2 µm^2 terraced grains that completely cover the surface [15].

The shape of the grains gives us the information relative to the crystallinity of films grown at this kinetic energy. In fact, the islands present a polygonal form typical of ordered structure (crystals), with an average grain size of 2-3 μm^2 and no preferential direction of growth. In this situation the main problem in the FET fabrication is related to the poor interconnection between the different islands and the resulting need to increase the film thickness. This limits the device's performances.

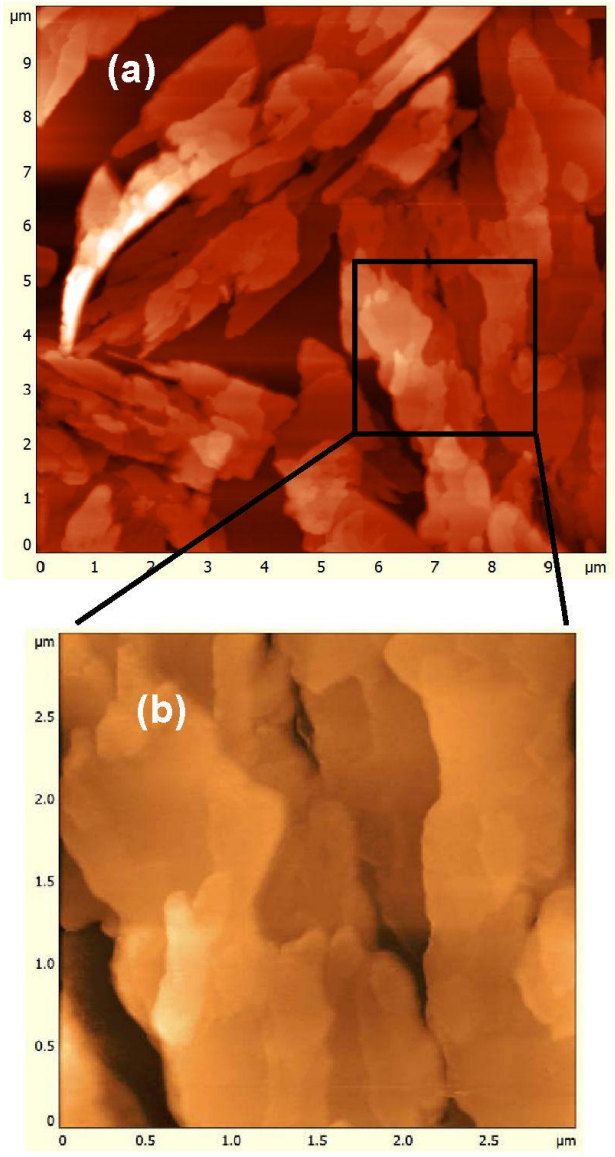

Figure 5.2: AFM topographic images of a film grown with impinging molecules having E_k = 7.5eV. (a) Image 10×10μm^2; (b) zoom on a few grains (region indicated by the black square, 3×3μm^2). Both images have been acquired in contact mode AFM.

If we compare this kind of morphology with the morphology reported in literature growing the α-4T molecules on the same surface in similar conditions [13,16], we notice that in our case the grains seem to be more regular and with a larger size. This effect is most likely related to the increased energy of the impinging molecules (3.0 eV in respect to about 150 meV of a common thermal evaporation) that, in our present case, permits their better rearrangement.

The growth is completely different in the case of impinging molecules having E_k = 7.5 eV. Figure 5.2 shows the typical morphology obtained in this case. The islands present really different shapes and dimensions. On the large area (Figure 5.2a) we observe that typically the films are formed by elongated terraced islands with dimensions in some cases larger than 10 μm. At the same time, the ratio between the covered surface and the islands' height increases, thus realizing more uniform films with less grain boundaries.

The high kinetic energy used in this case is able to partially overcome the low affinity between the α-4T molecules and the surface, leading to formation of such more regular structures. Also in this case, starting the characterization from the sub-monolayer growth, we observe the difficulty of the α-quaterthiophene molecules to cover completely the SiO_x/Si surface.

Going into detail (Figure 5.2b, zoom) we observe that the grains show the terraced structure typical of a layered morphology with steps of one molecule in height. With respect to the steps observable on top of the islands in the low E_k films (Figure 5.1b), the lateral size of these terraces present a larger surface. This indicates a better rearrangement of the molecules giving rise to a more ordered structure.

This kind of growth indicates that, by increasing the kinetic energy of the impinging molecules, we are able to modify the preferred growth of the α-4T molecules, thus having the possibility to grow films with a prevalent layer plus island growth. This gives the possibility to decrease the number of grain boundaries that, for devices realization, is an important point in order to improve their performances.

We should also stress here that the first few monolayers close to the oxide substrate are the most important ones for the fabrication of organic devices. Consequently, the higher order coming from a layer plus island

(instead of 3D) growth, is even more important in terms of electronic and gas sensing applications.

Furthermore, to confirm that a higher energy deposition doesn't change the phase of the material grown, we have made some X-ray diffraction analysis on the samples grown at different energies. Figure 5.3 shows the XRD spectra of two samples grown at low (black) and high (red) kinetic energy, respectively 3.0 eV and 7.5 eV. Both spectra show the same peak positions: 5.8°, 11.6°, 17.5°, 23.4°, 35.3°, 41.5° and 47.7°.

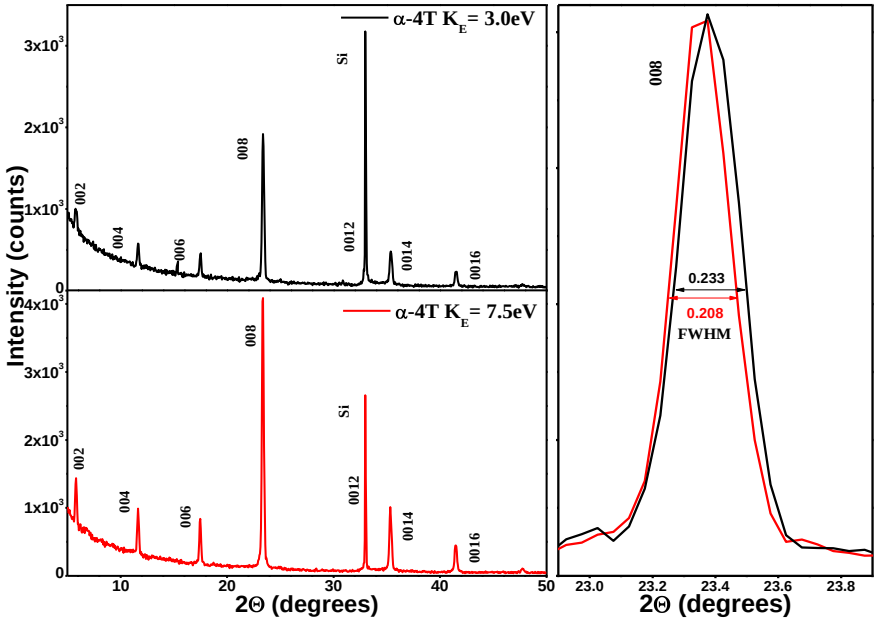

Figure 5.3: XRD spectra of two samples grown at 3.0 eV (top left, black) and 7.5 eV (bottom left, red) respectively. At right a zoom on the 008 reflection, comparing in detail the width of the peak in both spectra.

They confirm in both cases the low temperature phase of α-quaterthiophene [17]. At right there's a detail of the 008 reflection, rescaled to make comparable the difference in the FWHM of the two spectra. The full width at half maximum is lower (0.208° against 0.233°) in the spectrum of the sample deposited at high energy, and this agrees with the AFM images, reflecting an improved order of the film.

5.1.3 Organic field effect transistors

We have fabricated a series of bottom-gate top-contact field effect transistors to confirm that the growth by SuMBD gives the possibility to obtain films with better optical [18], morphological and electrical characteristics, due to the control achievable on the energetic state of the precursor and the consequent higher molecular order. The organic active devices are 30 μm long and 200 μm wide, and have been realized on the thickest films previously characterized by AFM, by depositing the 30 nm gold contacts (source and drain) through a shadow mask. The highly doped silicon substrate, etched on a sample corner, has been used as bottom-gate contact.

The electrical characterization was performed in a probe station equipped with a Agilent 4156 C source meter. Assembling devices on films previously characterized by AFM could limit their performances, but our objective here is just the correlation of the electrical performances with the growth conditions and the morphological properties and not the best performance achievable.

Figure 5.4 shows the typical transfer characteristics in saturation (Fig. 5.4a) and in the linear (Fig. 5.4b) regimes of our α-quaterthiophene FET devices in the case of films grown at low E_k (orange line) and in the case of films grown at high E_k (blue line). From these curves, we can calculate the electrical properties that characterize our devices [19].

In particular, in the linear regime, the drain current I_D can be written as:

$$I_D = \frac{WC_j\mu_{FE}}{L}\left(V_G - V_T - \frac{V_D}{2}\right)V_D \qquad (5.1)$$

where L is the channel length and W the channel width, C_j is the capacitance for unit area of the dielectric, V_T is the threshold voltage, and μ_{FE} is the field effect mobility. We can therefore calculate the mobility in the linear regime from the slope of the curve obtained by plotting I_D vs V_G for sufficient low V_D. The threshold voltage in this case is easily determined as the intercept

(I_D = 0) for the maximum slope of I_D. In the saturation regime, the drain current saturates and can be modeled by the following equation:

$$I_D = \frac{WC_j \mu_{FE}}{2L}(V_G - V_T)^2 \qquad (2)$$

In saturation regime, μ_{FE} can be calculated from the slope of the plot of $\sqrt{|I_D|}$ versus V_G, and, in the same way, V_T can be calculated as the intercept (I_D=0) of the maximum slope of $\sqrt{|I_D|}$ versus V_G.

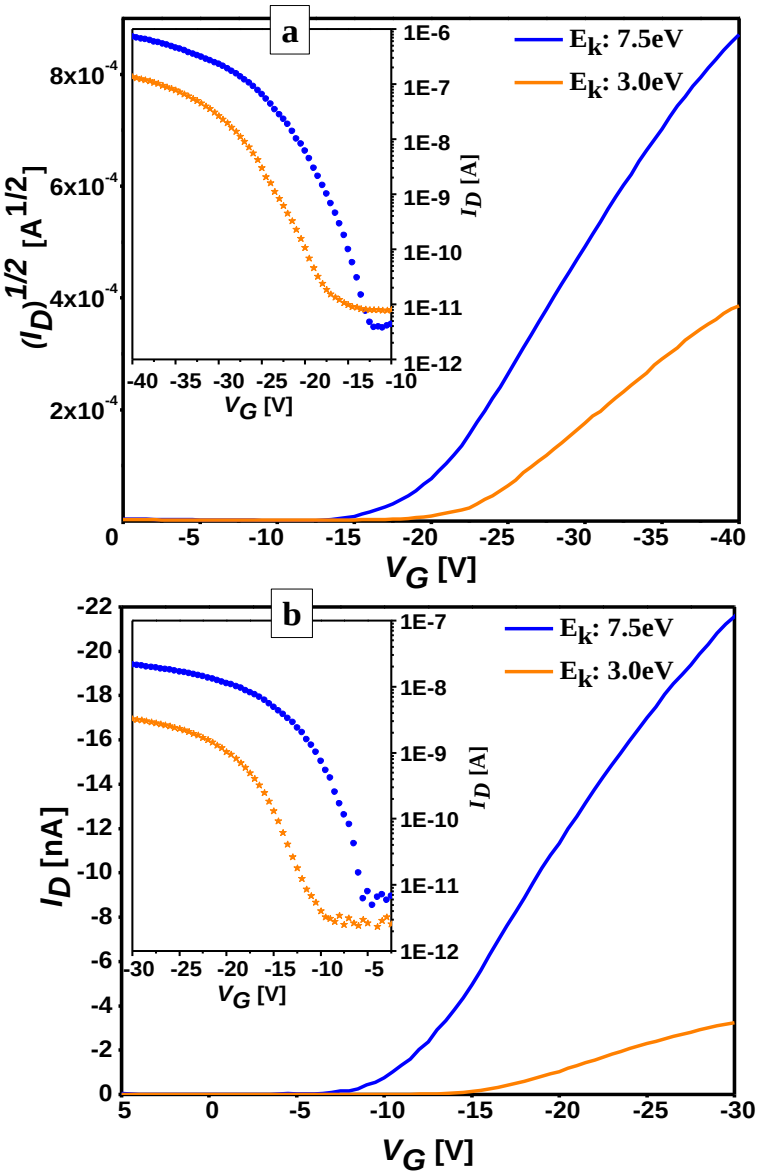

Figure 5.4: Transfer curves of a low E_k grown sample (orange) and a high E_k grown sample (blue). The curves are compared both in a) saturate (V_D

= -41 V) and b) linear regime (V_D = -1 V). The insets shows the transconductance of the same devices in both regimes.

	E_k = 3.0 eV		E_k = 7.5 eV	
	V_D = -1 V	V_D = -41 V	V_D = -1 V	V_D = -41 V
V_T [V]	-15.9	-22.5	-11.2	-16.0
I_{ON}/I_{OFF}	$1.1 \cdot 10^3$	$1.6 \cdot 10^4$	$8 \cdot 10^4$	$1.8 \cdot 10^5$
$S_T Slope$ [V·dec^{-1}]	2.0	2.5	0.98	1.66
μ [cm^2·V^{-1}·s^{-1}]	$0.75 \cdot 10^{-3}$	$1.7 \cdot 10^{-3}$	$3.8 \cdot 10^{-3}$	$1.22 \cdot 10^{-2}$

Table 5.1: Main working parameters of the devices fabricated. The first two columns show the low kinetic energy sample values, while the last two columns refer to the high kinetic energy sample.

From the semilogarithmic plot of I_D versus V_G (transconductance) we extract the I_{on} over I_{off} ratio and the subthreshold slope. The typical values obtained for our devices, grown at different kinetic energy values, are reported in Table 5.1.

Figure 5.4 and Table 5.1 give us the information about the strong impact of the growth conditions inside the source beam on the performances of the devices. Indeed field effect transistors fabricated with thin films grown at low E_k have characteristics in terms of mobility, threshold voltage, I_{on} / I_{off} ratio and subthreshold slope comparable with the majority of α-4T transistors reported in literature [20].

This is a first good result, considering the absence of any optimization in our fabrication process steps. However, if we compare these results with those obtained for the growth at 7.5 eV, we see the great advantage given by the growth method that we have developed. The extracted mobility for these devices (about $1.2 \cdot 10^{-2}$ V cm^{-1} s^{-1}) is about one order of magnitude larger with

respect to the first one and the performances of these transistors are better than the best ones reported in literature [21,22,23].

To better understand if the enhanced mobility is coming only by the improved order (wider grain size) of the film grown, we plotted in Figure 5.5 the field effect mobilities found for several samples as a function of the average grain size calculated from their AFM images. It can be seen that they follow a linear dependence, showing that the improved transport properties of the film grown at high kinetic energy comes from a reduced grain boundary.

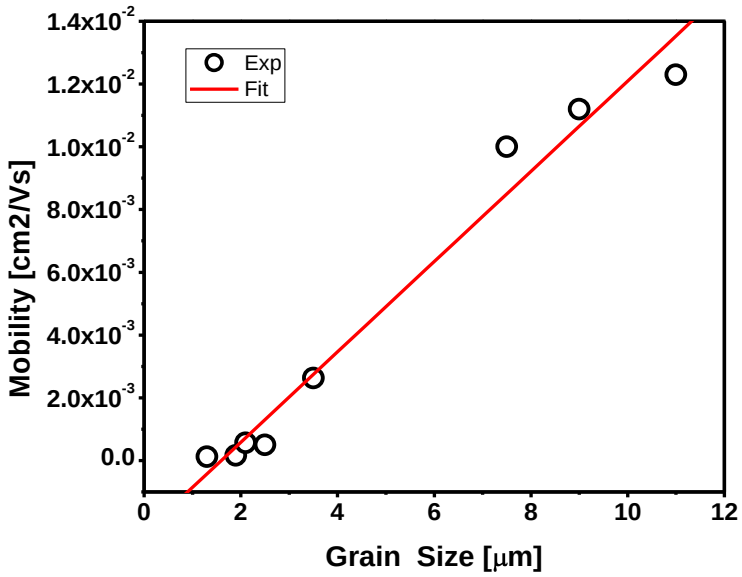

Figure 5.5: Graph reporting the field effect mobility of some devices as a function of the grain size of the film they were fabricated on. It is quite clear the linear dependency.

As a conclusion of this section, we have shown that the growth dynamics of organic thin films starting from the vapour phase are governed by a delicate equilibrium between the molecule/molecule and the molecule/surface interactions and for this reason are also strongly dependent on the energetic state of the precursors. This can be obtained by using the supersonic beam deposition technique, thus improving the organic material growth.

The key factor is the high kinetic energy achievable with this technique (up to 15 eV for the α-quaterthiophene seeded in hydrogen) by the impinging molecules. When the molecules collide with the surface, they can release this surplus of energy by increasing the surface mobility and giving rise to a sort of local annealing that can rearrange the molecular order and increase the islands size limiting the grain boundaries formation.

The final effect, as we have shown for the α-4T, is an increase in grain size while increasing the kinetic energy and an enhancement of the order inside the grain. The better morphology in terms of order and limiting of grain boundaries gives also the possibility to grow devices with better performances.

The electrical characteristics of our FETs obtained at 3.0 eV are comparable to the ones of transistors realized with the same materials but with different techniques. However, in the case of transistors obtained on films grown at 7.5 eV the performances are better than the state of the art, even without using any optimization process.

5.2 Sexithiophene thin film growth and devices[**]

In this section we will demonstrate again, using α-sexithiophene (α-6T) small molecule (a widely recognized reference molecule in the field of organic electronics [24]), the unprecedented control on the different states of the nucleation process and on the final properties of both the films structure and morphology obtainable with SuMBD. We will finally show the effective ability to improve device performance in a field effect transistor standard (bottom-gate top-contacts) architecture.

This is achieved by exploring the role of the initial state of the impinging molecules (kinetic energy in particular) in determining the film formation and device behaviour on substrates with different surface wettability and temperature. Along this section we will focus on the sub-monolayer growth of

[**] This section is based on M. Tonezzer*, T. Toccoli, E. Rigo, P. Bettotti and S. Iannotta, **"α-Sexithiophene growth by SuMBD: Enhanced Growth Control and Devices Performances",** submitted to ***Advanced Functional Materials.***

α-sexithiophene islands trying to develop a model which can explain how it's affected by the different deposition parameters.

5.2.1 Surface nucleation and sub-monolayer growth

The role of kinetic energy on the molecular assembling is investigated following the early stages of the growth on pristine SiOx/Si and UV/O_3 treated SiOx/Si, at room (25°C) and 90°C substrate temperatures, in order to better compare with the best results in literature. The samples are then studied ex situ, by atomic force microscopy, to characterize the growth evolution at different deposition times (5, 10 and 40 minutes).

We focused our investigations on two different values of the molecular kinetic energy in the beam: about 13.1eV (high E_K, from now E_{KH}) and 2.2 eV (low E_K, in the following E_{KL}). The two different kinetic energies are achieved by seeding in two different carrier gases the α-6T molecules: He for E_{KH} and Ar for E_{KL}. This is a nice way to produce beams characterized by a large difference in E_K keeping the roto-vibrational distributions of the molecules quite similar [25]. We also maintain the flux of the molecules arriving onto the surface constant in all the experiments.

Figure 5.6 shows typical AFM micrographs observed for samples grown at room temperature**.** Images follow the film formation with snapshots taken at 5, 10 and 40 minutes of beam flux exposure. The first two rows of the top half of the figure show the α-T6 islands grown on a hydrophilic substrate (less than 10° contact angle) at E_{KL} and E_{KH} respectively. The third and the fourth rows of the bottom part of Figure 5.6 show the same time evolution steps of growth on a slightly hydrophobic surface (about 65° contact angle) at E_{KL} and E_{KH} respectively.

In all the investigated cases we observe an island profile step of 2.4 ± 0.1 nm that is in good agreement with literature for vertically standing α-T6 molecules [26]. The evolution of the islands morphology is clearly visible in the typical shape of the islands (see insets in Figure 5.6) and is quantified and discussed in the following.

We focussed the analysis on the evolution of growth rate, island density and fractal dimension; the definitions of the related procedures are reported in the experimental section.

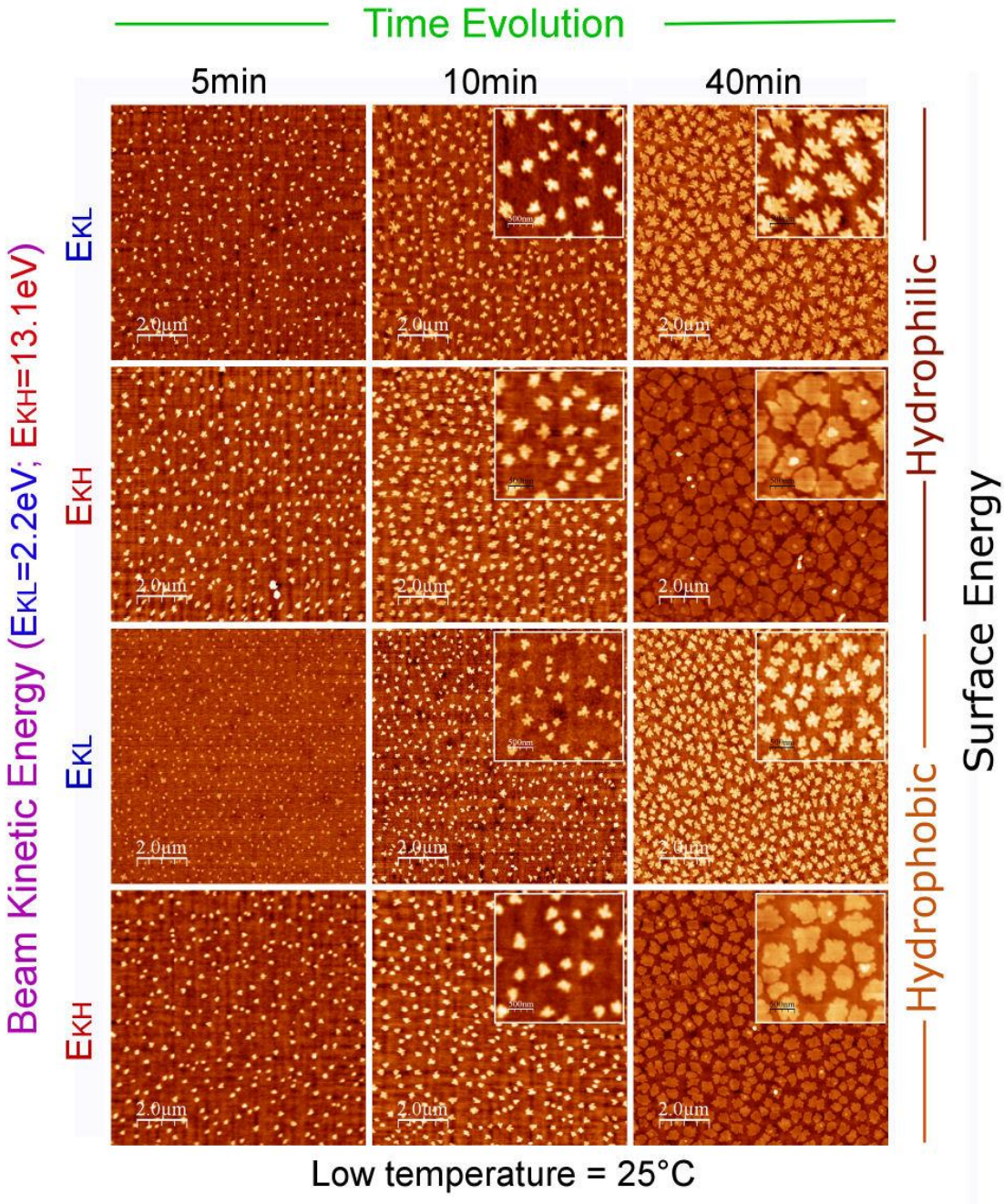

Figure 5.6: AFM pictures after 5, 10 and 40 minutes of α-6T sub-monolayer films grown at room temperature (25 °C) on hydrophilic (first and second row) and hydrophobic (third and fourth row) with low kinetic energy (first and third row) and high kinetic energy (second and fourth row).

The statistical analysis of the AFM data on a large number of micrographs of the type shown in Figure 5.6, is reported in Figure 5.7. A first important observation is that the molecule adsorption rate depends on both surface properties and the initial energy state of the molecules. In particular, we measure a higher absorption probability on a hydrophilic surface than on a hydrophobic surface in agreement with literature [27].

On the other hand, we also observe an enhanced growth rate when increasing the kinetic energy of the impinging molecules from E_{KL} to E_{KH} (Figure 5.7a). This energy dependence is typical of an activated process where the higher energy favours the access to extra adsorption sites on the surface.

This can be rationalized considering that during the collision the molecules impinging the surface can relax their kinetic energy due to the coupling to both the surface phonons and the roto-vibrational molecular degrees of freedom. In this complex series of events the available energy could also favour new pathways of adsorption otherwise not accessible because of energy barriers.

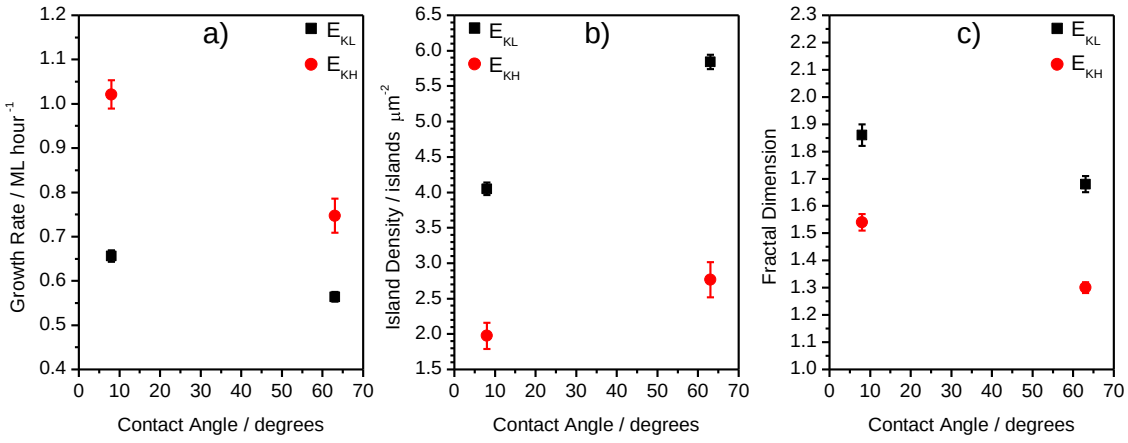

Figure 5.7: a) Growth rate, b) island density and c) fractal dimension of the samples grown at room temperature, on both hydrophilic and hydrophobic substrates. Red circles refer to samples grown with high kinetic energy, while black squares refer to samples grown with low kinetic energy.

This is consistent with the observation that at E_{KH} the overall growth rate is larger on both type of surface energies explored. On the other hand, the higher growth rates take place together with smaller density of islands (as shown in Figure 5.7b) that is an indication that only the islands grown on the more stable sites of absorption survive during the growth at E_{KH}, and the ones surviving are also more effective for further molecular aggregation.

In fact, when growing at E_{KH} the island density is much lower than for E_{KL}, with a factor ranging from 1.5 for an UV/O_3 treated surface (with a contact angle lower than 10°) up to 2.3 for the untreated surface (with a contact angle of about 65°). It is quite reasonable that the two different surface treatments generate, together with different contact angles, also a distribution in adsorption sites with different energy wells and barriers [26].

This is consistent with the observation (Figure 5.7b) that at E_{KL} there is a global increasing of the island density that is lively due to the nucleation around shallow adsorption sites. This effect is much more consistent for the untreated surface. At high kinetic energy the shallower sites do not stabilize the nucleation of new islands, so that the difference observed in the density of islands depending on the surface treatment is less significant (see Figures 5.6 and 5.7b).

Another key role of the kinetic energy of the impinging molecules concerns the observed control on the molecular assembling on the surface, giving rise to different island morphologies (see insets in Figure 5.6). We quantified this effect by using the fractal dimension D [28] using the following relationship $P = \mu S^{D/2}$ where S and P are respectively the surface and perimeter of the island and μ is a constant.

Figure 5.7c shows the dependence of the fractal dimension for deposition at E_{KH} and E_{KL} on different surface energies. First of all we notice that in general on non treated surfaces (with 65° as contact angle), we obtain a smaller fractal dimension than on UV/O_3 treated surfaces (with less than 10° as contact angle). The effect of surface energy on fractal dimension has been already observed by conventional OMBD [29] and correlated to the enhanced surface mobility of the molecules for hydrophobic surfaces [26].

We here achieve the evidence that the SuMBD ability to tune the kinetic energy of the impinging molecules allows to change independently the

surface mobility. The results of Figure 5.7c demonstrate that the final effect is a strong reduction of fractal dimension for higher kinetic energies and that un unprecedented low fractal dimension could be obtained even for hydrophilic surfaces at room temperature.

When compared to conventional OMBD, our E_{KL} islands grown at room temperature result to be comparable in fractal dimension to the best results reported on hydrophilic surfaces for sub-monolayer growth at 120°C [26]. At E_{KH} we achieved unprecedented low fractal dimension with values as low as 1.2, overcoming limits of the state of art that were considered intrinsic and hence not surmountable.

This is due to a dynamics where the molecules with E_{KH} sample many adsorption sites on the island perimeter before sticking, improving the minimization of the free energy. At lower contact angle there is a hindering of the molecular diffusion on the surface that reduces such effect as the fractal dimension of Figure 5.2b confirms.

In this framework the effect of the kinetic energy could be manifold. Apart from the above mentioned effect of an increase of mobility on the bare substrate surface, we should consider the effect on the molecules impinging on the already forming molecular islands. In fact the molecular kinetic energy can overcome the two most relevant barriers that limit the so called layer by layer growth.

The first one is the so called Schwoebel barrier that has been estimated to be in the order of 0.67eV for an organic semiconductor such as pentacene [30, 31]. The second one comes from the activation energy to incorporate the impinging molecules directly into the molecular layer at the collision site.

This process induces an overall molecular rearrangement of the islands and occurs only if the incoming energy is large enough. The probability of such events has been estimated to become sizeable for kinetic energy larger than 2eV in the case of pentacene molecules [32].

Even though our experiments could not discriminate such different mechanisms, our result show, for the first time, a clear evidence that both types of threshold could be overcome by the kinetic energy of the incident molecules. In fact the second layer is not being formed even at room

temperature until the first one is almost complete. The observed dependence of fractal dimension on kinetic energy is very likely due to the combination and possibly cooperation of the mechanisms discussed before.

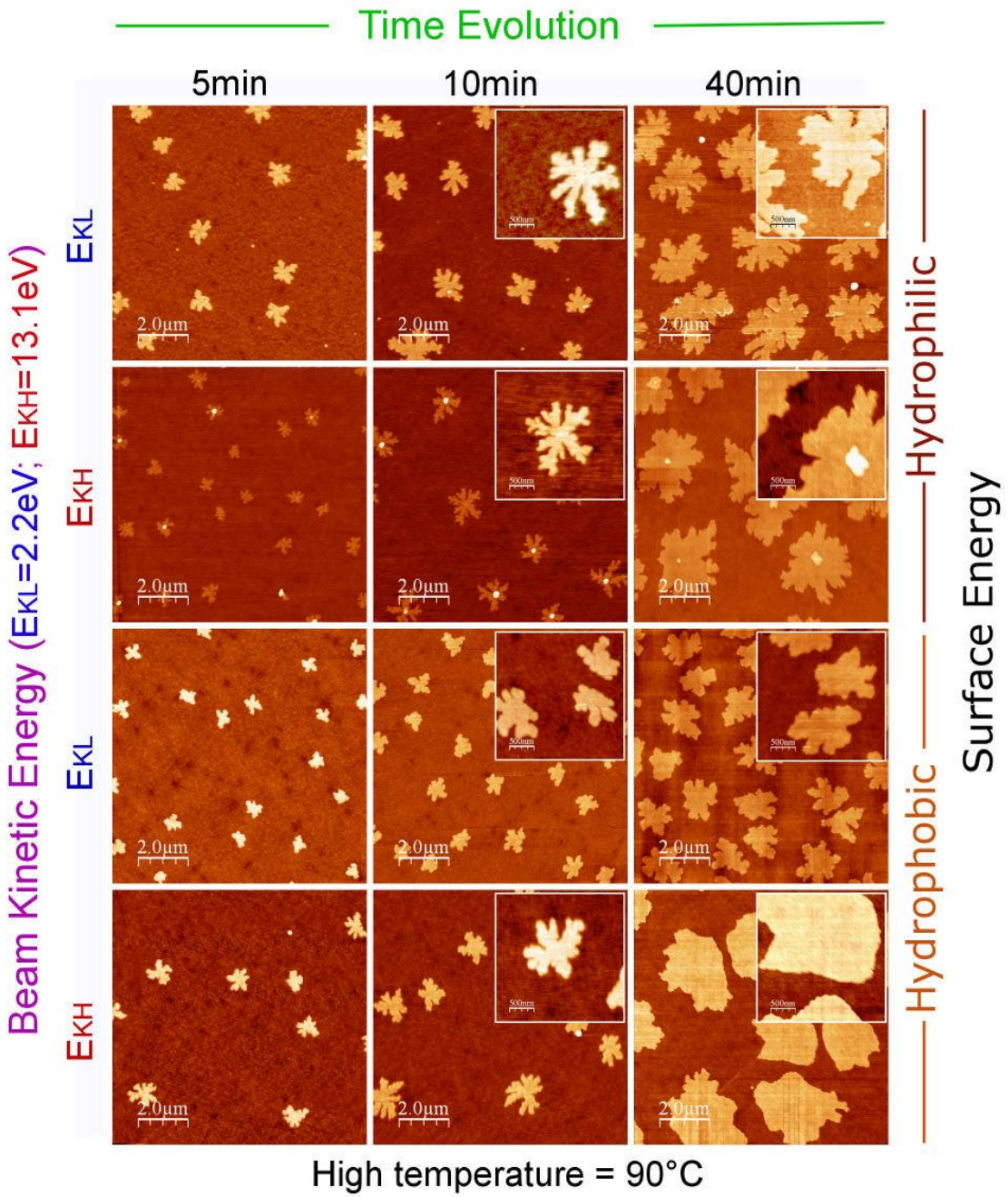

I

Figure 5.8: AFM pictures after 5, 10 and 40 minutes of α-6T sub-monolayer films grown at high temperature (90°C) on hydrophilic (first and second row) and hydrophobic (third and fourth row) with low kinetic energy (first and third row) and high kinetic energy (second and fourth row).

In fact in all these a thermalization of the molecular incoming energy within the island should be involved. Such a process would induce a rearrangement of the molecules towards a more ordered configuration where the more stable sites at the border of the islands become favoured.

On the other hand the molecules laying at the periphery of the island on sites with lower coordination would move, driven by the achievable energy, to sites with higher coordination: a process that statistically should give rise to smoother island borders and hence to lower fractal dimension.

Following the same scheme of RT films, Figure 5.8 reports the AFM micrographs of depositions on substrates at 90°C. The first two rows compare the sub-monolayer growth of α-6T on hydrophilic substrates for E_{KL} (first row) and E_{KH} (second row) deposition. Third and fourth rows report the results on the slightly hydrophobic substrates. The observed islands height is the same (2.4±0.1nm) observed for room temperature samples and hence the molecules assemble in vertical position.

The first major effect of the substrate high temperature is on the growth rate that significantly decreases (Figure 5.9a). This effect is stronger for E_{KH} growth rate, that becomes similar to the E_{KL} one.

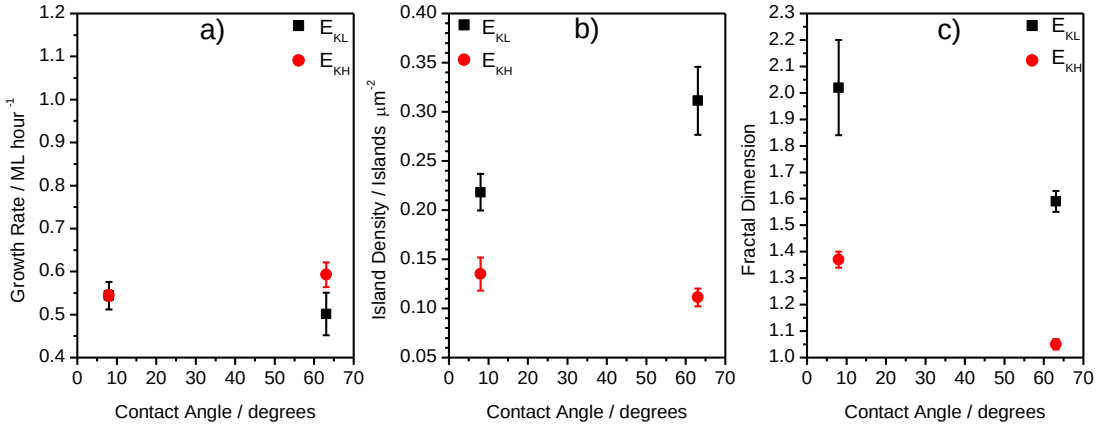

Figure 5.9: a) Growth rate, b) island density and c) fractal dimension of the samples grown at high temperature, on both hydrophilic and hydrophobic substrates. Red circles refer to samples grown with high kinetic energy, while black squares refer to samples grown with low kinetic energy.

On the other hand we observe a generalized increase of the island size with respect to the room temperature case, giving rise to a much lower (about a factor 20) island density as reported in Figure 5.9b.

The effect of the surface phonons is therefore quite strong in particular on the growth rate and could be rationalized within the mechanism discussed above. Higher surface temperature implies larger displacement of surface atoms perpendicular to the surface [33] that act as efficient scattering centres for the incoming molecules, reducing the overall sticking.

On the other hand it has been shown that collisions on hotter surfaces give rise to an increase uptake of perpendicular momentum in the collision [34]. Both such effects are expected to be more effective in the E_{KH} case and hence in causing a much larger reduction of growth rate.

On the other hand the effect of the kinetic energy on the island density remains very relevant on both surface energies, even at 90°C. The observation that the island growth, structure and morphology is strongly influenced by the E_K is also confirmed at 90°C by the fractal analysis that we carried out, which is shown in Figure 5.9c.

In the comparison with the data at room temperature we observe a very similar trend with a possible enhancement of the differences between E_{KH} and E_{KL} growth. At E_{KH} on non treated surfaces (contact angle of about 65°) we obtain the lower fractal dimension close to 1.

We have observed that changing the kinetic energy of the impinging molecules has a strong effect on the minimization of the surface energy, which is not simply achievable by increasing the global amount of available energy on the surface.

Controlling the precursor energetic state of molecules is indeed possible to act selectively on the activation of several mechanisms that lead to a better quality molecular assembling.

5.2.2 Thicker films morphology

To complete the analysis of the effect of the state of the impinging molecules on the growth, we have also characterized thicker films (nominally 20-30 nm) of α-6T grown on SiOx/Si^{n++} hydrophobic substrates. This surface was preferred because in the early stage growth we saw better morphology (lower fractal dimension and larger grain size) respect to films grown on hydrophilic surfaces.

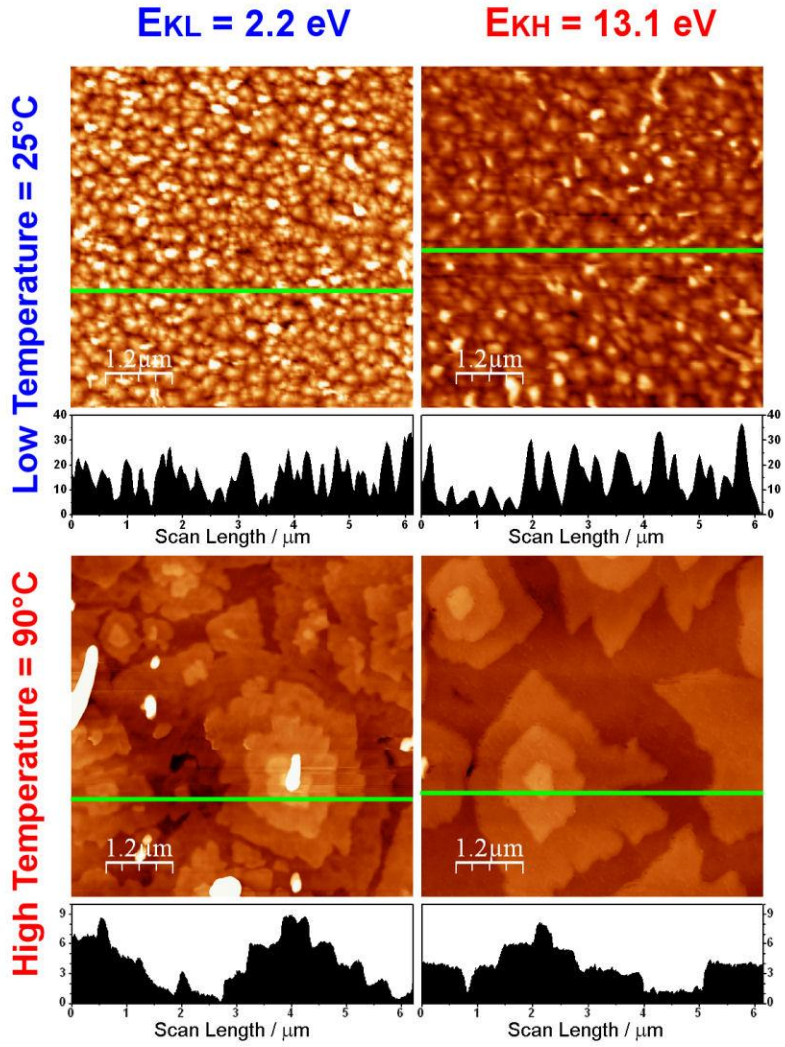

Figure 5.10: AFM pictures and profile scans of thicker films grown on hydrophobic substrates (low kinetic energy on the left and high kinetic energy on the right). First row refers to low temperature (25°C) growth and second row refers to high deposition temperature (90°C).

Figure 5.10 shows AFM characterizations (top view and cross section) with the comparison between multilayered films grown at 25°C and 90°C of substrate temperature and with high and low kinetic energy of the impinging molecules. The samples grown at room temperature (Figures 5.10a and 5.10b) show a typical polycrystalline morphology that compares well with the one obtained for the first layer.

In fact, the grain density is very close to the result obtained at RT for the sub-monolayer films, in both low and high kinetic energy cases, confirming that the thick film grow this highly influenced by the first layer morphology [35].

On the other hand, films deposited at 90°C (Figure 5.10c and 5.10d at low and high kinetic energy respectively) show a very homogeneous coverage with flat terraced islands and well-defined steps. In more detail few dark regions in Figure 5.10c, where the substrate surface is visible, confirm a not-completed coalescence of lower layers that is not present in the high E_K films Figure 5.10d.

5.2.3 Electrical characterization of devices

The knowledge of morphology in the early growth stages and in thicker films was an important step for an optimum correlation of the electric properties of devices with the investigated growth parameters. Here we study how the kinetic energy of the impinging molecules influence the electrical properties of the α-6T films, grown in the conditions reported in the previous section. The devices were realized in a bottom gate - top contact configuration (Figure 5.11) by depositing source and drain gold contacts by physical vapour deposition through a shadow mask. The transfer curve in linear and in saturation regime was used to obtain the electrical properties of the films.

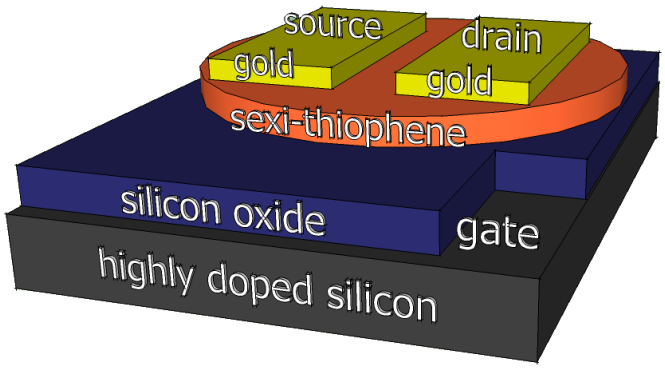

Figure 5.11: Sketch of the bottom-gate top-contacts OFET device.

The electrical parameters defining the performances of the devices were then calculated from the drain current using the usual relation of thin film FET [19]

$$I_D = \frac{WC_j\mu_{FE}}{L}\left(V_G - V_T - \frac{V_D}{2}\right)V_D \qquad (5.1)$$

for the linear regime, where L is the channel length and W the channel width, C_j is the capacitance for unit area of the dielectric, V_G the gate voltage, V_T is the threshold voltage, and μ_{FE} is the field effect mobility.

We can calculate the mobility in this regime from the slope of the curve obtained by plotting I_D vs V_G for sufficient low V_D [36].

In the saturation regime the drain current can be obtained from the equation [19]:

$$I_D = \frac{WC_j\mu_{FE}}{2L}\left(V_G - V_T\right)^2 \qquad (5.2)$$

In this regime, μ_{FE} can be calculated from the slope of $\sqrt{|I_D|}$ versus V_G. The device transfer characterization in both regimes permits also to extract, from the semi-logarithmic plot of I_D versus V_G, the I_{ON} over I_{OFF} ratio and the sub-threshold slope.

The summary of the results achieved from the electrical characterization of the devices are reported in Table 5.2. Here we see the strong impact of the growth conditions on the performances of the devices. The average performance of samples grown in different conditions are compared.

When depositing at low E_K on substrates at room temperature we observed very low drain currents, in this range the leakage currents are not negligible anymore and the measure becomes unreliable. For this reason we do not report the results.

	Room Temperature		**High Temperature (90 °C)**			
	High E_K (13.1eV)		**Low E_K (2.2 eV)**		**High E_K (13.1eV)**	
	Linear	Saturation	Linear	Saturation	Linear	Saturation
	V_D = -1 V	V_D = -71 V	V_D = -1 V	V_D = -70 V	V_D = -1 V	V_D = -70 V
V_T [V]	- 6.8 ± 0.3	- 7.1 ± 0.4	- 8.1 ± 0.5	- 7.2 ± 0.3	-6.4 ± 0.1	-6.2 ± 0.2
I_{ON}/I_{OFF}	$7.2 \pm 0.8 \cdot 10^2$	$5.6 \pm 0.8 \cdot 10^4$	$4.5 \pm 1.7 \cdot 10^3$	$5.0 \pm 0.9 \cdot 10^4$	$8.4 \pm 1.2 \cdot 10^3$	$5.3 \pm 0.2 \cdot 10^4$
S_TSlope $[V \cdot dec^{-1}]$	1.7 ± 0.7	0.9 ± 0.6	1.4 ± 0.2	1.9 ± 0.9	1.5 ± 0.4	1.0 ± 0.1
μ $[cm^2 \cdot V^{-1} \cdot s^{-1}]$	4.5 ± 1.1 $\cdot 10^{-2}$	5.6 ± 0.7 $\cdot 10^{-2}$	6.25 ± 0.42 $\cdot 10^{-3}$	6.72 ± 0.37 $\cdot 10^{-3}$	1.42 ± 0.02 $\cdot 10^{-1}$	1.51 ± 0.09 $\cdot 10^{-1}$

Table 5.2. Average device performance of field effect transistors fabricated with samples grown on hydrophobic substrates in different conditions.

On the contrary, the drain currents obtained in the other investigated cases were not affected by the leakage currents which are typically of the order of $1x10^{-11}$A. Looking at FETs grown at room temperature and with high E_K we obtain characteristics in terms of mobility, threshold voltage, I_{ON}/I_{OFF} ratio and sub-threshold slope comparable with the majority of α-6T transistors reported in literature [37]. This is a very good result considering the absence of any optimization in our realization processes.

Moreover, the obtained electrical properties are indeed better than in devices grown with low E_K but increasing the substrate temperature. This fact clearly evidences that the role of E_K is more important than the substrate temperature in determining the final device performance. This is quite surprising considering the very different film morphology in the two cases. It seems the bigger domains formed when depositing with higher substrate temperature, but low molecules' kinetic energy, are not well connected each other to give the expected improvement in the electrical properties. .

We obtain the best results for the performance of α-6T field effect transistors fabricated using the molecular film grown at 13.1eV of Ek and 90°C.In this condition, the higher energy available for the molecules favours a better coalescence of the islands limiting the numbers of charge trapping sites in the thin film..

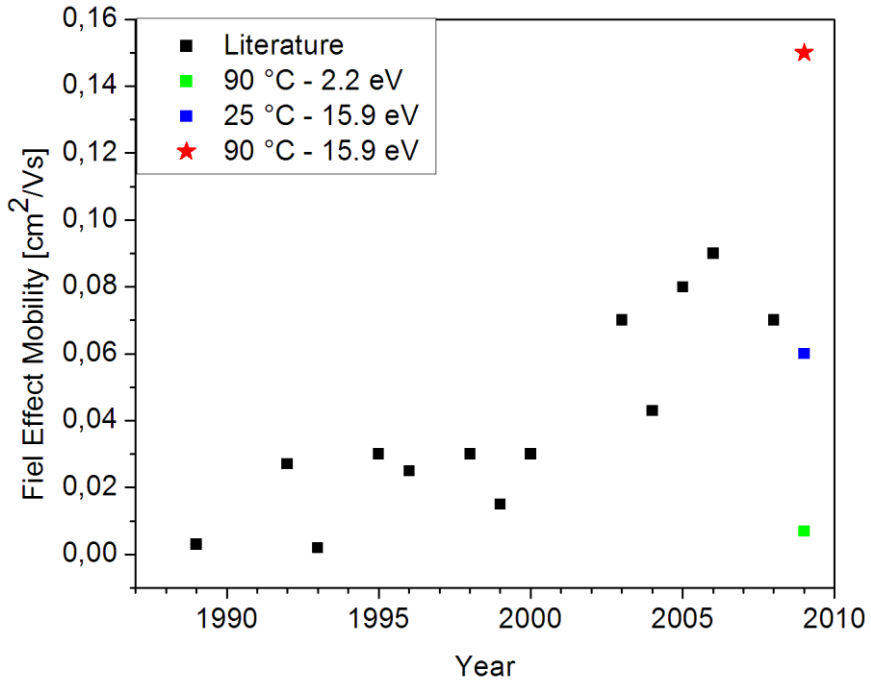

Figure 5.12: Comparison of the field effect mobility values found in literature for thin films of α-sexithiophene, compared to the average values calculated for the devices fabricated in this work.

The extracted mobility for these devices result to be $1.3 \cdot 10^{-1}$ $V \cdot cm^{-1} \cdot s^{-1}$ for linear and $1.5 \cdot 10^{-1}$ $V \cdot cm^{-1} \cdot s^{-1}$ for saturated regime. These values are close to that reported in literature up to know for the α-6T single crystal that are one order larger respect to that of the polycrystalline thin films [38,39], as can be seen in Figure 5.12.

The typical output characteristics are reported in Figure 5.13 with the comparison of the different growth conditions. In all the tested devices the "two ways scan" displays very small hysteresis and a very good linearity of the output curves in approaching the zero evidencing the absence of Schottky barrier effects of the source and drain contacts. Measurements on different devices show nice reproducibility of the transfer and output curves and very good stability in time.

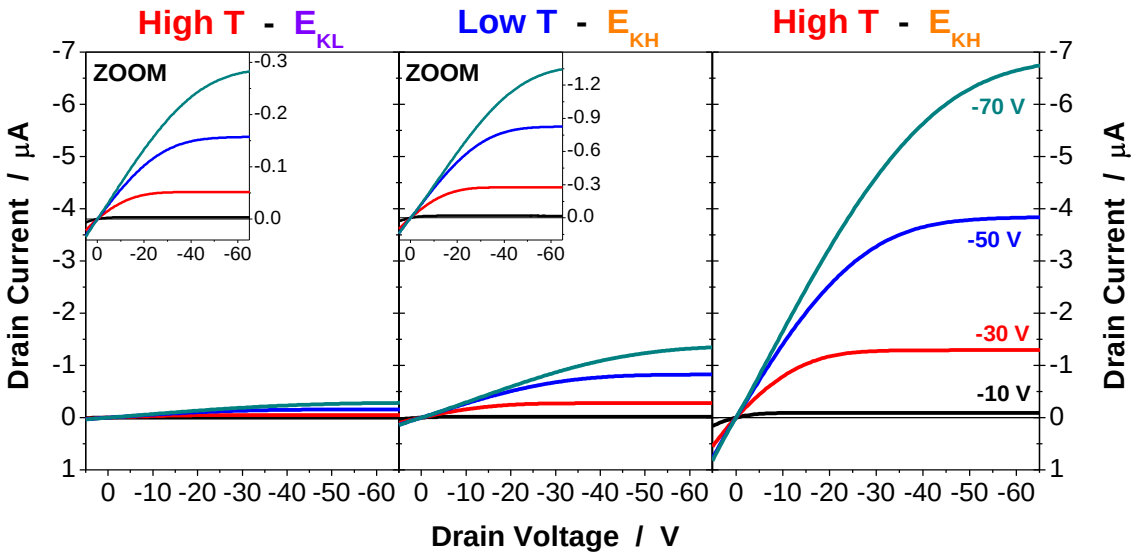

Figure 5.13: Comparison of the output curves of FET transistors fabricated with thicker films (of Figure 5.10), on the same scale. The insets in graphs a and b show a zoom of the relative output curves, to show their linearity in the origin.

5.3 Pentacene thin film growth

In this section we will present an investigation about pentacene sub-monolayer growth by SuMBD, focusing on the impact of the two components of impinging molecules' momentum. We should stress indeed that SuMBD allows to control not only the kinetic energy of the "bullets", but also the momentum, thus permitting to control the two components of it independently.

Pentacene, a promising candidate for organic electronic devices, has been (and still is) widely studied [40]. Recent efforts to improve the crystalline quality of pentacene thin films focused on supersonic molecular beam deposition as a new method for pentacene growth [41,42]. As we have seen, with this technique the kinetic energy of impinging molecules can be easily tuned from thermal energy up to several eV by means of changing the seeded molecular concentration in the carrier gas.

Several reports appeared on the initial growth of pentacene sub-monolayers [43, 44, 45, 46, 47], on the comparison between pentacene sub-monolayer morphologies for layers grown by SuMBD and by thermal sublimation [48] as well as on the carrier transport in field effect transistors based on SuMBD grown pentacene thin films [49].

So far, it has been demonstrated that the critical nucleus size, the crystallinity of the first monolayer and the structure of molecular islands in the first pentacene layer are all strongly correlated with the kinetic energy at which the molecules impinge on the substrate surface.

Moreover, with SuMBD, the first pentacene monolayer is completed before the second layer starts to grow, and a better quality pentacene monolayer with larger single crystal grains and much less grain boundaries was realized when $E_k > 5 - 6$ eV [44]. Improved carrier transport (hole mobility ~1.0 $cm^2V^{-1}s^{-1}$) was achieved in transistors based on SuMBD grown pentacene films [49]. A fundamental study of the interaction between energetic pentacene molecules and a SiO_x surface by A. S. Killampalli *et al.* [43] proposed that the decrease of pentacene adsorption probability with increasing E_k was dominated by a trapping mediated process [50].

The influence of parallel and normal momentum were found to be equally important for adsorption in these conditions, as demonstrated by applying the energy scaling process in a regime between the normal energy scaling [51, 52] and the total energy scaling [53, 54]. However, so far no detailed study of the critical nucleus size, the variation of molecular island size and the evolution of sub-monolayer coverage for SuMBD growth at different E_K and θ has been carried out.

This is what we aimed for in the investigations presented here about pentacene sub-monolayers deposited by SuMBD on a silicon oxide surface, in which we varied the kinetic energy of the impinging molecules and the incidence angle of the beam respect to the substrate during growth.

We will show that all the parameters strongly influence the molecular sticking coefficient, the molecular island density and size distribution as well as the critical nucleus size.

5.3.1 Growth control via momentum setting: a powerful tool

Pentacene was deposited on a 500 nm thick SiO_2/Silicon wafer (purchased from Silicon Quest International in USA) with a low root mean square surface roughness (around 5-6 Å) as determined by atomic force microscopy in tapping mode. All substrates were moderately hydrophobic, with water contact angles of 55 $\pm$ 2° determined by the sessile drop method [55]. Pentacene (Sigma-Aldrich, with a purity of 99.98%) was purified just before use by gradient vacuum sublimation [56].

Samples were prepared by exposure to the supersonic molecular beam (~10 mm in diameter), for different times (10, 20, and 30 minutes), at three different incident angles θ : 0° (normal) incidence, 45° and 75°, at room temperature. *Ex situ* AFM [57] was systematically carried out by scanning over multiple 10 × 10 μm^2 areas at the sample centre.

The molecular beam was characterized on-line in terms of chemical purity, flux, and energy distribution by combining time of flight (ToF) mass spectrometry and multi-photon ionization spectroscopy. We chose an

operating regime where no clustering effects [58] and contaminants were detectable. The typical flux was 6×10^{11} molecules/(s×cm^2), estimated by cross correlating the TOF spectra at different E_K of the beam with that of a Knudsen pentacene source used as standard. The two different E_K explored here (2.9 and 6.4 eV) were achieved by varying the degree of seeding through changing the helium carrier gas pressure.

For samples grown at θ = 0° the average height are 1.7±0.2 nm and 1.8±0.3 nm for E_k = 6.4 eV and 2.9 eV, respectively. Correspondingly at θ = 45° the heights observed are 1.7±0.1 nm and 1.6±0.1 nm while at θ = 75° the heights observed become 1.6±0.1 nm and 1.6±0.2 nm. These results are very close to the nominal length (~ 1.5 nm) of the long axis of single pentacene molecules and correspond quite well, within the experimental errors to other reports in literature [59], indicating that all the pentacene sub-monolayers consist of a single layer without the presence of a water layer on SiO_2 prior to pentacene deposition [60].

At these early stages of the growth (10 minutes of exposure time), the dependence of the morphology on the incident angle θ of the beam appears quite evident: both sub-monolayer coverage and molecular island size decrease with increasing θ, indicating that the molecular sticking coefficient is decreasing. At θ = 0, the island density augments from ~1.22 μm^{-2} for E_K = 2.9 eV to ~1.35 μm^{-2} for E_K = 6.4 eV, consistently with previous results [44].

When θ is increased to 45°, that is when the projection of the kinetic energy of the impinging molecules along and perpendicular to the surface are equal, we observe a significant change in both the density of island and of their size. Even more dramatic effects are clearly visible when most of E_K of the impinging molecules is along the surface of the substrate, for *i.e.* θ = 75°. Here we observe a much lower nucleation density than that at θ = 45°, namely ~0.46 μm^{-2} for the samples grown at E_K = 6.4 eV and ~ 0.64 μm^{-2} for the ones grown at E_K = 2.9 eV, and an even smaller typical island size than for θ = 45°.

Before a qualitative analysis comparing the AFM micrograph at the early stages of growth (10 min beam exposure) the role of the component of E_k associated with the momentum parallel to the surface, $E_{//}$, becomes evident.

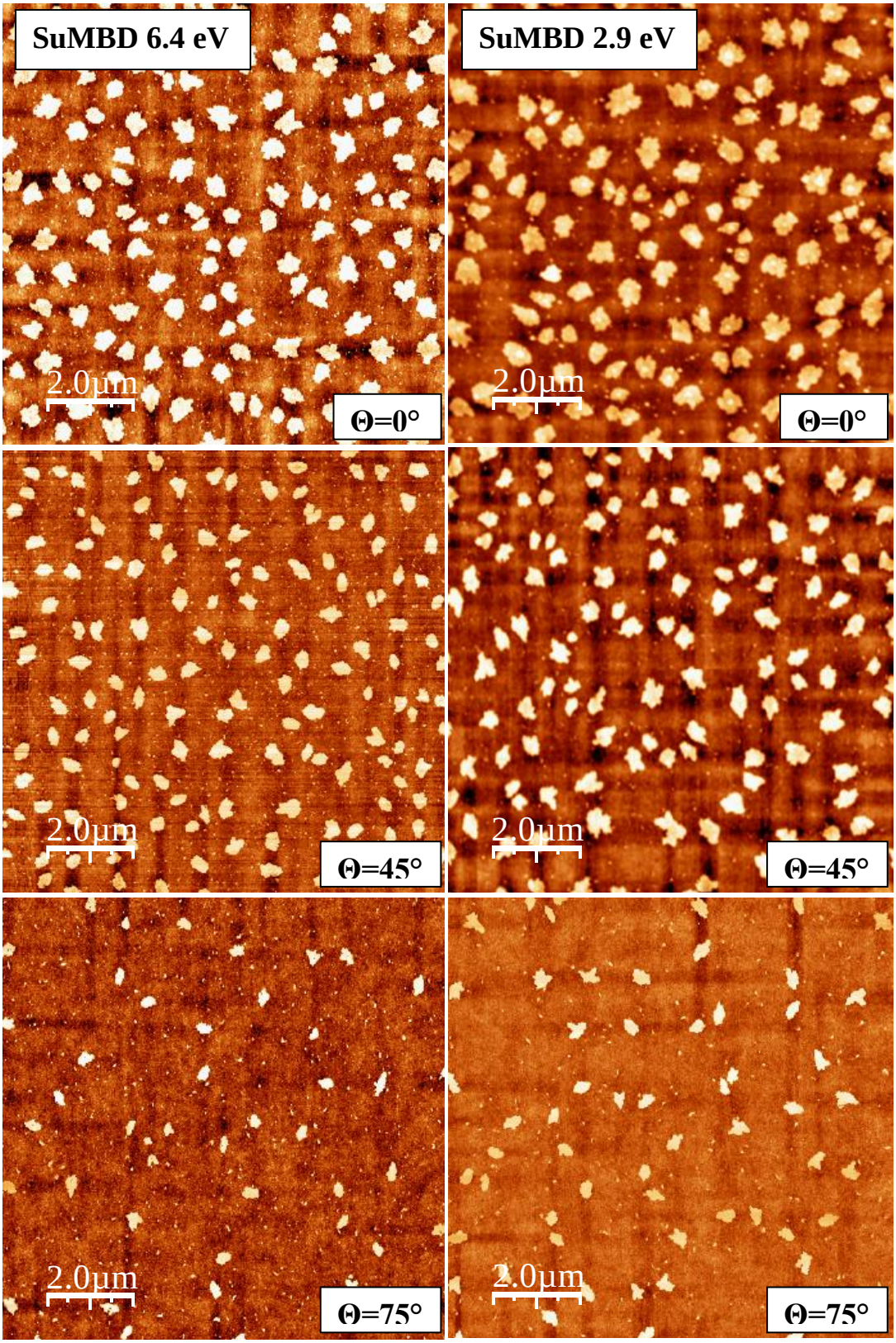

Figure 5.14: typical surface morphology of pentacene sub-monolayers as a function of the E_K and angle of the impinging molecules.

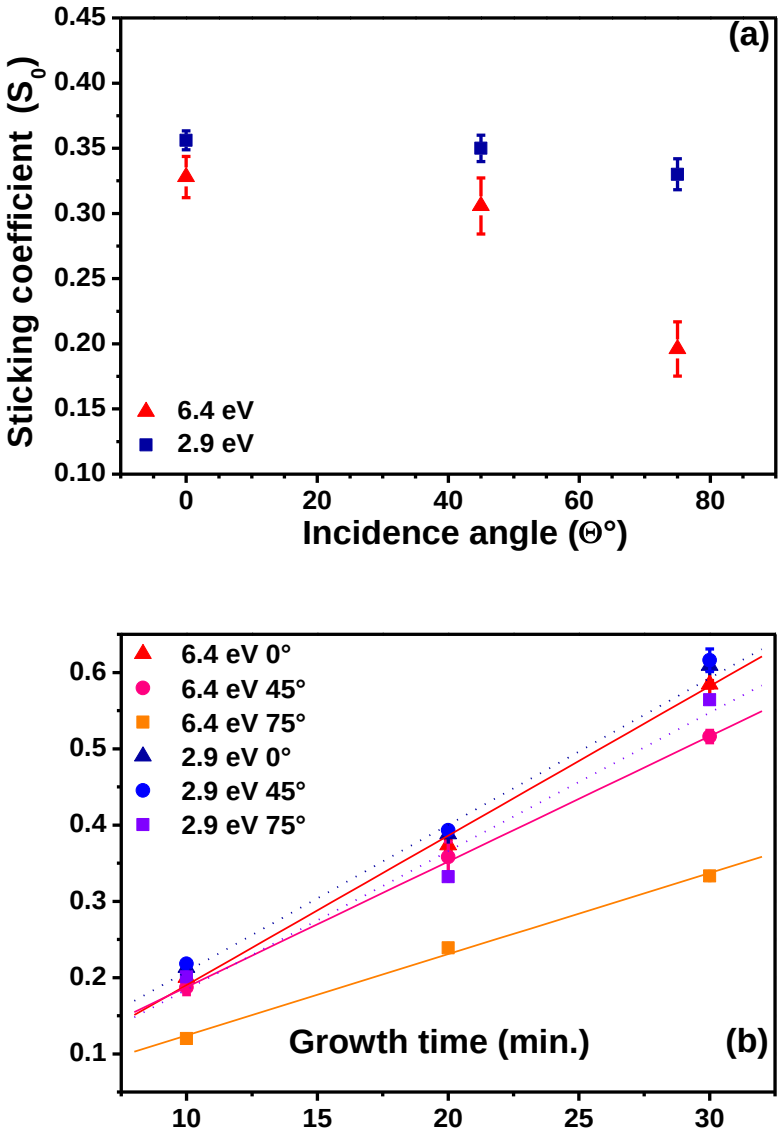

Figure 5.15: a) The molecular sticking coefficient of pentacene deposited at different kinetic energy of 6.4 eV and 2.9 eV as function of different incidence angle; b) Normalized coverage of pentacene sub-monolayers obtained in different SuMBD growth conditions as a function of growth time from the analysis of the AFM images. The linear fits of the data give the growth rate for each set of kinetic energy and different incidence angle.

The higher $E_{//}$, the larger is the probability for the molecules to be scattered out from the surface plane, so that not only the overall amount of materials deposited decreases (reduced sticking) also both density and size of islands. Figure 5.14 shows the typical surface morphology of the pentacene sub-monolayers as observed by AFM as a function of the incident angle for the two kinetic energies considered.

To quantify this effect we have investigated the sticking coefficient (S_0) under different growth conditions. We calculated the ratio between the number of adsorbed molecules using the samples of 10 min of growth and the incoming molecular flux. We took into account that with increasing θ the effective area of the surface hit by the beam increases from ~79 mm^2 at normal incidence to ~111 mm^2 at θ = 45° and ~304 mm^2 at θ = 75°.

Correspondingly, the effective flux on the surface decreases from 6000 molecules/(s×μm^2) determined at θ = 0°, to an estimated 4500 molecules/(s×μm^2) at θ = 45° and 1600 molecules/(s×μm^2) at θ = 75°. Figure 5.15a shows the calculated sticking coefficient S_0, as a function of incidence angle and of the kinetic energy of the incident molecules.

At θ = 0° the sticking coefficient is higher for growth at lower kinetic energy. For both E_K investigated, S_0 decreases with the incidence angle but more strongly for E_K = 6.4 eV. In fact, while for E_K = 2.9 eV we observe a reduction of only ~7% on going from θ = 0° to θ = 75°; for E_K = 6.4 eV the reduction is more than 68%.

The data also evidence a non linear relationship between S_0 and θ that is particularly evident for the higher kinetic energy. This is an indication of trapping processes involving possibly more than one step, as typical for direct trapping. Such a strong decrease of S_0 with increasing θ has been observed in very few cases, mostly when trapping occurs via dissipation of E_K associated with the normal component of momentum (normal energy scaling), $E_{\perp}$, as often true for simple (diatomic) molecules on surfaces of transition metals [61].

Most of the cases where normal energy scaling is not observed have been interpreted in terms of

i) strong corrugation effects either of the potential energy surface or of the physical substrate surface,

ii) the role of internal degrees of freedom and/or

iii) inefficient accommodation of parallel momentum [50].

A simple experimental way to quantify the relative role played by $E_{\perp}$ and $E_{//}$ is to introduce the empirical scaling function of the form $E_{k_i} f(\theta) = E_{k_i}(A\cos^2\theta_i + B\sin^2\theta_i)$ where *A+B=1* and the energy associated with the perpendicular (parallel) momentum scales with the coefficient *A* (*B*) [62]. Following this procedure for our data, we find values for *A* and *B* which, within the error bars, are identical to those found by A. S. Killampalli *et al.* [43]. However, we do not arrive at their same conclusion that the accommodation of parallel and perpendicular momentum are roughly equally important.

In fact, an understanding of these trends may be achieved by comparing with classical molecular dynamics simulations for SuMBD of ethane on Si(100) [61], a system where a similar sticking behavior was observed experimentally. These simulations show that the energy exchanged on first impact with the surface largely dictates whether the incident molecule will stay on the surface or not. During this first collision the energy associated with the normal momentum is dissipated very effectively, whereas that associated with the parallel momentum is not.

This process leaves the molecule in a vibrationally and rotationally excited state which allows it to make subsequent impacts with the surface and undergo further energy dissipation processes. However, molecules with a large parallel momentum were found to retain it in large part after the initial impact with the surface [50]. Parallel momentum, as well as any energy stored in rotations, can be converted into normal momentum during subsequent impacts, causing the molecules to scatter back into the vacuum.

Therefore, molecules with high kinetic energy impinging at glancing angles have a much larger probability of being scattered from the surface before the parallel momentum can be dissipated. Our data on pentacene where the sticking coefficient becomes smaller with larger incident angle and E_k strongly support this mechanism.

To gain further evidence, we analyzed the AFM images (not shown) for longer deposition times to determine the coverage normalized to the impinging molecular flux and found for all samples that this coverage monotonically increases with deposition time as shown in Figure 5.15b. The growth rate for each deposition condition, characterized by the kinetic energy and the incidence angle, was determined by linear fits, also shown in figure 5.14b.

Samples grown at E_k = 2.9 eV show very similar growth rates (~ 0.018 ÷ 0.019 ML/min) for all incident angles of the molecular beam (see dotted lines in Fig. 5.15b). However, for samples grown at E_k = 6.4 eV, the growth rate slightly decreases (from ~0.019 ML/min to ~0.016 ML/min) with increasing θ from normal incidence to 45°, and drops to a much smaller value of ~0.011 ML/min for θ = 75° (see continuous lines in Fig. 5.15b). The latter is another strong indication of the role played by the parallel momentum.

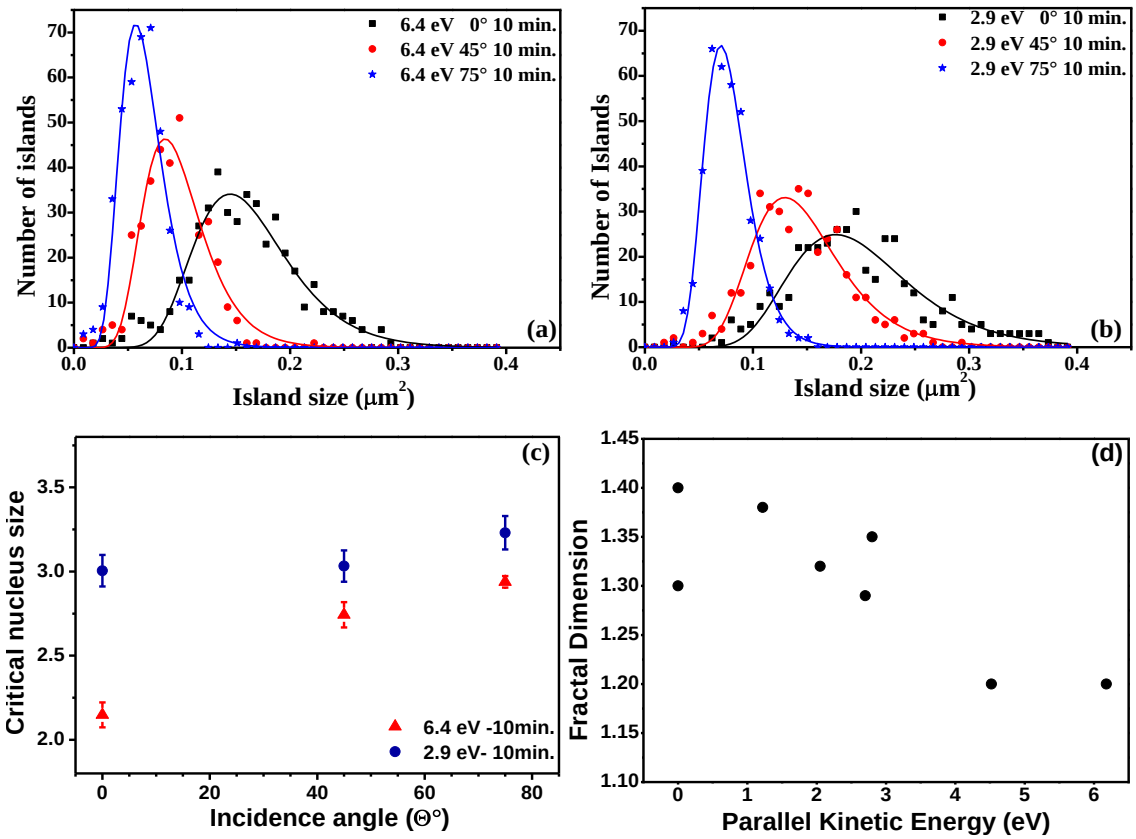

Figure 5.16: (a and b) Island size distribution of pentacene sub-monolayers grown on SiO_2 by 10 min exposure to the supersonic beam

operated at two pentacene different kinetic energies (a) E_K = 6.4 eV and (b)E_K = 2.9 eV at normal incidence, θ = 45° and θ = 75°. (c) Critical nucleus size for island formation obtained from pentacene submonolayers after 10 min of deposition of molecules with kinetic energies of 6.4 and 2.9 eV, plotted as function of θ at normal incidence, 45° and 75°. (d) Fractal dimension of the island shape as a function of $E_{//}$ component.

In these conditions, $E_{//}$ becomes so high that it cannot be dissipated anymore except at specific points (defects) where the trapping energy is large enough. This is consistent with the fact that for high E_k and grazing incidence AFM (not shown) reveals a practically constant density of islands and much slower ripening of the islands, if present at all.

Further insight into the growth dynamics can be obtained from studying the island size distribution and the average island size (A_{av}). We considered only the images collected from pentacene sub-monolayers after 10 min of deposition where the onset of island coalescence is not yet reached.

In figure 5.16 we report the histograms of the island size (A) for different growth conditions as obtained from AFM images collected over 5 scanning areas of 10 $\times$ 10 μm^2 for each case, together with the fit (using a log normal function) with a single peak.

The average island size is given by the position of the peak in the distribution curve. The obtained average island sizes were found to be 0.15$\pm$0.02, 0.09$\pm$0.01 and 0.06$\pm$0.01 μm^2 for samples grown at E_K = 6.4 eV, at normal incidence, θ = 45° and 75°; the corresponding values for E_K = 2.9 eV amounted to 0.19$\pm$0.03, 0.14$\pm$0.02 and 0.07$\pm$0.01 μm^2 for normal incidence, θ = 45° and 75°. The average island size decreases with increasing θ and for each incidence angle while the average island sizes for samples grown with E_K = 2.9 eV is always larger than the one for samples grown with E_K = 6.4 eV.

This suggests that less molecule - surface scattering and lower surface diffusivity caused by the smaller E_K favor lateral expansion of the islands via trapping of more molecules on the surface. With increasing θ, the distribution of island sizes obtained for the growth becomes narrower for both the kinetic

energies used. The full width at half maximum of the peak drops from 0.10 μm^2 (0.12 μm^2) at normal incidence to 0.06 μm^2 (0.10 μm^2) at θ = 45° and to 0.05 μm^2 (0.05 μm^2) at θ = 75° for samples grown with E_K = 6.4 eV (2.9 eV). This indicates that higher island size uniformity is achieved at larger incidence angle.

A quantitative assessment of the growth was achieved by determining the critical nucleus i (i + 1 = number of molecules forming a stable nucleus), based on the general scaling function $f_i(u) = C_i u^i e^{-i a_i u^{\frac{1}{a_i}}}$ introduced by Amar and Family [63], extended to Pentacene growth by Ruiz *et al.* [64], and re-proposed by Tejima *et al.* and Stadlober *et al.* [65,66]. C_i and a_i are constants determined by hypergeometrical equations for i = 0*; . . . ;* 3 that assure normalization and proper asymptotic behavior of $f_i(u)$. We compared the normalized island size distributions of films grown in different conditions with the predictions of the general scaling model calculated for i = 1, 2, and 3.

In figure 5.16c, the critical nucleus size is plotted as a function of E_k and θ. For samples grown with E_K = 2.9 eV, i = 3 for all incidence angles, while for those grown with E_K = 6.4 eV, at normal incidence, i = 2 as found previously [44] but for θ = 45° and 75°, i=3. This indicates that it is the normal energy which determines the critical nucleus size and not the total E_K. In fact, the normal energy components of molecules impinging with E_K = 6.4 eV at θ = 45° and θ = 75°, are 4.5 and 1.6 eV, respectively, and hence fall into the range < 5.5-6.0 eV, where we previously found i=3 at normal incidence [44].

E_k (eV) \ θ (°)	0	25	45	75
2.9	1.40±0.03	1.38±0.03	1.32±0.03	1.35±0.03
6.4	1.30±0.02	1.28±0.03	1.20±0.02	1.20±0.03

Table 5.3: Fractal island dimension as a function of E_K and θ.

We also investigated how kinetic energy and incidence angle of the impinging molecules influence the island shape. To this end we determined the fractal dimension for different growth conditions from AFM images. The island fractal dimension (D_f) calculated by the area-perimeter relationship $P = kA^{D_f/2}$, as proposed in [67], where P is the island perimeter, A its area, k a scaling constant and D_f the fractal dimension, gives important information about the molecular diffusion length and on the assembling processes of the molecules [47].

As reported in Table 5.3, D_f scales with θ for all E_k: the incident angle and/or the kinetic energy of the impinging molecules increase, the island fractal dimension decreases. These trends confirm that higher surface mobility of the pentacene leads to more compact islands. To better understand whether parallel or perpendicular moment play the major role, we analyzed the data as a function of $E_\perp$ and $E_{//}$.

The plot of the fractal dimension vs. $E_\perp$ does not show any particular dependence, indicating that this energy component has only a minimal role in the molecular surface diffusion while D_f vs. $E_{//}$, reported in figure 5.15d, shows a clear trend: the fractal dimension of the island shape decreases with increasing $E_{//}$. We can therefore conclude that the energy component associated with the moment parallel to the surface determines the island shape and size distribution.

We can rationalize these observations in the following way: when pentacene collides with the SiO_2 surface, it looses energy through different mechanisms which depend on its momentum and kinetic energy. In particular, $E_\perp$ determines the formation of the initial nuclei: increasing this component we observed that fewer molecules needed for the formation of stable nuclei. Higher $E_\perp$ also favors a higher number of islands and a decreasing of their distance between them the formation of more compact islands and also their aggregation.

The $E_{//}$ works on processes involved in the interaction between surface and molecules. Its dissipation modifies the sticking coefficient of the molecules and their relaxation processes increasing their surface mobility. High value of $E_{//}$ decrease the number of molecules on surface but favour the

formation of more compact (less fractal) island, better for the realization of ordered films.

As conclusion the $E_{\perp}$ is jointed to molecular-molecular interaction on the surface while the $E_{//}$ could be related to processes of interaction between molecules and surface phonon. To optimize the growth processes of organic molecules such as pentacene we need the right optimization of the two components.

5.4 Pentacene organic field effect transistors[††]

As we have seen, SuMBD is a growth technique for organic semiconducting molecules that gives unprecedented control on morphology and structure by tuning the kinetic energy of the impinging molecules. This is the key factor by which we could control the growth of high quality films showing state of the art electrical properties for pentacene films.

Along his section, we will show that exploiting such ability to control structure and morphology of the films, one could tailor the gas response of the organic thin film transistors. We envisage the potential of such devices in applications where the transistor configuration offers new strategic opportunities as in gas sensing and in microfluidics.

In the framework of the ongoing efforts for producing better performing organic semiconductors for thin film transistors (OTFTs), several molecular materials, with quite different chemical and physical properties, have been produced and tested [68]. Organic molecules have also been employed as gas sensors [69,70], due to their several potential advantages in terms of costs, compatibility with plastic substrates and biocompatibility.

The simplest and first sensing devices based on organics, were the chemiresistors [71] (see Chapter 1) and only recently the performance offered by the OFETs are being explored because of improved thin film and material

[††] This section is based on T. Toccoli, A. Pallaoro, M. Tonezzer, N. Coppedè and S. Iannotta*, **"OFET for gas sensing based on SuMBE grown pentacene films"**, ***Solid State Electronics***, 52 (2008) 417.

quality [69]. The advantages of FET sensors arise from the ability to control electronically in an active mode the gas sensing properties of the organic layer that plays simultaneously also the role of the semiconductor in the transistor.

The gas response appears in different properties of the FET (the drain current, the threshold voltage, etc.), whereas the modulation of the gate voltage can be used to enhance sensitivity to purge the active layer and to stabilize the response [69]. One of the actual limits of organic materials for FETs is the still low carrier mobility when compared to their inorganic counterparts.

The results show that we achieved on the realization of pentacene FETs [72] improving their field effect mobility make these devices more appealing. It is well known that molecular order and crystallinity of organic thin films are crucial for the final performance of OTFTs [73].

Controlling these factors, together with a better understanding and engineering of the needed interfaces, represents a feasible approach for the improvement in performance required to make organic devices competitive.

To this end we have developed our approach. We have already shown that via supersonic molecular beam deposition (SuMBD) [74] unprecedented control can be achieved on the growth of thin films of different organic materials such as oligothiophenes [75], metal phthalocyanines [76], and also pentacene [77].

The key factor controlling the films quality is the kinetic energy (E_K) of the impinging molecules [72,76]. The aim of this work is to show that pentacene films with a high degree of order and hence good field effect mobility can be ideally suitable for sensing applications, because the grain boundaries that act as traps for gases and volatile organics compounds (VOC) [69], can be controlled in density and shape.

5.4.1 Experimentals

The apparatus and the deposition method have been previously described [78]. The setup essentially consists of two differentially pumped chambers where the supersonic beams are realized, an ultrahigh vacuum deposition chamber and a time of flight mass spectrometer for beams characterization.

The substrates are cut to desired dimensions from a highly doped silicon wafer covered by a 100 nm (OTFTs) or 160 nm (OFET sensors) thermal oxide layer. They have been cleaned in hot (50 °C) isopropyl alcohol, and then outgassed at about 250 °C in the deposition chamber for about 12 h. Pentacene films, 35-40 nm thick, have been deposited at room temperature (RT) using He as carrier gas with a typical deposition time of 300 min.

Film thickness was determined by calibrating with the time of flight mass spectrometer the flux of the pentacene molecules, for all the different E_K on separate films as reported elsewhere [72]. The tuning of E_K was achieved by changing the molecular dilution in the source keeping the flux of pentacene constant. With this apparatus we can continuously control and stabilize the E_K from thermal (tens of meV) up to about 13.0 eV seeding the pentacene in hydrogen [73].

To realize the top contact configuration of our FETs, we deposited 50 nm thick gold drain and source contacts through a shadow mask on the pentecene films in a separate system. We realized two sets of devices, the first one to be used to test the final performance and the second one to be used as sensors.

The dimensions of the first devices series were: channel width W = 200 lm; channel length L = 20, 35, and 100 lm, whereas the second series had the dimensions: W = 5 mm and L = 0.5 mm. All the films have been characterized by tapping mode AFM before to deposit the gold contacts, using a Russian NTMDT instrument, whereas the electrical characterization of both devices types has been carried out in a probe station equipped with an Agilent 4156C source meter.

5.4.2 Devices characterization

To understand the effect of the kinetic energy on the growth, we characterized the thin films morphology by tapping mode AFM. Fig. 5.17a shows a micrograph of a pentacene film grown at a K_E of 3.6 eV having a polycrystalline terraced structure with typical grain lateral size of about 1 lm.

The grains are characterized by a stepwise morphology having terraces with 30-60 nm of lateral size and the height between two terraces of 1.5 nm which corresponds to the molecular length. Such morphology on Si/ SiO_2 substrates was obtained by thermal evaporation keeping the substrate heated at about 50 °C to increase the surface mobility of the molecules.

Films grown at higher E_K (6.5 eV), as shown in Fig. 5.17b, have a strongly different morphology. They are characterized by very wide and extended flat areas having lateral sizes of several microns. Those large structures are delimited by 1.5 nm steps corresponding to the length of a pentacene molecule and have some defects that occasionally appear.

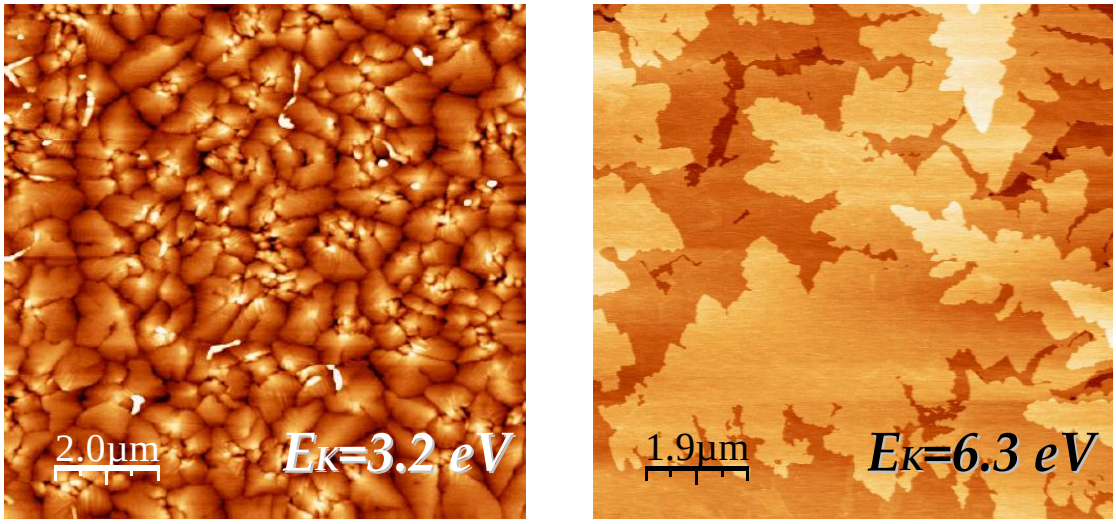

Figure 5.17: 10 µm x 10 µm AFM images of the samples grown at (a) KE of 3.6 eV and (b) 6.5 eV. Growth at RT on SiO_2 with a flux of 1ML/15min.

Up to now such a morphology has never been achieved by thermal evaporation. It is quite evident that at higher K_E, achieved by high dilution of

pentacene in the He beam at fixed molecular fluxes, corresponds a greatly ordered film that is characterized by a layer by layer growth process. The molecular K_E produces a sort of local annealing [70] thus giving a final structure similar to that of the single crystal. A more detailed study of the effects of the K_E on the pentacene growth process is reported in reference [79].

Based on this great improvement on the control on the structure of the pentacene films achievable by SuMBE we Pentacene thin film gas sensors realized two sets of OFETs using the two KE mentioned above. Since our goal is to use organic molecules to build gas sensor FETs, we extracted the electrical characteristics of our devices both in vacuum and in air to verify their stability in different conditions.

Figure 5.18 shows the typical transfer characteristics in the linear regime (V_{DS} = -1 V) of the devices. By comparing Figure 5.18a and b, it becomes quite evident that the performance of the films grown at higher kinetic energy (Fig. 5.18b) is better than for the other. The carrier mobility reaches values (larger than 1 V cm^{-1} s^{-1}) that are state of the art for FET grown on the clean Si/ SiO_2 surface that is without any interface layer such as SAM [72].

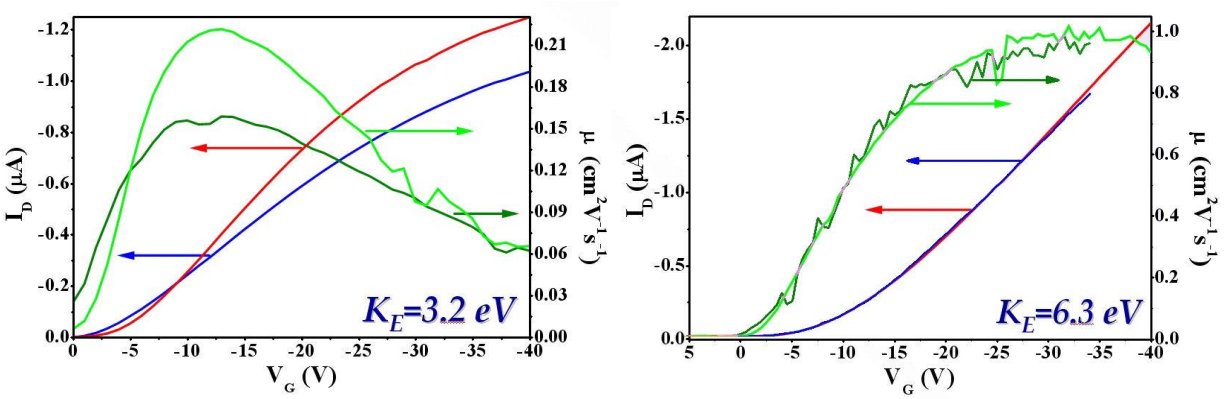

Fig. 5.18: Transfer characteristics (red and blue lines), measured at V_{DS} = -1 V and field effect mobility (green lines) of pentacene samples grown by SuMBE at (a) 3.6 eV and (b) 6.5 eV. The devices have been tested both in air (blue and dark green lines) and vacuum (red and light green lines).

Fig. 5.18a also represents the behaviour in both vacuum and air of the OFET prepared at low E_K. The change of the electrical characteristic of the transistor when exposed to air is very strong. This is due to the large number of grain boundaries that even though limits the performance of the device, increases the trap sites for the volatiles (in this case the humidity present in the air [80]). The films grown at high E_K (Fig. 5.18b), instead show almost the same behaviour both in vacuum and in air. In this case the strongly reduced number of grain boundaries makes the device's performance almost insensitive to the air exposure.

To better understand the difference between the two types of devices we report in Table 5.4 a summary of the principal electrical characteristics of these pentacene FETs measured both in vacuum and in air. The table confirms quantitatively the observations made from the comparison of the different curves shown in Fig. 5.18. The devices grown at higher E_K show better performance that are barely affected by the environmental conditions.

	3.6eV Samples		**6.5 eV Samples**	
	Vacuum	Air	Vacuum	Air
V_T [V]	- 4.9	- 3.0	- 11.5	- 10.9
I_{ON}/I_{OFF}	$1 \cdot 10^4$	$1 \cdot 10^3$	$3 \cdot 10^5$	$2 \cdot 10^5$
S_TSlope [$V \cdot dec^{-1}$]	1.9	2.0	0.8	0.9
μ [$cm^2 \cdot V^{-1} \cdot s^{-1}$]	0.22	0.16	1.00	0.95

Table 5.4: Summary of result of the electrical characterization of the OTFT having the pentacene layer grown at 3.6 eV and 6.5 eV, respectively

This is an important aspect because usually pentacene FETs fail to work as sensors for their difficulty to release the volatile adsorbed during the VOC absorption. The reason is likely due to the presence of grain boundaries which trap more strongly the volatiles and thus causing very long recovery times [69].

Tuning E_K allows to produce film morphologies much less sensitive to air exposure, hence tailoring the gas sensing activity and keeping a high carrier mobility so that the transistor performance is still very good. This is the reason why we used pentacene films grown at high kinetic energy to realize devices for sensing applications.

Fig. 5.19 shows the electrical characteristic (output curve) of a pentacene FET device realized for sensing applications. The devices were tested in both nitrogen (red solid lines) and nitrogen + ethanol 5 $\cdot 10^4$ ppm (blue dashed lines) atmosphere.

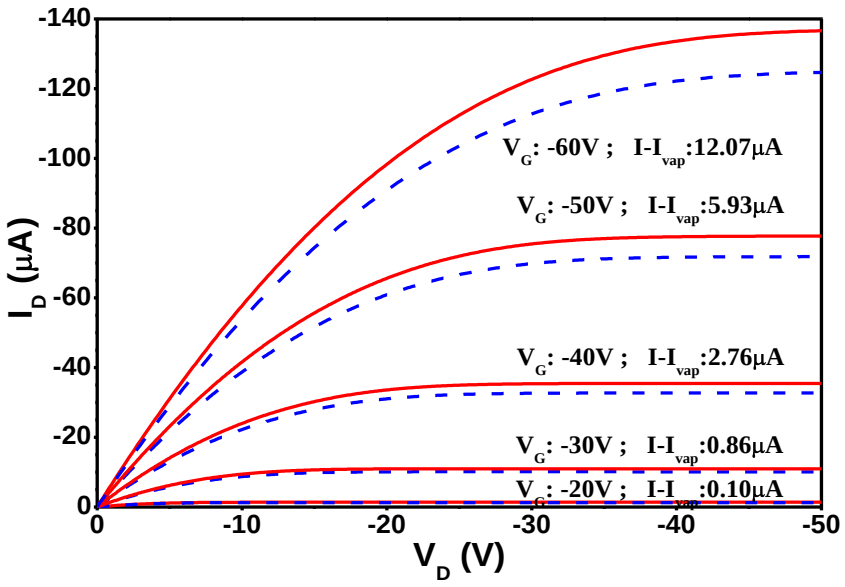

Fig. 5.19. OFET output characteristics for pentacene SuMBD grown film at E_K = 6.5 eV. Red solid lines refer to the device tested in nitrogen flow, blue dashed lines in vapours of ethanol. The figure reports also the difference between the drain current in nitrogen and in ethanol vapours at the different gate bias applied.

The output characteristics reported in the figure confirm the good quality of the devices which shows low contact resistance and good saturation current. Furthermore, the difference between each solid line and its

corresponding dashed line, gives the device response when used as a gas sensor.

It is clear from the figure that the device behaves as a gas sensor and its sensitivity can be tuned by changing the gate voltage and consequently increased by a factor higher than 120. This is one of the major advantages of the FET sensors with respect to the corresponding chemiresistor the performance of which can be approximated to, for a gate voltage equal to 0.

In Table 5.5 we report the summarized electrical characteristics of the devices used as sensors both in the linear (V_{DS} = -1 V) and saturation (V_{DS} = -50 V) regimes, showing the effect of the VOC on these properties.

	Nitrogen		**Nitrogen + Ethanol**	
	V_D = - 10V	V_D = - 50V	V_D = - 10V	V_D = - 50V
V_T [V]	- 25.9	- 19.1	- 26.4	- 19.4
I_{ON}/I_{OFF}	$7 \cdot 10^6$	$3 \cdot 10^5$	$7 \cdot 10^6$	$3 \cdot 10^5$
S_TSlope [$V \cdot dec^{-1}$]	1.08	1.85	1.12	1.80
μ [$cm^2 \cdot V^{-1} \cdot s^{-1}$]	0.67	0.67	0.65	0.64

Table 5.5: Summary of result of the electrical characterization of the OFTF used as a gas sensor for ethanol vapours

5.4.3 Sensors characterization

We assessed the effective sensing properties our FETs by monitoring the time evolution of the drain current at fixed V_G and by alternatively exposing the devices to pure nitrogen and nitrogen with saturated ethanol vapours. Figure 5.20 shows the typical observed trends of I_D, collected at V_{DS} = -70 V and at V_G = -60 V. The effects of the ethanol on the performance of the FET are clearly visible.

The drain current decreases when the devices were exposed to the vapours and recovers the original value when the exposure to the gas is stopped. The background drift observed is mainly caused by the long recovery time related to the low operating temperature. In fact the original values are fully recovered after about half an hour at room temperature. The overall performance observed, when compared to the state of the art, looks very promising for the application of our devices in gas-sensing.

We have shown that the OFETs based on films fabricated by SuMBD at E_K = 6.5 eV give an overall performance that improves the state of the art for devices having a similar architecture, where no interface layers are used. In fact the best carrier mobility values reported to date are typically around 0.5 $cm^2\ V^{-1}\ s^{-1}$ [81] that is about one-half the mobility of the devices discussed here.

The better performance is correlated to the thin film growth and in particular to its morphology, structure and order and is achieved by SuMBD that is well suited to produce highly ordered films by tuning the kinetic energy of the molecular precursor in the beam. The electronic properties shown in this work demonstrate that a gas sensor made by SuMBD is sensitive, reliable and stable.

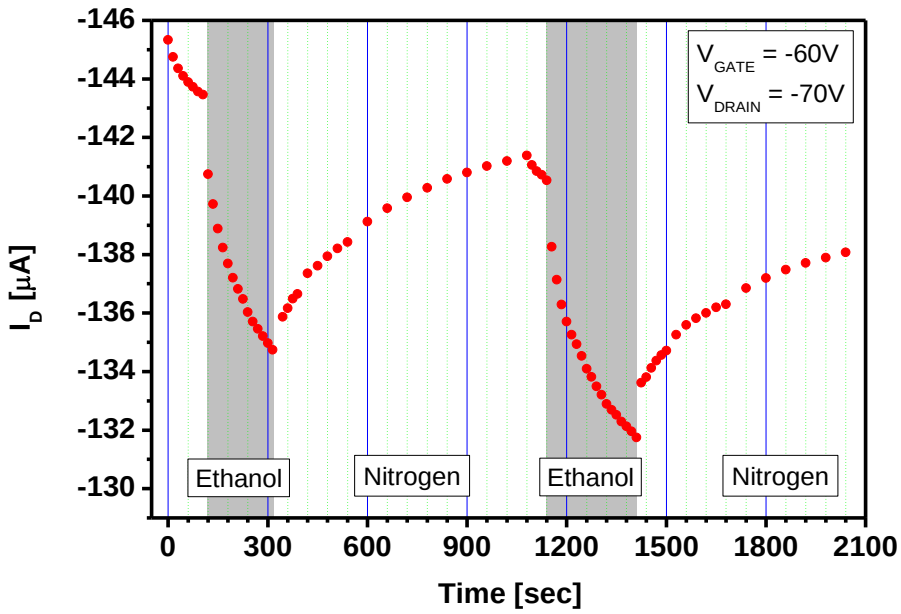

Figure 5.20: I_D collected at V_{DS} = -70 V and V_G = -60 V as a function of time. The device was exposed alternatively to the flux of nitrogen and nitrogen.

Furthermore, the sensor sensitivity can be increased of a factor up to 120 just by varying the gate voltage from 0 (as in the simple resistors) up to the typical operating voltage of the device. This gives the device a higher versatility and a better outlook for sensing applications.

This preliminary work demonstrates that the one of the main bottlenecks of organic thin films to be used as sensing devices, is their intrinsic low charge carrier mobilities. Our novel approach can improve this figure of merit, allowing the fabrication of higher response gas sensors.

[1] A.R. Murphy and J. M. J. Fréchet, *Chem. Rev.* 107 (2007)1066.

[2] A. Facchetti, *Mater. Today* 10 (2007) 28.

[3] C. Reese and Z. Bao, *Mater. Today* 10 (2007) 20.

[4] R. Ruiz, D. Choudhary, B. Nickel, T. Toccoli, K.C. Chang, A.C. Mayer, P. Clancy, J.M. Blakely, R.L. Headrick, S. Iannotta, and G.G. Malliaras, *Chem. Mat.* 16 (2004) 4497.

[5] F. Schreiber, *Phys. Stat. Sol. A* 210 (2004) 1037.

[6] J.A. Venables, G.D.T. Spiller and M. Hanbucken, *Rep. Prog. Phys.* 47 (1984) 399.

[7] T. Kakudate, N. Yoshimoto, Y. Saito, *Appl. Phys. Lett.* 90 (2007) 081903.

[8] N. Coppedè, T. Toccoli, A. Pallaoro, F. Siviero, K. Walzer, M. Castriota, E. Cazzanelli, and S. Iannotta, *J. Phys. Chem. A* 111 (2007) 12550.

[9] K. Takimiya, Y. Kunugi and T. Otsubo, *Chem. Lett.* 36 (2007) 578.

[10] F.O. Goodman and H.Y. Wachman, *Dynamics of Gas Surface Scattering*, Academic, New York (1976).

[11] S. Iannotta, T. Toccoli, *J. Polym Science: B* 41 (2003) 2501.

[12] P. Milani and S. Iannotta, *Synthesis of Nanophase Materials by Cluster Beam Deposition*, Springer Berlin (1999).

[13] J. Ackermann, C. Videlot, P. Dumas, A. El Kassmi, R. Guglielmetti, V. Safarov, *Org. Electr.* 5 (2004) 213.

[14] Y. Wu, T. Toccoli, N. Koch, E. Iacob, A. Pallaoro, P. Rudolf, and S. Iannotta, *Phys. Rev. Lett.* 98 (2007) 076601.

[15] T. Toccoli, A. Pallaoro, N. Coppedè, S. Iannotta, F. De Angelis, L. Mariucci, and G. Fortunato, *Appl. Phys. Lett.* 88 (2006) 132106.

[16] A. Sassella, M. Campione, A. Papagni, C. Goletti, G. Bussetti, P. Chiaradia, V. Marcon, G. Raos, *Chem. Phys.* 325 (2006) 193.

[17] T. Siegrist, C. Kloc, R.A. Laudise, H.E. Katz, R.C. Haddontrs, *Adv. Mater.* 10 (1998) 379.

[18] S. Iannotta, T. Toccoli, F. Biasioli, A. Boschetti, and M. Ferrari, *Appl. Phys. Lett.* 76 (2000) 1845.

[19] C.D. Dimitrakopoulos and P.R.L. Malenfant, *Adv. Mat.* 14 (2002) 99.

[20] P. Wolfer, C. Müller, P. Smitha, M.A. Baklar, N. Stingelin-Stutzmann, *Synth. Met.* 157 (2007) 827.

[21] S.E. Fritz, S. Mohapatra, B.T. Holmes, A.M. Anderson, C.F. Prendergast, C.D. Frisbie, M.D. Ward, and M.F. Toney, *Chem. Mater.* 19 (2007) 1355.

[22] A. Hoppe, T. Balster, T. Muck, and V. Wagner, *Phys. Stat. Sol. A* 205 (2008) 612.

[23] C. Videlot-Ackermann, J. Zhang, J. Ackermann, H. Brisset, Y. Didane, P. Raynal, A. El Kassmi, F. Fages, *Current Appl. Phys.* 9 (2009) 26.

[24] A. R. Murphy and J. M. J. Frechet, *Chem. Rev.* 107 (2007) 1066.

[25] D.R. Miller, *Atomic and Molecular Beam Methods*, Vol. 1 (Ed: G. Scoles), Oxford University Press New York, (1988).

[26] F. Dinelli, J.-F. Moulin, M. A.Loi, E. Da Como, M. Massi, M. Murgia, M. Muccini, F. Biscarini, J. Wie and P. Kingshott, *J. Phys. Chem. B*. 110 (2006,) 258.

[27] J. Park, J.-H. Bae, W.-H. Kim, S.-D. Lee, J.S. Gwag, D.W. Kim, J.C. Noh, J.S. Choi, *Solid State Electr.* 54 (2010) 1650.

[28] A.-L. Barabási, H.E. Stanley, *Fractal Concepts in Surface Growth*, Cambridge University Press (1995).

[29] S.Y. Yang, K. Shin and C.E. Park, *Adv. Funct. Mater.* 15 (2005) 1806-1814.

[30] G. Hlawacek, P. Puschnig, P. Frank, A. Winkler, C. Ambrosch-Draxl, and C. Teichert, *Science* 321 (2008) 108.

[31] D. Guo, S. Ikeda, K. Saiki, *Thin Solid Films* 515 (2006) 814.

[32] J.E. Goose and P. Clancy *J. Phys. Chem. C,* 111 (2007) 15653.

[33] A. Boschetti, A. Cagol, C. Corradi, R. Jacobs, M. Mazzola, S. Iannotta, *Chem. Phys.* 163 (1992) 179.

[34] M. van Opbergen, A. Boschetti, and S. Iannotta, *Opt. Express* 4 (1999) 53.

[35] Frank-J. Meyer zu Heringdorf, M. C. Reuter & R. M. Tromp, *Nature* 412 (2001) 517.

[36] P. Stallinga, H.L. Gomes, F. Biscarini, M. Murgia and D.M. Leeuw, *J. Appl. Phys.* 96 (2004) 5277.

[37] B.C. Shekar, J. Lee and S. Rhee, *Korean J. Chem. Eng.* 21 (2004) 267.

[38] J.A. Letizia, J. Rivnay, A. Facchetti, M.A. Ratner and T.J. Marks, *Adv. Funct.Mater.* 20 (2010) 50.

[39] G. Horowitz, M.E. Hajlaoui and R. Hajlaoui, *J. Appl. Phys.* 87 (2000) 4456.

[40] R. Ruiz, D. Choudhary, B. Nickel, T. Toccoli, K.C. Chang, A.C. Mayer, P. Clancy, J.M. Blakely, R.L. Headrick, S. Iannotta, G.G. Malliaras, *Chem. Mat.*, 16 (2004) 4497.

[41] S. Iannotta and T. Toccoli, *J. Polymer Sci.* B, 41 (2003) 2501.

[42] L. Casalis, M.F. Danisman, B. Nickel, G. Bracco, T. Toccoli, S.Iannotta and G. Scoles, *Phys. Rev. Lett.* 90 (2003) 206101.

[43] A.S. Killampalli, T.W. Schroeder and J.R. Engstrom, *Appl. Phys. Lett.* 87 (2005) 033110.

[44] Y. Wu, T. Toccoli, N. Koch, E, Iacob, A. Pallaoro, P. Rudolf and S. Iannotta, *Phys. Rev. Lett.* 98 (2007) 076601.

[45] D. Choudhary, P. Clancy, R. Shetty and F. Escobedo, *Adv. Func. Mater.* 16 (2006) 1768.

[46] F.J. Meyer zu Heringdorf, M.C. Reuter, R.M. Tromp, *Appl. Phys. A* 78 (2004) 787.

[47] S. Pratontep, M. Brinkmann, F. Nuesch and L. Zuppiroli, *Phys. Rev. B* 69 (2004) 165201.

[48] Y. Wu, T. Toccoli, J. Zhang, N. Koch, E, Iacob, A. Pallaoro, S. Iannotta and P. Rudolf, *Appl. Phys. A* 95 (2009) 21.

[49] T. Toccoli, A. Pallaoro, N. Coppedè, S. Iannotta, F.D. Angelis, L. Mariucci and G. Fortunato, *Appl. Phys. Lett.* 88 (2006) 132106.

[50] C.T. Reeves, B.A. Ferguson, C.B. Mullins, G.O. Sitz , B.A. Helmer and D.B. Graves, *J. Chem. Phys.* 111 (1999) 7567.

[51] F.O. Goodman and H.Y. Wachman, *Dynamics of Gas – Surface Scattering*, Academic, New York (1976).

[52] J.A. Barker and D.J. Auerbach, *Surf. Sci. Rep.* 4 (1984) 1.

[53] S. Andersson, L. Wilzen and J. Harris, *Phys. Rev. Lett.* 57 (1986) 1603.

[54] C. T. Rettner, H. Stein and E. K. Schweizer, *J. Chem. Phys.* 89 (1988) 3337.

[55] A.W. Neumann and R.J. Good, in *Surface and Colloid Science*, edited by R. J. Good and R. R. Stromberg (Plenum, New York, 1979), Vol. 11

[56] O.D. Jurchescu, J. Baas, and T.M. Palstra, *Appl. Phys. Lett.* 84 (2004) 3061.

[57] I. Horcas, R. Fernandez, J.M. Gomez-Rodriguez, J. Colchero, J. Gomez-Herrero, and A.M. Baro, *Rev. Sci. Instr.* 78 (2007) 013705.

[58] P. Milani and S. Iannotta, *Cluster Beam Synthesis of Nano-Structured Materials*, Springer-Verlag, Berlin, 1999.

[59] S.D. Wang, X. Dong, C.S. Lee, and S.T. Lee, *J. Phys. Chem. B*, 109, (2005) 9892.

[60] A.C. Mayer, R.Ruiz, R.L. Headrick, A.Kazimirovc and G.G. Malliaras, *Organ. Electr.* 5 (2004) 257.

[61] C.T. Rettner and D.J. Auerbach, J.C. Tully, A.W. Kleyn, *J. Phys. Chem.*, 100 (1996) 13021.

[62] M.C. McMaster, S. Schroeder, and R.J. Madix, *Surf. Sci.* 297 (1993) 253

[63] J.G. Amar and F. Family, *Phys. Rev. Lett.* 74 (1995) 2066.

[64] R. Ruiz, B. Nickel, N. Koch, L.C. Feldman, R.F. Haglund Jr., A. Kahn, F. Family and G. Scoles, *Phys. Rev. Lett.* 91 (2003) 136102.

[65] M. Tejima, K. Kita, K.. Kyuno and A. Toriumi, *Appl. Phys. Lett.* 85 (2004) 3746.

[66] B. Stadlober, U. Haas, H. Maresch and A. Haase, *Phys. Rev. B* 74 (2006) 165302.

[67] P.A. Burrough, *Principles of Geographical Systems for Land Resources Assessment, Clarendon*, Oxford (1986).

[68] E. Reichmanis, H. Katz, C. Kloc, A. Maliakal, *Bell Lab. Technol. J.* 10 (2005) 87.

[69] L. Torsi, A. Dodabalapur, *Anal. Chem.* 1 (2005) 381.

[70] B. Adhikari, S. Majumdar, *Prog. Polym. Sci.* 29 (2004) 699.

[71] G. Guillaud, J. Simon, J.P. Germain, *Coord. Chem. Rev.* 1443 (1998) 178.

[72] T. Toccoli, A. Pallaoro, N. Coppedè, S. Iannotta, F. De Angelis, L. Mariucci and G. Fortunato, *Appl. Phys. Lett.* 88 (2006) 132106.

[73] R. Ruiz, D. Choudhary, B. Nickel, T. Toccoli, K.C. Chang, A.C. Mayer, et al., *Chem. Mater.* 16 (2004) 4497.

[74] P. Milani, S. Iannotta, *Cluster beam synthesis of nanostructured materials*, Springer, (1999).

[75] S. Iannotta, T. Toccoli, A. Boschetti, F. Biasioli, M. Ferrari, *Appl. Phys. Lett.* 76 (2000) 1845.

[76] T. Toccoli, A. Boschetti, C. Corradi, L. Guerini, M. Mazzola, S. Iannotta, *Synth. Met.* 3 (2003) 137.

[77] L. Casalis, M.F. Danisman, B. Nickel, G. Bracco, T. Toccoli, S. Iannotta et al., *Phys. Rev. Lett.* 90 (2003) 206101.

[78] S. Iannotta, T. Toccoli, *J. Polym. Sci. B: Polym. Phys.* 41 (2003) 2501.

[79] Y. Wu, T. Toccoli, N. Koch, E. Iacob, A. Pallaoro, P. Rudolf et al., *Phys. Rev. Lett.* 98 (2007) 076601.

[80] D. Li, E.J. Borkent, R. Novtrup, H. Moon, H. Katz, Z. Bao, *Appl. Phys. Lett.* 86 (2005) 042105.

[81] R. Ruiz, A. Papadimitratos, A.C. Mayer, G.G. Malliaras, *Adv. Mater.* 17 (2005) 1795.

Chapter 6

In this final chapter, we will present an interesting novel architecture which combines metal oxide nanowires and organic materials. Going more in detail, an integration of zinc oxide nanowires onto carbon microfibers using electrochemical deposition and thermal oxidation approach has been developed and used as a versatile resistive sensor for both oxidizing and reducing gases.

This architecture is attractive because it allows mechanical flexibility, low cost and large-area fabrication. Being structured at both microscale and nanoscale, the ZnO nanowires-carbon microfiber (ZnO-μC) sensor possesses a greater surface area, giving rise to a strong and rapid response/ recovery time. Additionally, the ZnO-μC sensor is simple to manufacture, has a very low power consumption (less than 0.6 μW) and is prepared without any lithographic process.

The sensor exhibits excellent oxygen (down to 2 ppm) and hydrogen (down to 4 ppm of H_2) sensing characteristics, showing a fast response on gas exposure (less than 10s) and very good reversibility. Furthermore, the carbon microfiber is as flexible as a fabric is, thus, the ZnO-μC sensor could also be used in applications where flexibility is required. This architecture can also be expanded to other nanowire materials (CuO, Fe_2O_3, etc) widening the range of detected gases. We therefore believe that the integration of nanowires with carbon microfibers has the potential for being the next generation of simple and low cost sensor devices.

Hybrid sensors‡‡

During the last decades, solid-state gas sensors have played an important role in environmental monitoring and chemical process control [1].

‡‡ This Chapter is based on M. Tonezzer* and R.G. Lacerda, **"Zinc oxide nanowires on carbon microfiber as flexible gas sensor"**, in press, published online on ***Physica E: Low-dimensional Systems and Nanostructures***. doi:10.1016/j.physe.2010.11.029

Among the various solid-state sensors, semiconducting metal oxide sensors [2] have been widely studied due to their small dimensions, low cost, and low power consumption.

Across the many semiconductor oxide materials, zinc oxide is a very interesting one due to its chemical and thermal stability, its large exciton binding energy and bandgap as n-type semiconductor, and, especially, to its high response to toxic and combustible gases (see Chapter 2). To date, various types of ZnO-based gas sensors, such as thick films [3], thin films [4,5], nanoparticles [6] and nanowires [7,8], have been demonstrated. Compared to bulk ZnO and ZnO thin film gas sensors, quasi-1D ZnO nanowires provide a greater response to their increased surface-to-volume ratio [6]. Especially, ZnO nanowires have been grown by physical [9,10] (for instance, using Zn foil or powder), and chemical [11] methods proving to have promising sensing performance for both for hydrogen [12] and oxygen [13,14].

In this chapter, we will present a work in which zinc oxide nanowires were grown directly on highly conductive and flexible carbon fibers with a diameter of 10 microns. By integrating the microstructure of the fiber with the nanostructure of the nanowires, we provide a 3D architecture that achieves mechanical flexibility, low cost and large-area fabrication [15]. Being structured at both microscale and nanoscale, the ZnO-μC sensor possesses a greater surface area, giving rise to a strong and rapid response/ recovery time, being also able to detect both hydrogen and oxygen gases with excellent reversibility. The results presented in this letter show that the combination of nanowires with carbon microfibers may pave the way to simple and low cost sensor devices.

6.1 Multi-step deposition technique

Figure 6.1a shows a scanning electron micrograph (Quanta 200), operated at 15 kV, of the commercial carbon microfiber (EletroChem, Inc) having a diameter of about 10 microns.

Metallic zinc was deposited on the carbon microfibers by chemical electrodeposition, using 40 ml of 0.75 molar solution of $ZnCl_2$. The microfiber was placed 40 mm from a pure (99,99%) zinc electrode, and a 40 mA current was flowed through the solution for 20 minutes. The microfiber was dried and loaded in an alumina boat, then positioned at the center of a quartz tube that was inserted in a horizontal furnace. The growth process consisted in rising the temperature to 500 °C in 15 minutes, maintaining it for 2 hours and then cooling down slowly [16].

The thermal oxidation process creates a very light grey layer, made of hierarchic ZnO nanowires sprawling radially from each carbon microfiber, as can be seen from the SEM picture in Figure 6.1b. The nanowires diameters range between 50 and 150 nm, and have an average length of 2 μm, while the diameter of the “branches” is about 25 nm, as it can be seen in Figure 1d. A macroscopic view of the texture of the carbon microfiber with the ZnO nanowires is shown in Figure 6.1c.

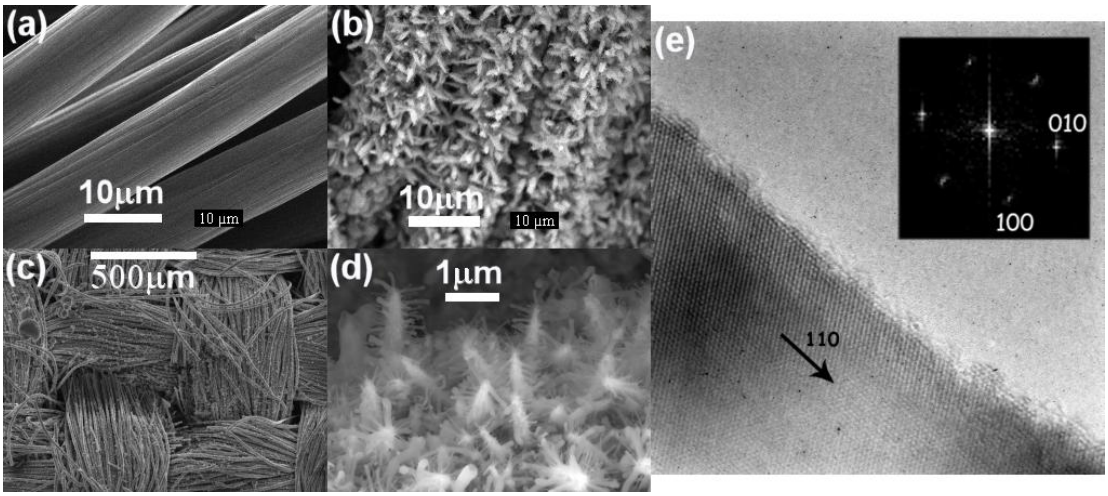

Figure 6.1: SEM (a-d) and TEM (e) images of samples. a) Carbon microfiber before zinc deposition; b) Carbon microfiber with ZnO nanowires sprawling radially; c) lower magnification image of the microfiber-nanowires sensor; d) zoom of the hierarchic nanowires; e) TEM image of a nanowire (inset shows SAED of the same wire) showing its crystallinity.

The good crystallinity of the wires was confirmed by transmission electron microscopy (TEM) (Tecnai G2 SuperTwin, operated at 200 kV) analysis, as shown in Figure 6.1e. The selected area electron diffraction (SAED) pattern shows that the nanowires are single crystalline wurtzite ZnO (a = b = 0.3249 nm, c = 0.5205 nm) with the [110] growth direction (inset of Figure 6.1e).

Gas sensing characteristics of the ZnO-μC system were measured using a home-built apparatus consisting of a test chamber (a furnace), a sensor holder, a Keithley 2410 multimeter, a Keithley 6517A electrometer, mass flow controllers and a data acquisition system (LabView, National Instruments), as shown in Figure 6.2. The test chamber is a quartz cylinder 300 mm long with a diameter of 20 mm, for a volume of about 94 cubic centimetres.

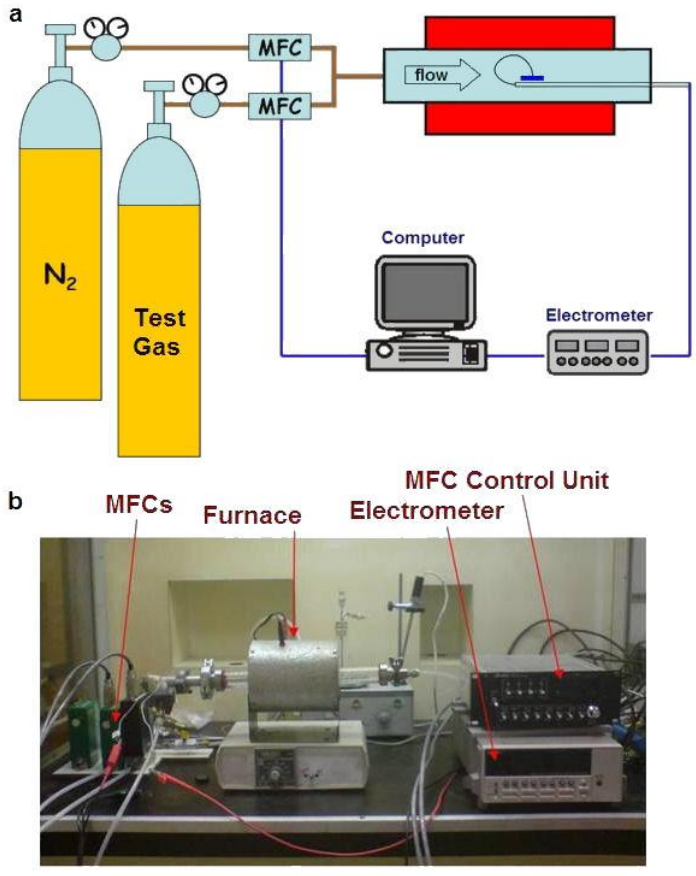

Figure 6.2: a) schematic diagram and b) photograph of the of the gas sensor test system.

For electrical measurements, silver paste contacts (2 mm diameter, 0.5 mm distance) were formed on the samples of area of 1cm x 1cm. Initially, the I-V characteristics were studied within ±10V range where it was found that the silver electrical contacts showed ohmic behaviour. In order to improve the repeatability, the devices were conditioned at 280 °C at 1V in N_2 for 5 hours prior the measurements to stabilize their microstructure and guarantee that their electrical properties would not change during gas tests.

The resistance of the sensors was in the 1 - 10 MΩ range under nitrogen atmosphere at 40 - 320 °C. During this “aging annealing” at high temperature in inert atmosphere, the surface of the zinc oxide loses many of the O^{2-} lattice and O^- desorbed ion species.

Consequently, oxygen vacancies are formed resulting in donor states that decrease the resistance of the oxide [17]. The sensors were operated at a constant 1V voltage between the contacts and were tested for O_2 and H_2 in the temperature range of 40 - 320 °C. The voltage value (1 V) and the mean current value in pure nitrogen (0.55 µA) give a mean power consumption of less than 0.6 µW. The total gas flow was maintained at 500 sccm in pure nitrogen (99,9999%) by using the mass flow controllers. The working temperature of the sensors was controlled by a feedback on the thermocouple inside the furnace. By monitoring the output current across the sensor, the resistances of the sensor in nitrogen or in test gases could be measured.

6.2 Hybrid carbon microfiber-zinc oxide nanowires gas sensor

6.2.1 Oxygen sensing properties

The response of the ZnO-µC sensor was first checked at different temperatures ranging from 40 to 320 °C to optimize the working temperature. As shown in Figure 6.3, the working temperature clearly influences the sensor response to 500 ppm of oxygen. Here we use the definition of sensor response as $S_R = R_G / R_N$ where R_N and R_G are, respectively, the resistance

of the nanowires exposed to air without and with the detecting gas). The sensor response has a peak at 280 °C, with a maximum value of 10.

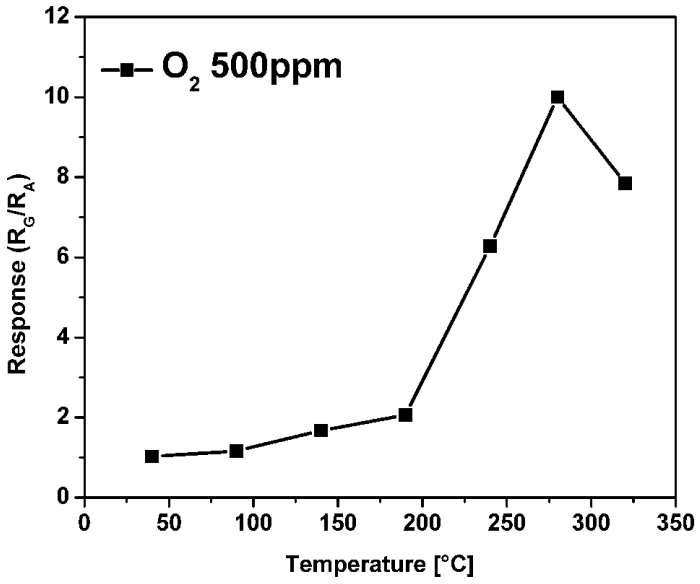

Figure 6.3: response of the ZnO-µC sensor to 500 ppm of O_2 as a function of the working temperature, showing a peak at 280°C.

A bell-shape behaviour as a function of working temperature has already been found [18] and has been explained by gas-diffusion theory [19]. The sensor starts working under 100 °C, but its response greatly improves over 200 °C, reaching its maximum at 280 °C. Therefore 280 °C has been chosen as the working temperature for oxygen gas.

Figure 6.4 shows the absolute value of current variation as a function of the gas concentration. It increases linearly from 0 to 200 ppm, then starts to saturate. The slope of the linear fit of the first part of Figure 6.4 is $3.1 \cdot 10^{-9}$A, while the standard deviation of the current signal in pure nitrogen is $2.1 \cdot 10^{-9}$A. Here we use the definition of limit of detection (LoD) as three times the standard deviation, obtaining an oxygen limit of detection (LoD) of 2 ppm.

Figure 6.5a shows the dynamic response of the ZnO-µC sensor under exposure to various levels of oxygen concentrations (100 - 600 ppm of O_2 in pure nitrogen) at 280°C.

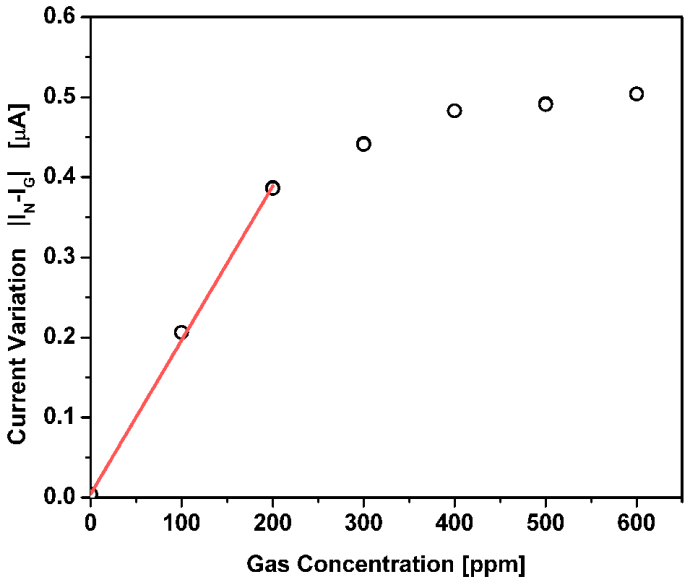

Figure 6.4: Current variation of the ZnO-μC sensor under exposure to different O_2 concentrations (100 - 600 ppm of O_2 in pure nitrogen) at 280°C; the linear fit serves to calculate the detectable oxygen limit of detection.

When the sensor was exposed to the oxygen/nitrogen as opposed to pure nitrogen, the resistance of the sensor rapidly increased reaching a relatively stable value. When the sensor was switched to pure nitrogen again, the resistance abruptly decreased and rapidly reached its former value. It is clear that the response increases with increasing concentration of O_2.

The relatively minor deviations between the increasing and the decreasing steps demonstrate that the sensors have good reversibility (Chapter 1). The sensor response ranges from 1.6 for 100 ppm to 13 for 600 ppm of O_2. The response is very stable and repeatable over a period of two months, as shown in Figure 6.5b.

The sensor response time is defined as the time taken for the sensor to reach 90% of the equilibrium value after the sensor has been exposed to oxygen, as can be seen in the inset of Figure 6.5 (also remember Chapter 1). The recovery time is defined as the time the sensor needs to recover 90% of the initial signal after the removal of oxygen [20]. The response time of the sensors was found to be less than 10s, and the recovery time about 12s.

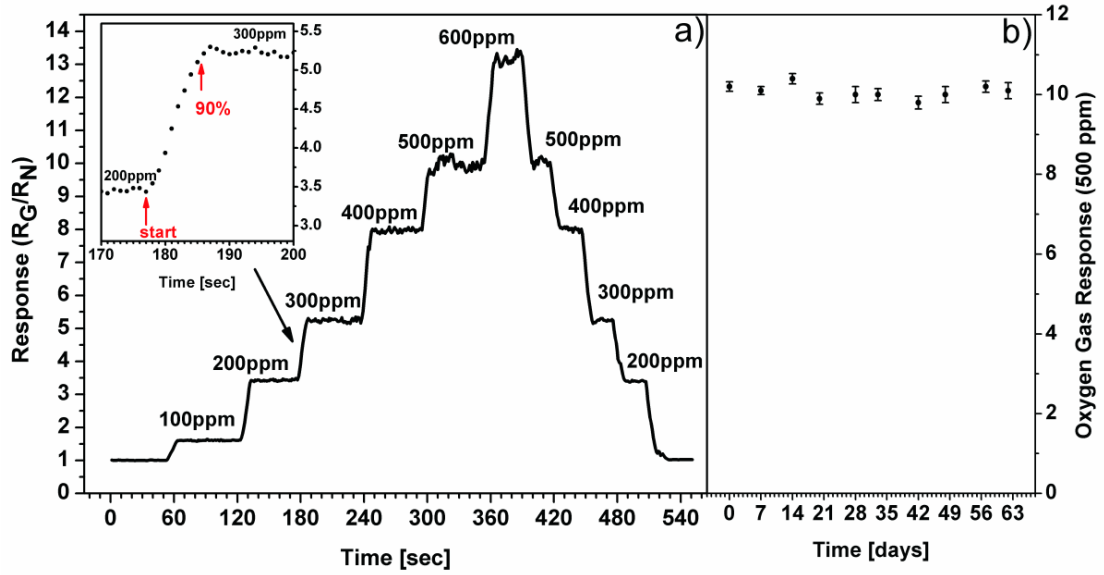

Figure 6.5: response transient of the ZnO-μC sensor under exposure to different O_2 concentrations (100 - 600 ppm of O_2 in pure nitrogen) at 280°C. The inset underlines the fast response time.

These times are much shorter if compared with those found by Chien-Yuan Lu and coworkers [21] (both response and recovery time larger than 1200 seconds) or by J.H. He and coworkers [22] (both response and recovery time larger than 300 seconds).

The fast response and recovery time can be related to two issues of the sensor: on one side the high surface-to-volume ratio due to the nano-on-micro structure, and on the other side the very thin “branches” nanowires, that improve its sensitivity.

The gas sensor response of the ZnO-μC devices to various concentrations of oxygen can be extracted from Figure 6.5 as a function of oxygen concentration, and will be discussed later

6.2.2 Hydrogen sensing properties

As a second step, the sensing properties of the ZnO-μC device have been tested with hydrogen. The definition of sensor response in the case of hydrogen is $S_R = R_N / R_G$, where R_G is the resistance in presence of hydrogen, and R_N the resistance in pure nitrogen. The temperature dependence of sensor response to 500ppm H_2 is shown in Figure 6.6. Also in this case the response exhibits a bell-shape, with its maximum at 300 °C. The gas sensor response reaches a maximum value of 11.0 at 280 °C for 500 ppm of hydrogen.

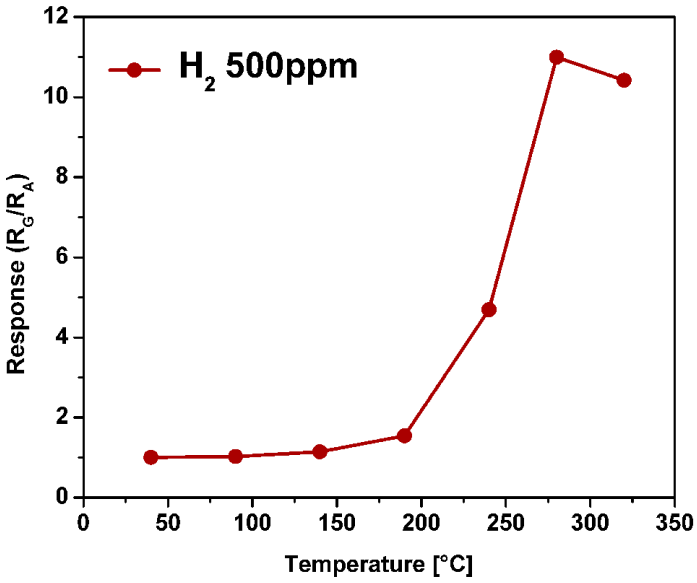

Figure 6.6: response of the ZnO-μC sensor to 500 ppm of H_2 as a function of the working temperature, showing a peak at 280°C.

Figure 6.7 shows the absolute value of current variation as a function of the hydrogen gas concentration. It increases linearly along the whole measured range. The slope of the linear fit in Figure 6.7 is $1.9 \cdot 10^{-8}$A, while the standard deviation of the current signal in pure nitrogen is $2.6 \cdot 10^{-8}$A. Here we use the definition of limit of detection (LoD) as three times the standard deviation, obtaining an hydrogen limit of detection of 4 ppm.

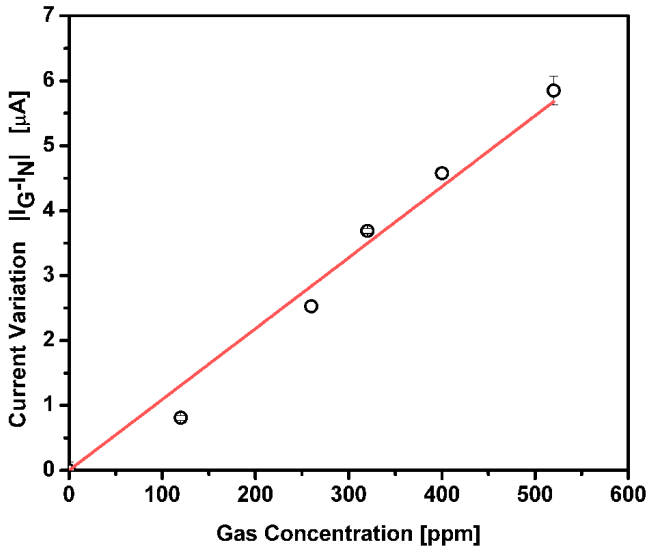

Figure 6.7: current variation of the ZnO-µC sensor under exposure to different H_2 concentrations (120 - 520 ppm of H_2 in pure nitrogen) at 280°C; the linear fit serves to calculate the hydrogen limit of detection.

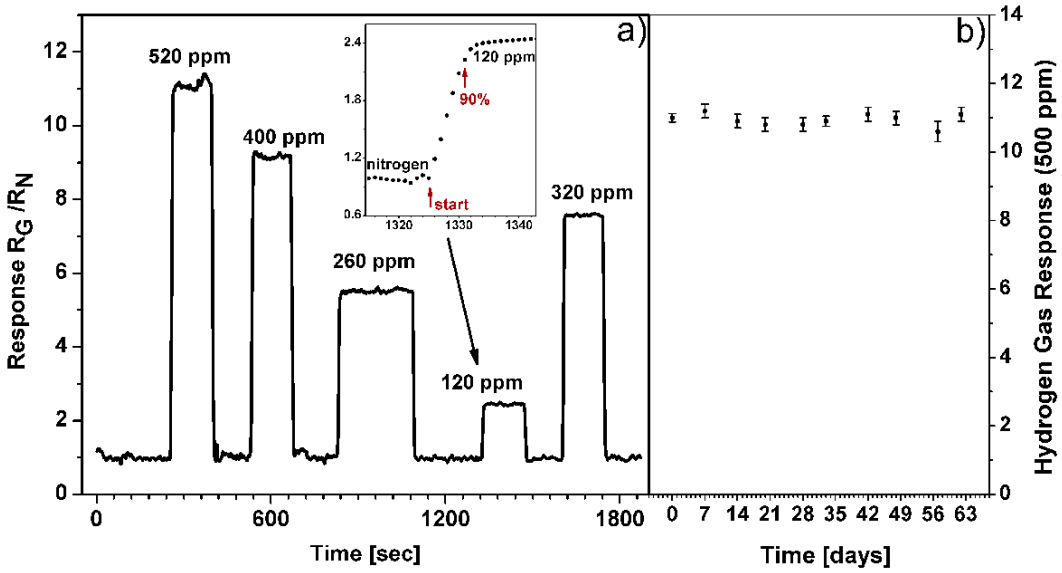

Figure 6.8: response transient of the ZnO-µC sensor under exposure to different H_2 concentrations (120 - 520 ppm of H_2 in pure nitrogen) at 280°C. The inset underlines the fast response time.

The gas dynamic response of the ZnO-μC sensor, measured at the optimal working temperature of 280 °C for various hydrogen concentrations, is shown in Figure 6.8a.

The sensor response ranges from 2.4 for 120 ppm to 11.1 for 520 ppm of hydrogen. The response is very stable and repeatable over a period of two months, as shown in Figure 6.8b. The sensors present a fast response time, defined as the time taken for the sensor to reach 90% of the equilibrium value after the sensor was exposed to hydrogen (as shown in the inset of Figure 6.8).

The recovery time is defined as the time the sensor needs to recover 90% of the initial signal after the removal of hydrogen gas. It was found that the response time of the sensors to H_2 was less than 8 seconds, whereas the recovery time was about 12 seconds.

These times are much shorter if compared with those found by J.X. Wang and coworkers [23] (response time of 200 seconds and recovery time of 800 seconds, respectively). Also in this case, the fast response and recovery time can be attributed to the huge surface-to-volume ratio and to the size of the hierarchic nanowires.

The ZnO-μC gas sensor shows very similar response values (10 to 500 ppm O_2 and 11.1 to 520 ppm H_2, respectively), response and recovery times (10 and 12 sec for O_2 gas, 8 and 12 seconds for H_2) for both oxygen and hydrogen gases.

6.3 Sensing mechanism

The electrical conductance of the ZnO nanowires changes in the presence of the oxidizing gas (oxygen in our case) due to two successive reactions occurring on the surface [24]. In the first reaction, atmospheric oxygen molecules, which are physisorbed on the surface sites (Eq. 6.1), are ionized while moving from site to site, by capturing electrons from the conduction band, thus becoming ionosorbed on the surface (Eq. 6.2a, b, c).

Due to this phenomenon the oxygen is chemisorbed in the form of O_2^-, O^- or O^{2-} depending on the operating temperature [25]:

$$O_{2\,(gas)} \leftrightarrow O_{2\,(adsorbed)} \qquad (6.1)$$

$$O_{2\,(adsorbed)}^- \leftrightarrow 2\,O_{(adsorbed)}^- \qquad T < 100°C \qquad (6.2a)$$

$$O_{2\,(adsorbed)} + e^- \leftrightarrow O_{2\,(adsorbed)}^- \qquad 100°C < T < 300°C \qquad (6.2b)$$

$$O_{(adsorbed)}^- + e^- \leftrightarrow O_{(adsorbed)}^{2-} \qquad T > 300°C \qquad (6.2c)$$

As shown by the above equations, the electrons are consumed in the reactions, thus explaining the increase of the ZnO resistance after the O_2 exposure. On the contrary, in the case of a reducing gas (hydrogen in our case), it reacts with the oxygen at the zinc oxide surface, thereby releasing an electron to the conduction band and increasing the conductance of the semiconductor.

$$H_2 + O^- \leftrightarrow H_2O + e^- \qquad (6.3)$$

In the case of ZnO nanostructures, electrons are also extracted from the interstitial zinc atoms which act as electron donors [26]. The interstitial zinc atoms in such cases are ionized via the following reversible reaction

$$Zn_i^+ \leftrightarrow Zn_i^{2+} + e^- \qquad (6.4)$$

Based on the ideas described above we will now discuss the mechanism that governs the ZnO-μC sensors. For n-type ZnO single-crystals, the intrinsic carrier concentration is primarily determined by deviations from stoichiometry, usually in the form of interstitial zinc and oxygen vacancies, which are predominantly atomic defects acting as electron donors [27]. The conduction electrons resulting from the point defects play a major role in gas sensing of various materials.

Thus, the electrical conductivity of nanocrystalline ZnO strongly depends on the surface states produced by molecular adsorption that results in space-charge layer changes and band modulation [28]. In the space charge

model, the sensor response S (defined as the ratio of R_G to R_N for oxygen and oxidizing gases, where R_N is the electrical resistance in nitrogen and R_G is the resistance after gas exposure) can usually be represented as

$$S = \text{const} \cdot C^N \qquad (6.5)$$

where C is the target gas concentration and N is typically 1 or 0.5, depending on the charge of the surface species and the space-charge layer thickness (a Debye length, also called depletion layer in Chapter 3) L_D of the sensing material. If the diameter of the material is close or smaller than $2L_D$, N is about 1.

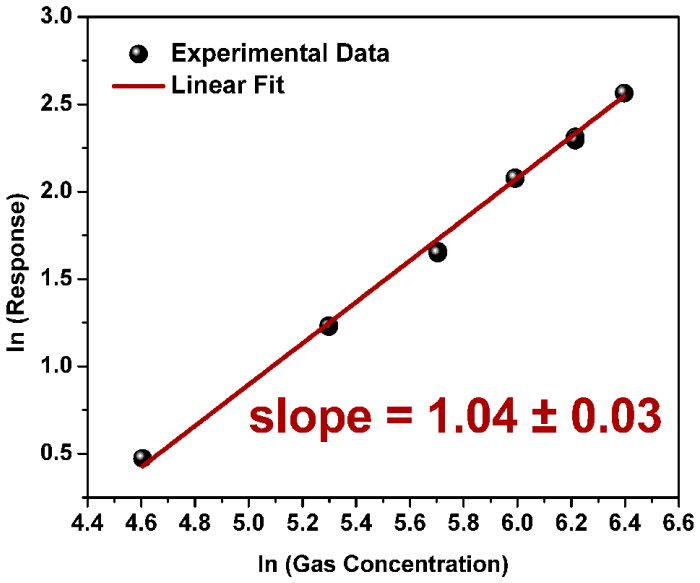

Figure 6.9: plot of logarithm of response S versus logarithm of oxygen concentration C: ln(S) versus ln(C). The fit close to 1 proves the space charge model.

In literature, the thickness L_D of the ZnO nanostructured material around 300°C is calculated to be approximately 10 nm [29,30]. The diameter for the small nanowires, at the surface of our sensors, was about 20-30 nm and

therefore N should be close to 1. Figure 6.9 shows a plot of ln(S) versus ln(C), where the linear relationship is evident and N is estimated to be 1.04 ± 0.04.

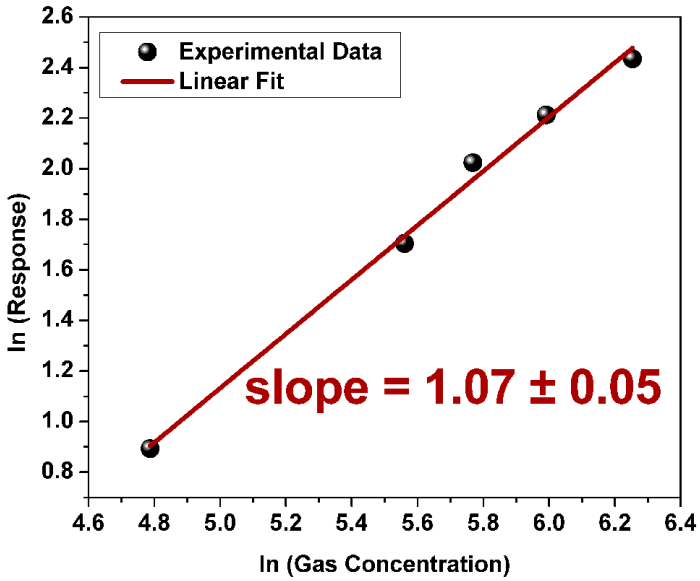

Figure 6.10: plot of logarithm of response S versus logarithm of hydrogen concentration C: ln(S) versus ln(C). The fit close to 1 proves the space charge model.

Similarly, Figure 6.10 shows the plot of ln(S) versus ln(C) in the case of H_2 gas, and also here the linear relationship is evident again and N is calculated to be 1.07 ± 0.05. According to this analysis, we can propose that the sensing mechanism for both hydrogen and oxygen gases follows the space charge model.

6.4 Conclusions

In summary, we have synthesized a hierarchic micro-on-nano structure based on ZnO nanowires grown on a carbon microfiber and acting as a promising O_2 and H_2 sensor. The micro-on-nano structure leads to a

dramatically high surface and flexibility of the device. Gas sensing performance is very good at 280-300 °C, with a sensor response of 11 for 500 ppm of O_2 and 10.1 for 520 ppm of H_2.

Response and recovery time are fast (<9 and <8 seconds for O_2 and H_2, respectively) and the device shows good reversibility. The sensor selectivity is going to be investigated in a future work. Furthermore, the absence of any lithographic process makes the sensors very easy and cheap to fabricate, while the low power consumption (less than 0.6 μW) makes them low-cost to operate.

Additionally, the methodology developed here can also be expanded to other nanowires materials providing a way to develop other kinds of simple and low-cost gas sensors.

[1] P.T. Mosley and B.C. Tofield, *Solid State Gas Sensor*, Hilger, Bristol, 1987.

[2] S.M. Sze, *Semiconductor Sensors*, Wiley, New York, 1994.

[3] M.S. Wagh, G.H. Jain, D.R. Patil, S.A. Patil and L.A. Patil, *Sens. Actuators B* 115 (2006) 128-133.

[4] G. Sberveglieri, *Sens. Actuators B* 23 (1995) 103-109.

[5] A. Rothschild, F. Edelman, Y. Komem and F. Cosandey, *Sens. Actuators B* 67 (2000) 282-289.

[6] J. Xu, Y. Zhang, Y. Chen, Q. Xiang, Q. Pan and L. Shi, *Mater. Sci. & Engin. B* 150 (2008) 55-60.

[7] N. Zhang, K. Yu, Q. Li, Z.Q. Zhu and Q. Wan, *J. Appl. Phys.* 103 (2008) 104305.

[8] J.Y. Son, S.J. Lim, J.H. Cho, W.K. Seong and H. Kim, *Appl. Phys. Lett.* 93 (2008) 053109.

[9] J. Zhang, Y. Yang, B. Xu, F. Jiang and J. Li, *J. Cryst. Growth* 280 (2005) 509-515.

[10] T. Ghoshal, S. Biswas, S. Kar, A. Dev, S. Chakrabarti and S. Chaudhuri, Nanotechnology 19 (2008) 065606.

[11] C. Lu, L. Qi, J. Yang, L. Tang and D. Zhang, *J. Mat. Chem. Commun.* 33 (2006) 3551-3553.

[12] H.T. Wang, B.S. Kang, F. Ren, L.C. Tien, P.W. Sadik, D.P. Norton, S.J. Pearton and J. Lin, *Appl. Phys. Lett.* 86 (2005) 243503.

[13] Q.H. Li, Y.X. Liang, Q. Wan and T.H. Wang, *Phys. Lett.* 85 (2004) 6389-6391.

[14] Z. Fan, D. Wang, P. Chang, W. Tseng, J.G. Lu, *Appl. Phys. Lett.* 85 (2004) 5923-5925.

[15] H.E. Unalan et al., *Appl. Phys. Lett.* 93 (2008) 133116.

[16] A.M.B. Goncalves, L.C. Campos, A.S. Ferlauto and R.G. Lacerda, *J. Appl. Phys.* 106 (2009) 034303.

[17] A. Kolmakov, Y. Zhang, G. Cheng and M. Moskovits, *Adv. Mater.* 15, 12 (2003) 997-1000.

[18] L. Bie, X. Yan, J. Yin, Y. Duan, Z. Yuan, *Sens. Actuators B* 126 (2007) 604-608.

[19] G. Sakai, N. Matsunaga, K. Shimanoe, N. Yamazoe, *Sens. Actuators B* 80 (2001) 125-131.

[20] V.R. Shinde, T.P. Gujar, C.D. Lokhande, R.S. Mane, Sung-Hwan Han, *Mater. Sci. & Engin. B* 137 (2007) 119-125.

[21] Chien-Yuan Lue t al., *IEEE Sensors Journal*, 9 (2009) 485.

[22] J.H.He, C.H. Ho and C.Y. Chen, *Nanotech.*, 20 (2009) 065503.

[23] J.X. Wang et al, *Nanotech.* 17 (2006) 4995-4998.

[24] H. Windischmann and P. Mark, *J. Electrochem. Soc.* 126 (1979) 627-633.

[25] K. Arshak and I. Gaidan, *Mater. Sci. Eng. B* 118 (2005) 44-49.

[26] M. Takata, D. Tsubone and H. Yanagida, *J. Am. Ceram. Soc.* 59 (1976) 4-8.

[27] Z.M. Jarzebski, *Oxide Semiconductors*, vol. 4, Pergaman Press, 1973.

[28] H. Windischmann and P. Mark, *J. Electrochem. Soc.* 126 (1979) 627-633.

[29] Y.J. Chen, C.L. Zhu and G. Xiao, *Nanotechnology* 17 (2006) 4537-4541.

[30] N. Yamazoe, G. Sakai and K. Shimanoe, *Catalysis Surv. Asia* 7 (2003) 63-75.

Conclusions

This doctorate thesis had the goal to investigate two of the main materials families used in gas sensor applications: metal oxides (and principally metal oxide nanowires) on one side, and small conjugated molecules as test organic material on the other side. For this reason two paths have been followed simultaneously along this work (even if the two materials are in different development steps) to converge at the end, with the exploitation of both of them.

We started with a chapter on the basics of sensors, and giving simple definitions of the main quantities which characterize them and can be used to compare their performance, like response intensity, reversibility, response and recovery times (50% and 90%) specificity, selectivity and drifts. Not all of these parameters are usually cited in literature, but it is important to understand the meaning of each term, because comparison between two devices is fundamental in gas sensing field.

We have then shown the basics of metal oxide nanostructures, and specifically nanowires, explaining the sensing mechanism up to now recognized as responsible of their good response, and giving a picture of the sensing state of the art. After this preliminary part, the inorganic part of this thesis started elucidating the investigations and characterizations (SEM, HR-TEM, GI-XRD) which lead us to the discovery of a novel growth mechanism of zinc oxide nanowires.

This catalyst-assisted growth model, operating at low temperature, much lower than the lowest eutectic point of the Au-Zn binary system, involves the presence of a Au-Zn solid particle in a Vapour-Solid-Solid mechanism which is driven by the etero-epitaxy between the two good matching planes: ZnO(10-10) of the nanowire and γ-AuZn(222) of the catalyst solid nanoparticle.

Concerning the use of monocrystalline single nanowires as sensing devices, tin oxide nanowires grown by thermal CVD have been used as passive (resistive) gas sensors bridging two Ti/Pt electrodes. Using NO_2 as testing gas, the response of 5 different nanowires with different diameters

(ranging from 41 to 117 nm) has been characterized as a function of working temperature and gas concentration. While the fast response and recovery time (3 seconds each at 400°C) don't seem to depend on the nanowire diameter, the response intensity increases when the nanowire diameter decreases.

Developing a simple model to simulate the depletion layer modulation, the experimental results have been fitted for different values of gas concentration, finding for the depletion layer depth an average value of 14 nanometres, which is in good agreement with literature.

After a short general introduction on small conjugated molecules, their growth and the SuMBD technique, the organic part was divided in 3 sections, concerning the growth of one different molecular material each: α-quaterthiophene, α-sexithiophene and pentacene.

The first section simply investigated the thin film growth of 4T as a function of its E_K, correlating the morphological order to the performance of FETs fabricated with such thin films, and finding a linear relation between the grain size and the hole mobility.

The second part showed a study on the growth of 6T as a function of the main deposition parameters: substrate temperature, substrate wettability and kinetic energy of the impinging molecules. Such a comprehensive investigation lead to a better understanding of the growth of the first monolayer, which is of crucial importance in organic devices working.

The higher E_K provided by the supersonic beam doesn't only increase the islands size, but also decreases their fractal dimension, resulting in a much lower grain boundary density. We also demonstrated how this is reflected in a much better performance of the field effect transistors fabricated on such more ordered films grown with high energetic impinging molecules.

In the third of the chapter, pentacene sub-monolayer growth has been investigated, focussing on the different contribution of parallel and perpendicular momentum components, $E_{//}$ and $E_{\perp}$. The first one is more related to a molecule-surface interaction (when $E_{//}$ increases, the sticking coefficient decreases and more compact islands grow), while the second one

is more related to molecule-molecule interaction (a higher value of $E_{\perp}$ decreases the critical nucleus size and increases the island density).

The chapter ends with a preliminary study on the sensing capability of pentacene ordered thin films. Here we showed that a better arrangement of molecular monolayers affects also the device stability in air: a thin film grown with a high energetic supersonic beam is almost unaffected by the presence of air (laboratory normal air), on the contrary of the films grown with less energetic beams.

The pentacene thin film sensor was tested with ethanol vapours, both statically and dynamically, and the OFET configuration was found to increase greatly the sensor response (120 times higher from V_G = -20V to V_G = -60V), showing that ordered molecular materials are worth further investigation in this field.

This doctoral thesis ends with the combination of inorganic and organic worlds in a hybrid nano-on-micro architecture which exploits carbon microfiber advantages during the fabrication process and giving the ZnO nanowires sensor a flexibility it couldn't have by standing alone.

The zinc oxide nanowires, sprouting radially from the carbon microfibers tissue, showed a maximum response at 280°C both for O_2 and H_2, and short response and recovery times (10 and 12 second for oxygen, 8 and 12 seconds for hydrogen, respectively) and low limits of detection (2 and 4 ppm for O_2 and H_2, respectively).

Such a hybrid architecture is only one among the wide range of combination which could exploit a synergy of useful properties of metal oxides and molecular materials (high response and stability of metal oxides and selectivity of tailored small molecules).

My personal opinion is that great perspectives are hiding behind such synergy. Furthermore, using a powerful tool such as SuMBD technique, we will be able to control the metal oxide-molecular film interface, which will greatly affect the performance of the new generation of sensors.